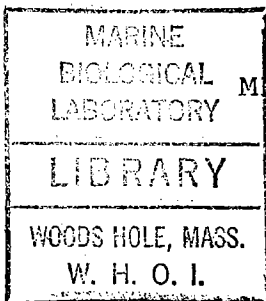


2214 GC
7.1
R44
1976

KINEMATICS AND ENERGETICS

OF THE MESOSCALE

MID-OCEAN CIRCULATION: MODE



JAMES GREGORY RICHMAN

B. S., Harvey Mudd College

(1971)

SUBMITTED IN PARTIAL FULFILLMENT OF THE
REQUIREMENTS FOR THE DEGREE OF
DOCTOR OF PHILOSOPHY

at the

MASSACHUSETTS INSTITUTE OF TECHNOLOGY

and the

WOODS HOLE OCEANOGRAPHIC INSTITUTION

September, 1976

Signature of Author..... *James G. Richman*
Joint Program in Oceanography, Massachusetts
Institute of Technology-Woods Hole Oceanographic
Institution and Department of Earth and Plane-
tary Sciences, Massachusetts Institute of Tech-
nology, September, 1976

Certified by..... *Carl Wunsch*
Thesis Supervisor

Accepted by..... *J.M. Arnold*
Chairman, Joint Oceanography Committee in the
Earth Sciences, Massachusetts Institute of
Technology-Woods Hole Oceanographic Institution

KINEMATICS AND ENERGETICS OF THE
MESOSCALE MID-OCEAN CIRCULATION: MODE

by

James Gregory Richman

Submitted to the Massachusetts Institute of Technology-Woods Hole Oceanographic Institution Joint Program in Oceanography on September 3, 1976, in partial fulfillment of the requirements for the degree of Doctor of Philosophy

ABSTRACT

The temporal and spatial variability of low frequency moored temperature and velocity observations, obtained as part of the Mid-Ocean Dynamics Experiment (MODE), are analyzed to study the kinematics and energetics of meso-scale eddies in the ocean.

The temporal variability of the low frequency motions is characterized by three regimes: very low frequencies with periods greater than 200 days, an eddy energy containing band of 80 to 120 day periods, and high frequencies with periods less than 30 days. At very low frequencies, the zonal kinetic energy exceeds the meridional at all depths. In the thermocline, the very low frequency zonal flow dominates the total kinetic energy. The greatest contribution to the kinetic and potential energy in the MODE region, except for the thermocline zonal flow, is from an eddy energy containing band of 80 to 120 day periods. Eddy scale kinetic energy spatial variations are confined to this band. At high frequencies, the kinetic and potential energy scale with frequency as $\omega^{-2.5}$ and with depth in the WKB sense. Energy at high frequencies is partitioned evenly between zonal kinetic, meridional kinetic and potential energy and is homogeneous over 100 km.

Using the technique of empirical orthogonal expansion, the vertical structure of the energetically dominant eddies is described by a few modes. The displacement is dominated by a mode with a thermocline maximum and in phase displacements with depth, while the kinetic energy is dominated by an equivalent barotropic mode. A smaller portion of the

kinetic and potential energy is associated with out of phase thermocline and deep water currents and displacements.

The dynamics of the mesoscale eddies are very nonlinear. Using the vertical veering of the current at MODE Center, the estimated horizontal advection of heat contributes significantly to the low frequency thermal balance. The observed very low frequency anisotropic flow is consistent with the nonlinear eddy spindown models, dominated by cascades of vorticity and energy. At high frequencies, the spectral similarity is consistent with advected geostrophic turbulence.

Thesis supervisor: Carl I. Wunsch
Title: Professor of Oceanography

ACKNOWLEDGEMENTS

A number of people contributed greatly to both my education and research efforts and I would be remiss in not recognizing some of them. Carl Wunsch, as my thesis advisor, provided much patient and persistent advice and criticism. His guidance helped me to successfully complete this thesis and taught me the importance of clear and concise presentation of results. Bill Schmitz introduced me to oceanography and the delights of low frequency motions and continued to help me throughout my student days. Nelson Hogg generously gave his time and helpful advice and acted as a sounding board for my ideas. Peter Rhines taught me about waves and the intricacies of non-linear flows. I want to thank Barbara Grant and Charmaine King for assisting me in my battles with the computer and, in the end, doing much of my work. For the last three years I received generous support from the Fannie and John Hertz Foundation, which definitely made life as a student easier and more enjoyable. The National Science Foundation supported my work through grants GX29034 and IDO-75-03998 and a graduate fellowship. Lastly, I want to thank all my friends, especially mj and ur, for their moral support and friendship; without them I never would have survived.

TABLE OF CONTENTS	PAGE
Abstract	1
Acknowledgements	3
I. Introduction	7
II. Mesoscale Spatial Variability	19
1. Objective mapping of temperature	19
2. Statistical assumptions	39
2.1 Probability distribution of temperature	39
3. Horizontal variation of temperature	48
3.1 Spatially averaged temperature spectra	48
3.2 Isotropic correlation functions	53
3.3 Horizontal coherence	56
3.4 Wavenumber spectra	58
4. Vertical variation of temperature	62
4.1 Vertical coherence	62
4.2 Empirical vertical structure	65
4.3 Velocity vertical structure	70
5. Kinetic and potential energy in the MODE region	73
5.1 Mean flow	73
5.2 Kinetic energy	76
5.3 Potential energy	80
5.4 Reynolds stresses and heat flux	81
6. Summary and discussion	84
III. Temporal Variability	86
1. Spectral estimation	86

	PAGE
2. Very low frequency fluctuations	88
3. Small scale fluctuations	107
4. Summary and discussion	109
IV. Possible Dynamical Mechanisms	110
1. Quasigeostrophic waves	110
1.1 Computation of the normal modes in the MODE region	111
1.2 Weak nonlinear interactions	119
2. Numerical models of the large scale development of the mesoscale flow	133
3. Summary and discussion	137
V. Relationship of the Observations to Possible Dynamical Mechanisms	139
1. Wave models	139
1.1 MODE-I	140
1.2 Site mooring observations	149
1.3 Summary and discussion	157
2. Comparison to numerical models	158
3. Horizontal advection of heat	160
4. Summary and discussion	169
VI. Conclusions	171
Appendix A Representativeness of Moored Temperature Observations	176
A.1 Mooring motion	176
A.2 Density and dynamic height estimation	185

	PAGE
Appendix B Maximum Entropy Spectral Estimation . .	192
Appendix C Site Mooring Data Summary	194
Bibliography	198
Biographical Note	205

I. Introduction

In recent years the nature of low frequency mesoscale oceanic fluctuations, that is, motions with time scales much greater than a day and horizontal length scales of tens to hundreds of kilometers, and their role in the general circulation of the ocean have come under increasing investigation. Prior to 1960, the circulation of the ocean was depicted as a slow interior flow in Sverdrup balance (Sverdrup, 1947) with intense western boundary currents (Stommel, 1948 and Charney, 1956) and possibly, linear waves driven by the action of the wind (Veronis and Stommel, 1956). The discovery of energetic, highly variable in space and time, currents south of Bermuda by the Aries expedition (Crease, 1962 and Swallow, 1971) raised doubts about the simple linear wind-driven circulation models.

The existence of energetic mesoscale fluctuations posed a number of questions:

- 1) Can the mesoscale motions be characterized statistically?
 - 2) What are the dynamics of the low frequency motions?
 - 3) What are the sources and sinks of energy?
- and
- 4) How important are the mesoscale motions in the energetics of the ocean?

The mesoscale motions (or "eddies") are potentially quite important in determining the mean circulation of the ocean. By analogy to the large scale motions in the atmosphere, where the transport of angular momentum by the eddies is thought to

drive the trade winds and middle latitude surface westerlies (Lorenz, 1969), the circulation of the ocean, predicted neglecting eddy transport processes, will not be the same as the average observed circulation. The mesoscale motions are potentially important in the redistribution of momentum and heat in the ocean. Thus, it is of interest to describe the kinematics and energetics of the mesoscale mid-ocean eddies.

Historical Background

The first direct observations of energetic mesoscale currents were obtained by the Aries expedition south of Bermuda (Crease, 1962 and Swallow, 1971). Using neutrally buoyant floats at nominal depths of 2 and 4 km, Swallow and Crease expected to measure a slow mean drift of less than 1 cm/sec, but instead relatively high speeds of 5 to 10 cm/sec were observed over the 4 to 10 day float trajectories. Crease estimated the time scale of the motions from the large scale changes in the directions of the float trajectories as 10 to 15 days (50 to 100 day period). Phillips (1966) estimated the length scale as 50 to 70 km (300 to 400 km wavelength). Swallow (1971) noted that long time scale motions in the ocean should be nearly geostrophic and found that the observed vertical shear of the floats was, on the average, geostrophic within rather large error bounds. However, some individual float pairs apparently did deviate from geostrophy.

Energetic mesoscale motions are present throughout the world's oceans. Wunsch (1972), using data in the main thermo-

cline at Bermuda, and Gill (1974a), using bathythermograph data from ocean weather ships, observed that the temperature variance is dominated by periods of 40 to 200 days. Bernstein and White (1974) observed westward propagating eddies in the central North Pacific with length and time scales consistent with baroclinic Rossby waves. During a large scale experiment, POLYGON, in the tropical Atlantic, Koshlyakov and Grachev (1973) observed an anticyclonic eddy with approximately 116 day period and 360 km wavelength moving westward through a moored current meter array.

The mesoscale eddies appear to be basically geostrophic, as observed by Swallow (1971) from the Aries observations and by Koshlyakov and Grachev (1973) in the POLYGON observations, with the governing dynamics of the low frequency motions occurring as deviations from a basic geostrophic state. Initially, linear wave models were used to describe mesoscale eddy observations. Using a two layer model of barotropic and baroclinic Rossby waves for the Aries observations, Phillips (1966) noted that most of the energy appears to be in the barotropic mode. Similarly, McWilliams and Robinson (1974) fit Rossby waves to the POLYGON data, suggesting that linear dynamics might be locally valid, because two linear waves described the gross features of the observations. However, in general, the magnitude of the neglected nonlinear terms is large and inconsistent with linear dynamics.

Knowledge of the energy sources for the mesoscale motions is important to the understanding of their complete dynamics. Recognizing the large amount of potential energy in the mean circulation of the ocean, a number of investigators have considered baroclinic instability as a possible source for the mesoscale eddies in direct analogy to meteorological ideas. Robinson and McWilliams (1974) observed, in a two layer model that, for realistic mid-ocean shears in the western return flow, growth rates of the order of a few months could be obtained. Holland and Lin (1975) showed numerically the formation of eddies by baroclinic instability in the western return flow. Orlandi and Cox (1973) found that intense currents such as the Gulf Stream are baroclinically unstable. However, baroclinic instability is not the only possible source of low frequency fluctuations. For example, the radiation field from the Gulf Stream meanders may be another source. Holland and Lin (1975) and Haidvogel (1976) observed regions of barotropic instability, converting the mean kinetic energy into eddy kinetic energy, in their numerical models.

In addition to knowledge of the source mechanisms for the low frequency kinetic energy, we need to know how the eddy energy is redistributed in both physical and wavenumber space throughout the ocean from the source regions. Rhines (1975, 1976), Owens (1975) and Bretherton and Haidvogel (1976) in numerical experiments consider the evolution of an existing eddy field via turbulent cascades of energy and vorticity. The propagation of nonlinear Rossby waves stops the vorticity

cascade and provides a controlling mechanism for the evolution of eddies. From the eddy spindown experiments, the dual nature of turbulence and waves in the oceanic parameter range is observed. Wavelike characteristics such as propagation are observed even in highly nonlinear flows.

While a number of mechanisms for the generation and evolution of mesoscale eddies have been suggested, there is little overall understanding of the kinematics, energetics or dynamics of low frequency motions in the ocean. As a start towards understanding mesoscale oceanic eddies, we want to describe kinematically the results of a large scale experiment in the western North Atlantic Ocean, the Mid-Ocean Dynamics Experiment, and then use these results to infer the possible eddy energetics and dynamics.

Mid-Ocean Dynamics Experiment (MODE)

As part of the effort to investigate the kinematics, energetics and dynamics of oceanic mesoscale eddies, an international cooperative experiment, the Mid-Ocean Dynamics Experiment (MODE), was performed southwest of Bermuda over the Hatteras Abyssal Plain. MODE spanned four years from 1971 to 1975 with three phases: MODE-0 with three preliminary mooring arrays in 1971 and 1972, MODE-I with an intensive four month, sixteen mooring array and SOFAR float and STD surveys in 1973, and post-MODE with two site moorings maintained in the region. During MODE-0, described by Gould, et al. (1974), the velocity and temperature records were

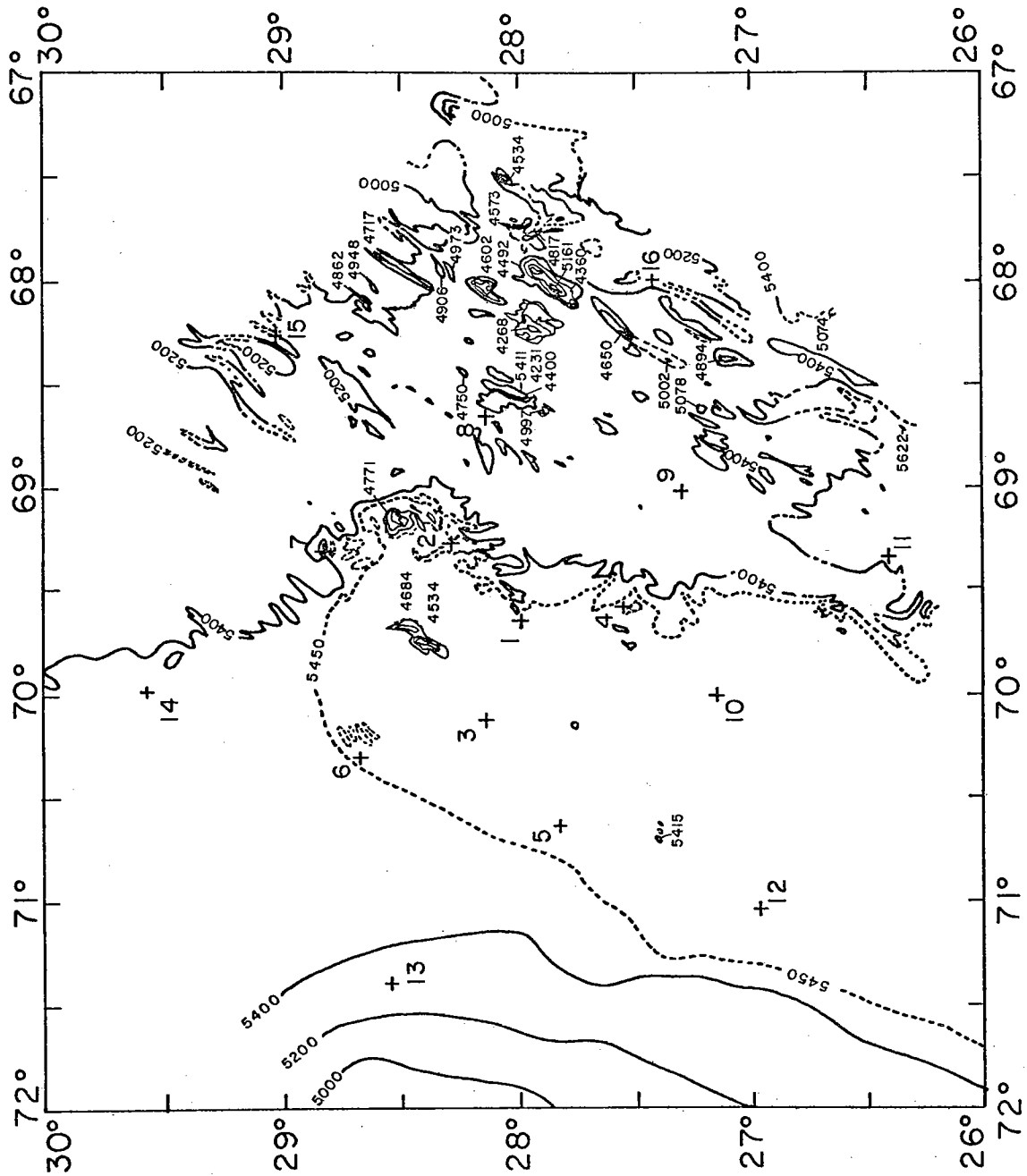


Figure I.1: MODE bathymetry and mooring locations
(after Pat Bush)

dominated by 50 to 100 day fluctuations with apparent horizontal scale of 60 km, consistent with previous observations of mesoscale eddies (for example, the Aries observations of Crease and Swallow). (Here the term scale is defined as the dominant period or wavelength divided by 2π .)

The data from MODE provide an opportunity to begin to characterize statistically the kinematics and energetics of mesoscale eddies in at least a small portion of the ocean. In this thesis, we shall concentrate on the results from the moored velocity and temperature observations. Results from the SOFAR floats, described by Freeland, et al. (1975), and from the STD casts, described by Scarlet, et al. (1976), will be considered as supporting evidence but not discussed in detail. During MODE-I, sixteen moorings were deployed for up to four months. The mooring locations and bathymetry of the experimental region are shown in Figure I.1. The array covered a circle of nominal radius of 200 km centered on mooring 1 at 28° N and $69^{\circ}40'$ W. Approximately half the area was over the smooth Hatteras Abyssal Plain and the remainder over the abyssal hills to the east. This intensive experiment was designed to give a detailed synoptic picture of a mesoscale eddy. To provide information about the longer term behavior of the mesoscale eddy field, two site moorings, located at mooring 1 and 8, were maintained throughout MODE with an intermittent data return. The two site mooring locations, moorings 1 and 8, will be designated MODE Center and MODE East respectively.

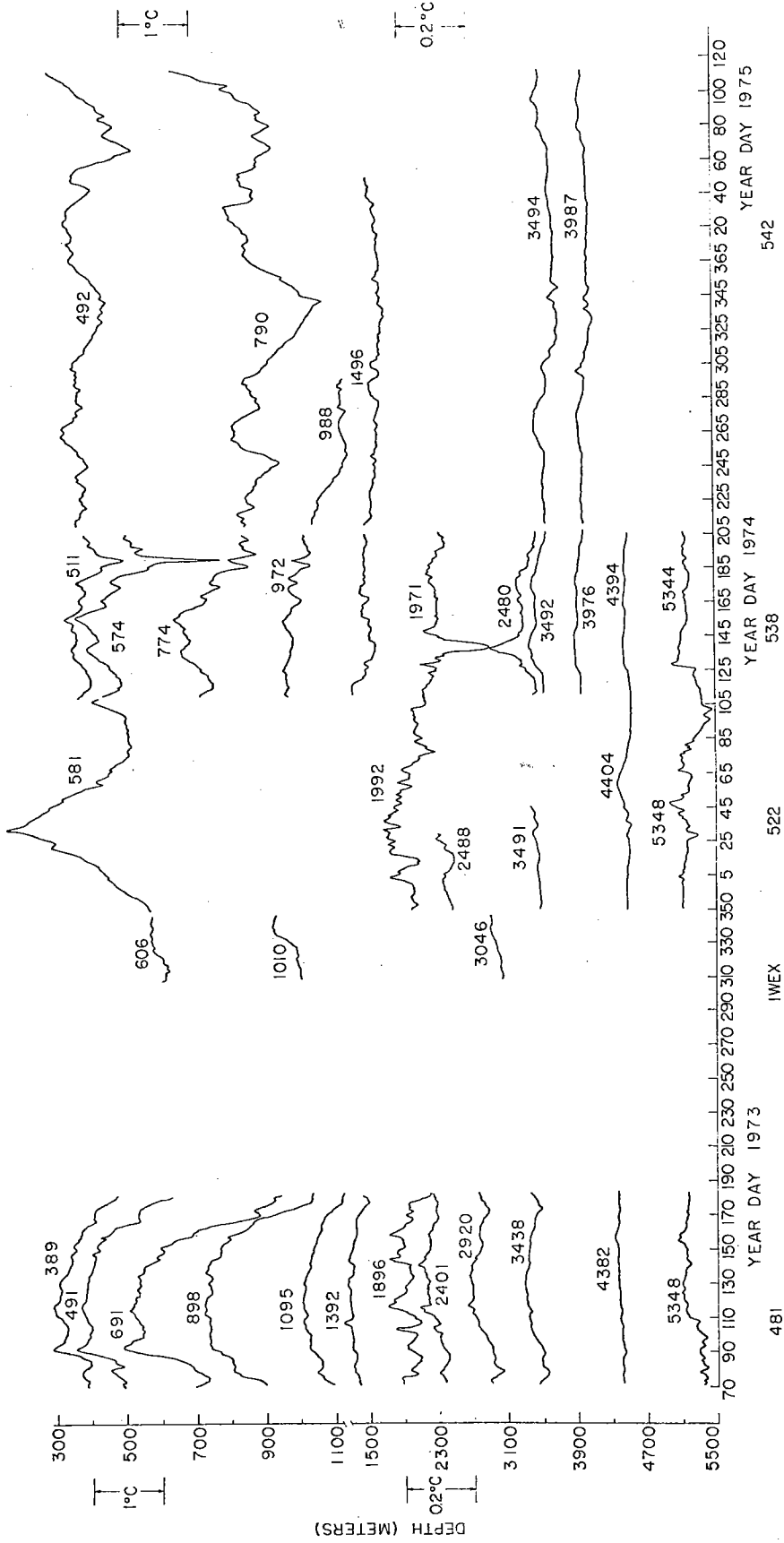


Figure I.2a: Temperature observations at MODE Center

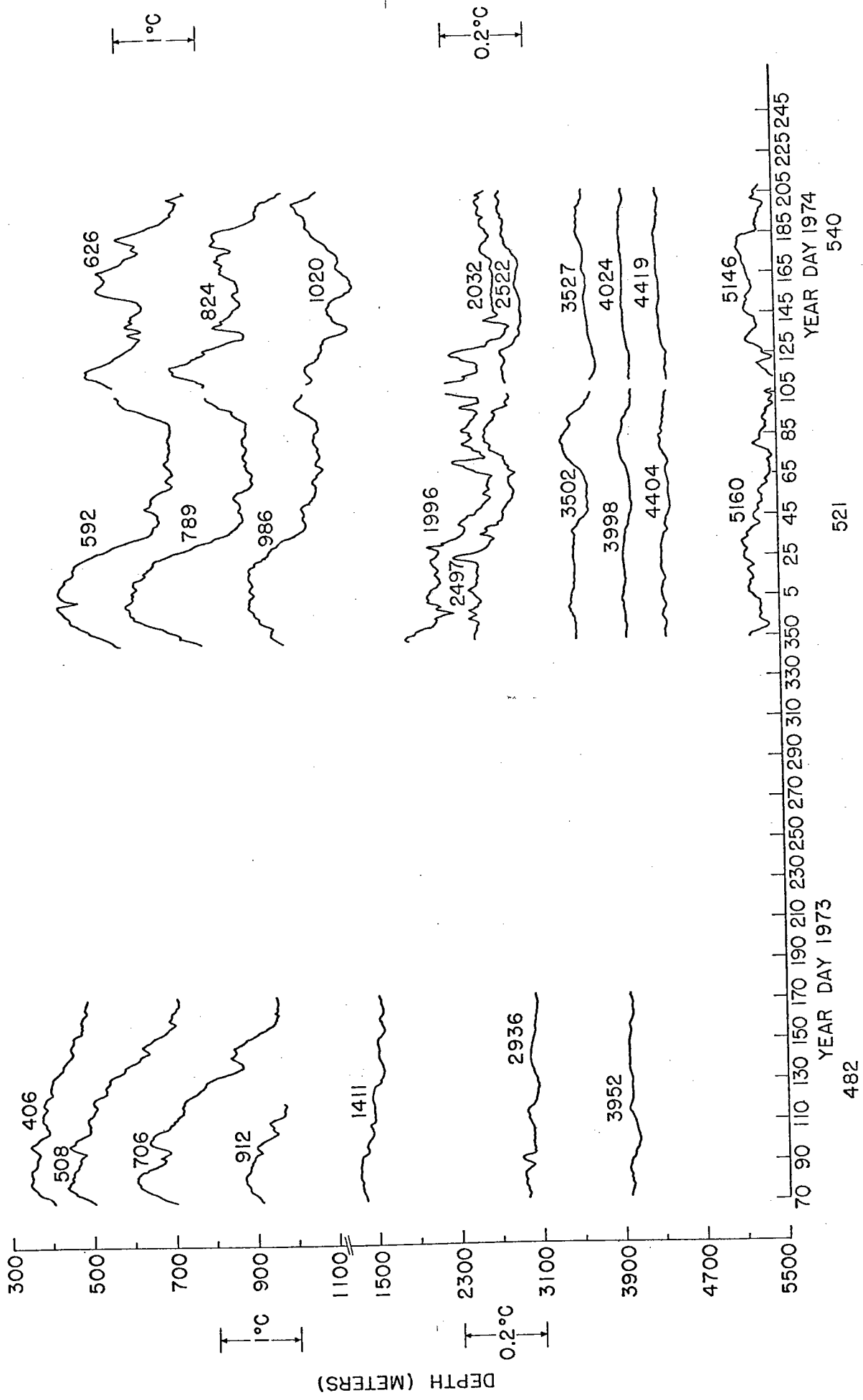


Figure I.2b: Temperature observations at MODE East

Visual inspection of the site mooring temperature records (see Figure I.2) shows some of the features of the low frequency fluctuations characteristic of the MODE region. During MODE-I, days 71 through 185 in 1973, the thermocline was dominated by an anticyclonic eddy with approximately 50 m depression of the isotherms. This eddy moved westward through the region at approximately 2 km/day. A similar isotherm depression of slightly greater amplitude is observed six months later, again appearing to occur earlier to the east. Later in 1975, a 50 m thermocline elevation, possibly a cyclonic eddy, is observed at MODE Center. In the deep water, below 3000 m, the magnitude of the thermal fluctuations is much less than in the thermocline, although the actual isotherm displacements are of similar magnitude. There is little visual similarity between the deep water and thermocline temperature fluctuations. Between 1500 m and 2500 m, the region of Mediterranean water influence, and very near the bottom, there is an apparent increase in the small time scale variability.

In an effort to characterize the mesoscale motions in the MODE region, we shall describe first the spatial variability of the temperature field. During the intensive MODE-I, the thermocline was dominated by a 50 to 70 km length scale eddy with approximately 16 day time scale. The length and time scales decreased with increasing depth. However, the time and length scales of a single eddy may

not be typical of the region. We shall address the question of typicality for the MODE region by considering the spatial variations over 100 km at the site moorings and the temporal variability of the velocity and temperature.

As we shall observe, the spectra of velocity and temperature in the MODE region may be separated into three regimes, very low frequency fluctuations with a dominance of zonal kinetic energy, an eddy energy containing band, and a high frequency region described by spectral similarity of the kinetic and potential energy. We shall compare the observed mesoscale variations with simple linear quasigeostrophic waves and with the results of Rhines' (1975, 1976) eddy spindown experiments to consider the possible dynamics of the motions.

While we generally cannot determine the actual dynamics of the flow, we can use the kinematics to speculate about the possible dynamics. In the eddy spindown experiments without topography and energy dissipation, a field of existing eddies evolves into a zonally anisotropic barotropic flow. The presence of topography can induce inhomogeneity and anisotropy in the mesoscale fields. We note here that anisotropy is used in two senses, with regard to the velocity, to indicate a preferred direction of the flow and, with regard to spatial variations, to indicate a preferred direction for inhomogeneities in scales and energy levels. At very low frequencies, we shall observe a tendency towards the end state of the

spindown models, but the eddy energy containing band with eddy scale energy variations is not consistent with the models, possibly due to topographic effects. Thus, we can use the detailed description of the mesoscale eddies in a small region of the ocean to explore the potential relevance of dynamical models of the flow.

II. Mesoscale Spatial Variability

During MODE-I, a synoptic picture of a mesoscale eddy is obtained. In this chapter, we shall use objective maps of the temperature field to present a qualitative description of the eddy and then estimate the horizontal and vertical length scales of the fluctuations. Because a single event is not necessarily typical of the variability of the eddy field, we shall consider the variation of the eddy kinetic and potential energy at the much longer site moorings to compare with the single eddy present during MODE-I.

II.1 Objective mapping of temperature

The isotherm distribution at a given level may be interpolated from the moored temperature observations by the technique of objective mapping (Gandin, 1965 and Bretherton, et al., 1976). For a scalar field the maps are obtained by minimizing the mean square error of the estimate $\hat{\varphi}$ of the field φ

$$\xi = \overline{[\varphi(x, y) - \hat{\varphi}(x, y)]^2} \quad (\text{II.1.1})$$

where the overbar denotes an ensemble average. For a field φ with known covariance function

$$F(\underline{\Delta}) = (\varphi(\underline{x}) - \bar{\varphi})(\varphi(\underline{x} + \underline{\Delta}) - \bar{\varphi}) \quad (\text{II.1.2})$$

the least squares estimate of the field is

$$\hat{\varphi}(x, y) = \bar{\varphi} + \sum_r F(\underline{x} - \underline{x}_r) \left[\sum_s A_{rs}^{-1} (P_s - \bar{\varphi}) \right] \quad (\text{II.1.3})$$

where

$$\bar{\varphi} = \sum_r \sum_s A_{rs}^{-1} P_s / \sum_r \sum_s A_{rs}^{-1} \quad (\text{II.1.4})$$

is the estimate of the mean, p_s is the observed value of the field at \underline{x}_s

$$p_s = \varphi(\underline{x}_s) + \varepsilon_s \quad (\text{II.1.5})$$

ε_s is uncorrelated white noise, and A_{rs}^{-1} is the r, s element of the inverse of the correlation matrix of the observations

$$A_{rs} = p_s p_r = F(\underline{x}_r - \underline{x}_s) + \varepsilon^2 \delta_{rs} \quad (\text{II.1.6})$$

The error variance of the field estimate is

$$(\varphi(\underline{x}) - \hat{\varphi}(\underline{x}))^2 = F(0) - \sum_r \sum_s F(\underline{x} - \underline{x}_r) A_{rs}^{-1} F(\underline{x}_s - \underline{x}) + \frac{(1 + \sum_r \sum_s F(\underline{x} - \underline{x}_r) A_{rs}^{-1} p_s)^2}{\sum_r \sum_s A_{rs}^{-1}} \quad (\text{II.1.7})$$

Objective mapping provides a technique for visualizing the development of the temperature field from a sparse set of moored observations using a known spatial correlation function. The statistics of the mesoscale temperature field are not known in advance. Since we want the objective maps to be smooth, we shall approximate the actual correlation function with an isotropic exponential function with a 100 km decay length. Experimentally, the results are insensitive in the accurate mapping region to the exact form of the correlation function used, though the error maps are sensitive. The observed correlation functions for the temperature during MODE-I will be discussed later in § II.5.2 and will seem to be roughly consistent with the model correlation function.

In cooperation with Dr. Nelson Hogg of the Woods Hole Oceanographic Institution 4 day temperature objective maps

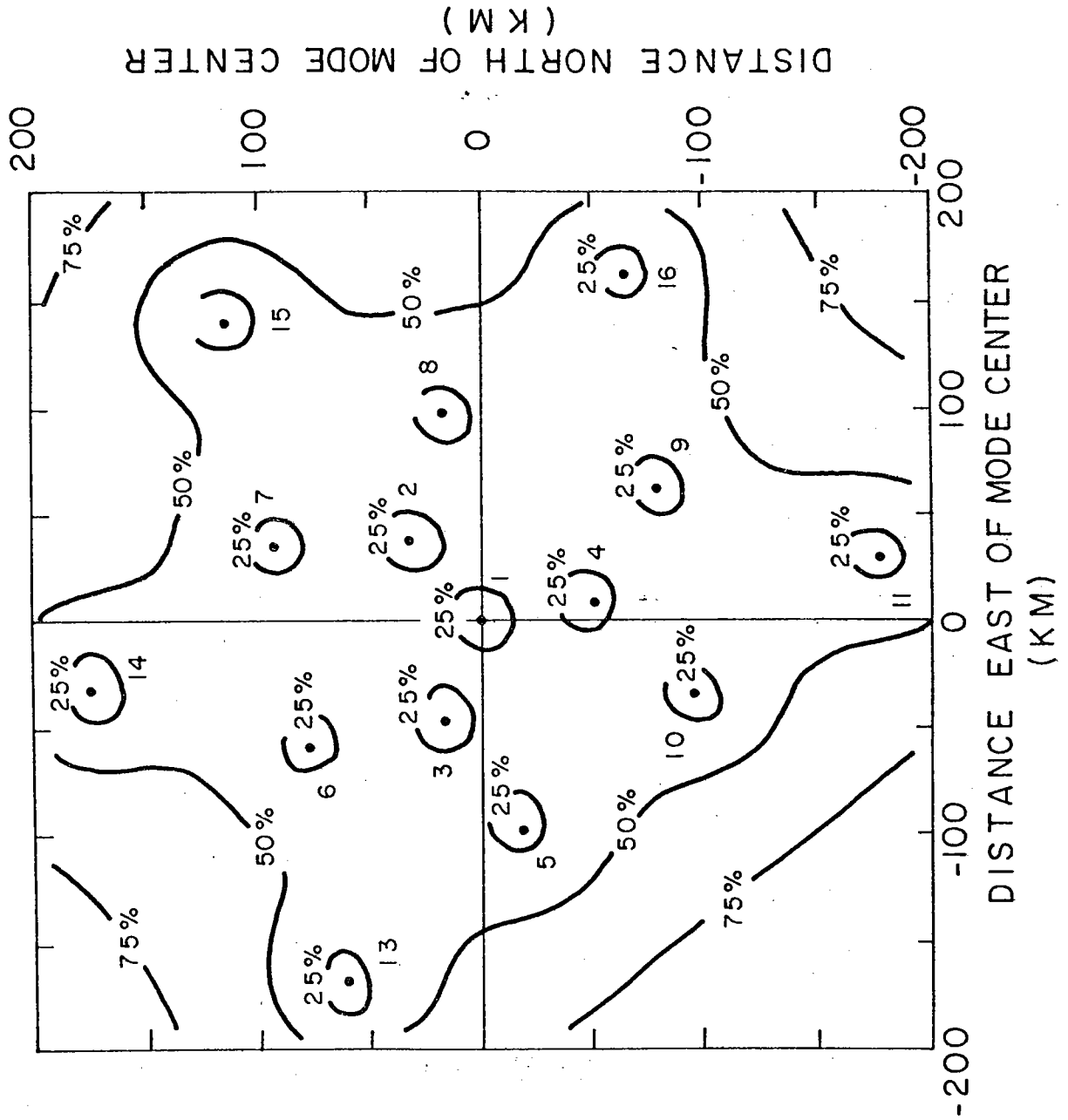


Figure II.1: Error variance for 515 m objective maps

at several levels were computed. Maps at four depth levels, shown in Figures II.2 and II.5, will be discussed. As a word of caution notice that the mapping technique tends to close contours on the periphery of the field. Thus, the shape of the field will be in part dependent on the location of the observations. A map of the error variance at 515 m when all the moorings are included is shown in Figure II.1. The 50% error contour is a reasonable guide to where the isotherm estimates become unreliable. Mooring deployment was spaced over two cruises and not until day 97 (April 7, 1973) are all the observations at a given level included in the maps. Hence, error maps are a function of time.

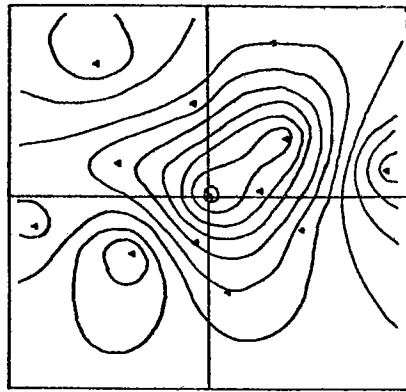
Thermocline

Initially in the thermocline at 418 m and 515 m there is a warm core eddy in the eastern half of the array. Although the maps show an east-west elongation, it is not possible to determine reliably the size or shape of the eddy at this early stage of the experiment. Around day 91 a sharp warming occurs at the central mooring of the array (mooring 1 at 28°N , $69^{\circ}40'\text{W}$) represented in the maps by an intensification of the warm core at this point.

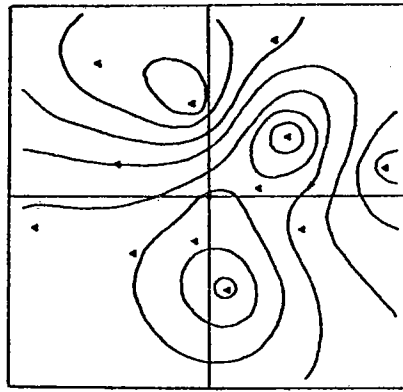
During the period of days 93 to 96 the mooring deployment was completed. The maps now have more structure with a double maximum of the warm core along a NW-SE line at 418 m. The main thermocline eddy is positioned at the array center with a longitudinal width of nearly 400 km and a latitudinal width of nearly 250 km. Little westward motion

Figure II.2: Objective maps of temperature in the MODE region. The maps are drawn on a 400 km square centered on mooring 1 (28° N, $69^{\circ}40'$ W) with the moorings located by triangles.

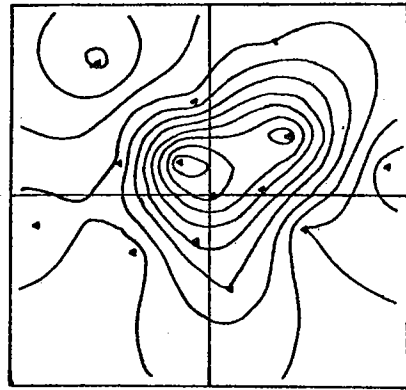
- a) 418 m temperature (0.1° C contour interval)
- b) 515 m temperature (0.25° C contour interval)
- c) 1420 m temperature (0.05° C contour interval)
- d) Phase diagrams along 28° N and $69^{\circ}40'$ W



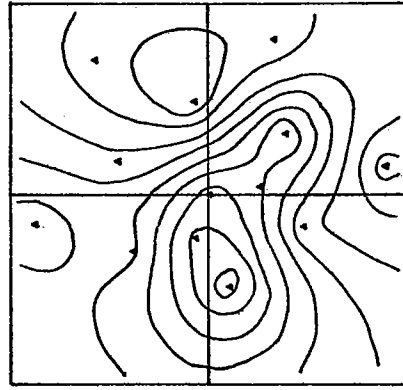
DAYS 121 TO 124



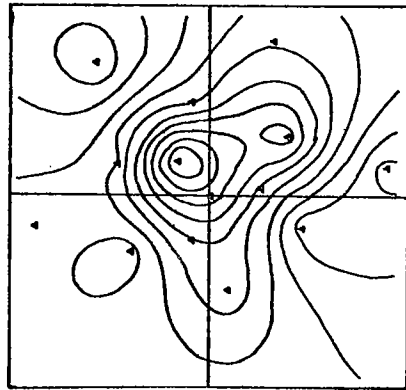
DAYS 173 TO 176



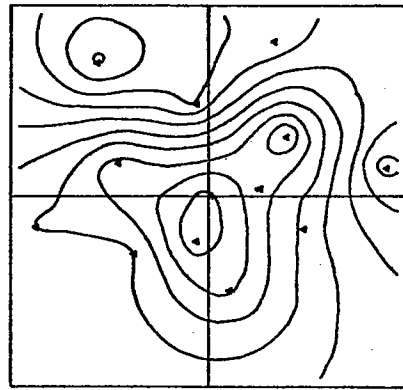
DAYS 109 TO 112



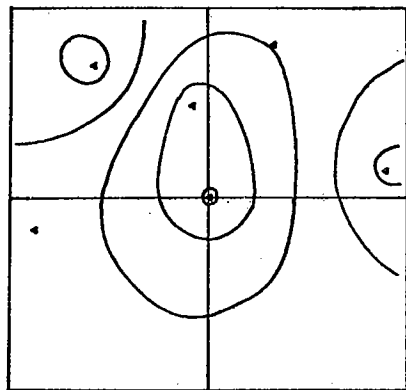
DAYS 157 TO 160



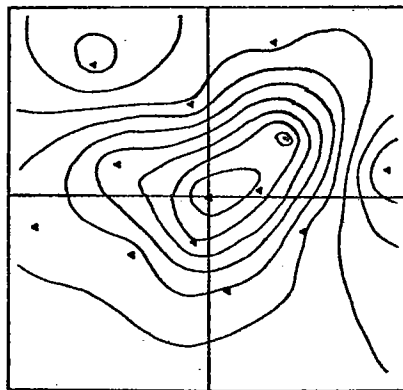
DAYS 97 TO 100



DAYS 145 TO 148

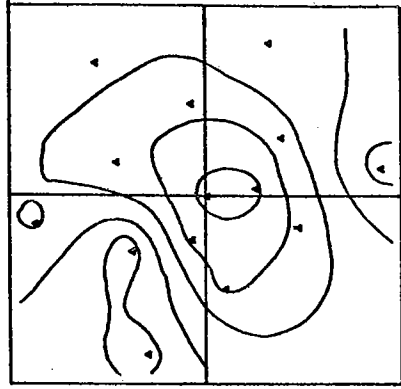


DAYS 85 TO 88

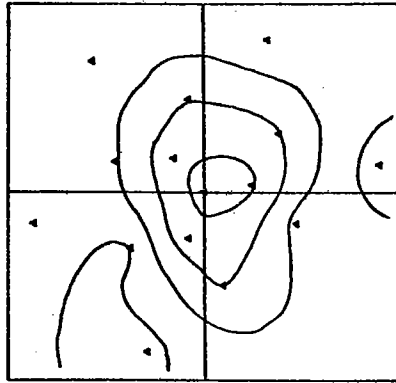


DAYS 133 TO 136

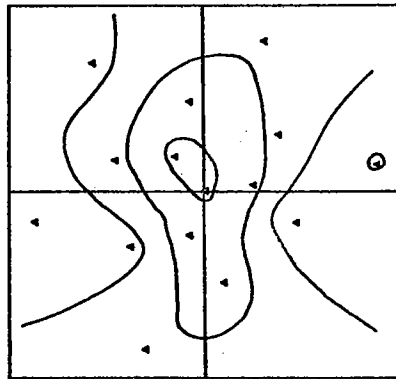
Figure II.2a



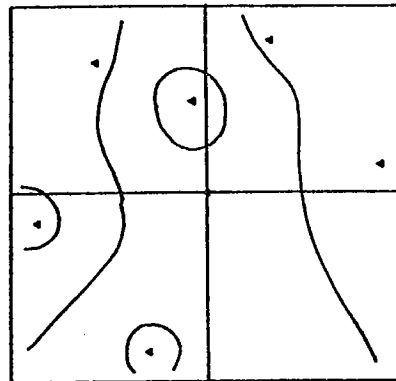
DAYS 121 TO 124



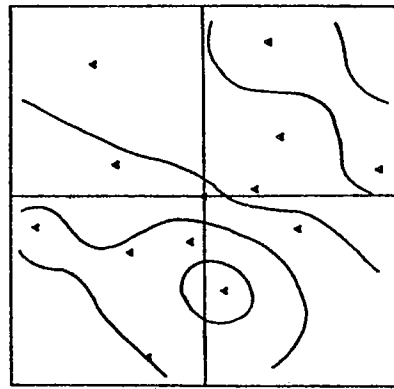
DAYS 109 TO 112



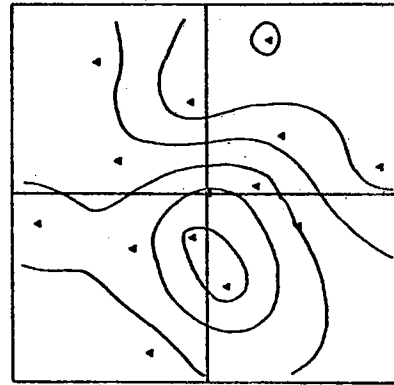
DAYS 97 TO 100



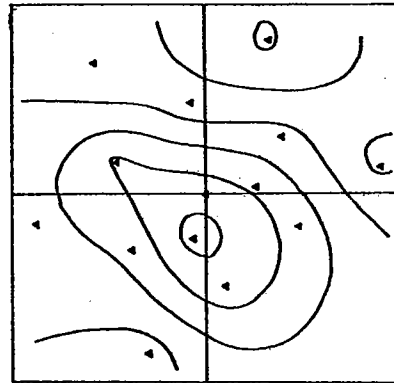
DAYS 85 TO 88



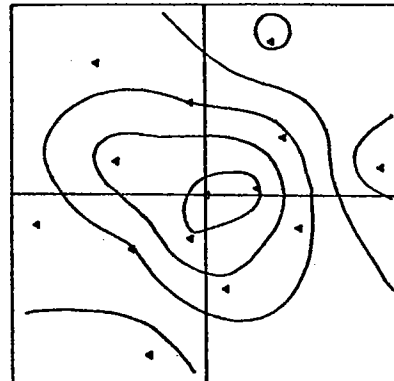
DAYS 173 TO 176



DAYS 157 TO 160

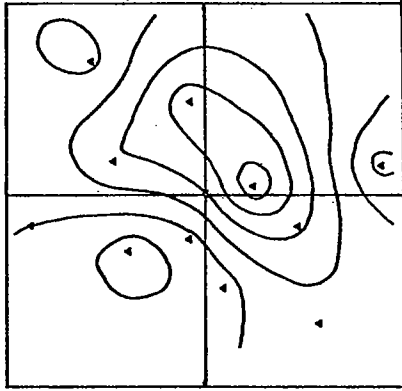


DAYS 145 TO 148

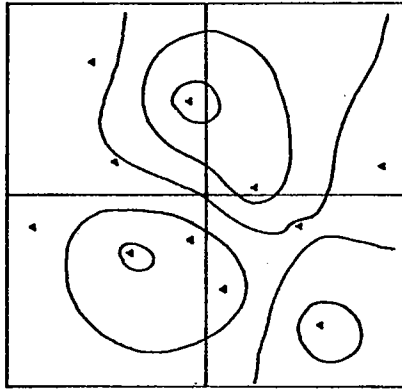


DAYS 133 TO 136

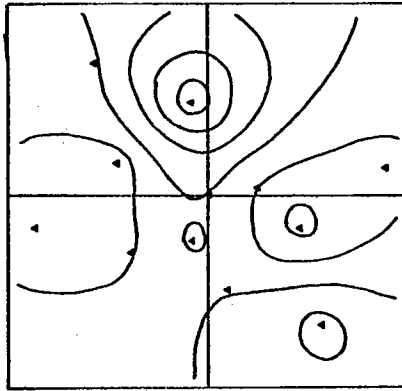
Figure II.2b



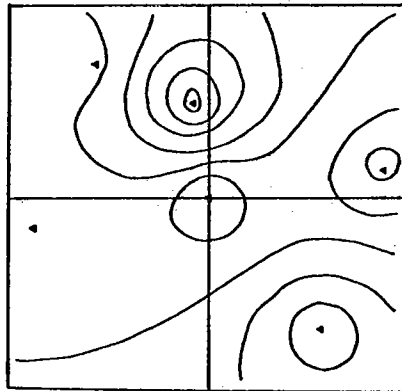
DAYS 121 TO 124



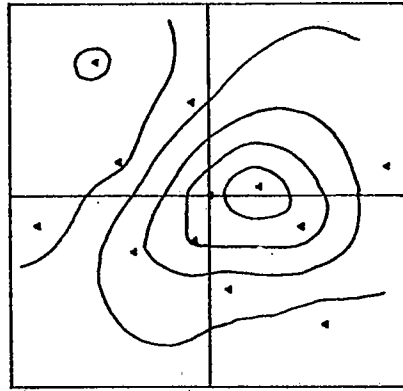
DAYS 109 TO 112



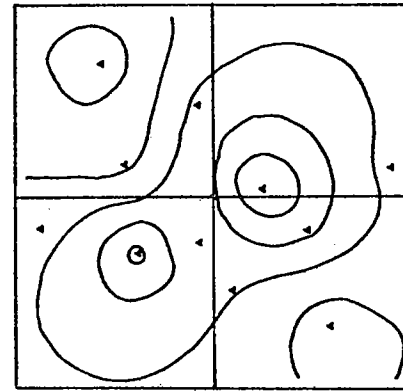
DAYS 97 TO 100



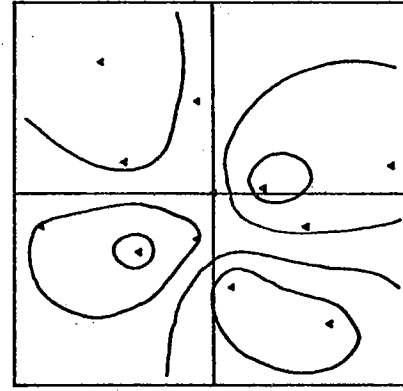
DAYS 85 TO 88



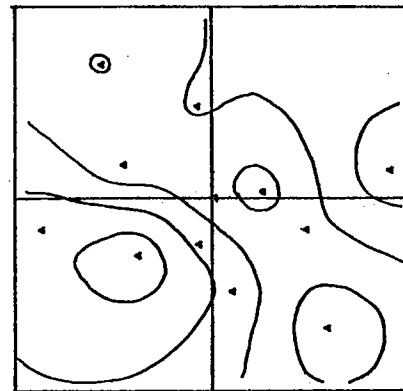
DAYS 173 TO 176



DAYS 157 TO 160



DAYS 145 TO 148



DAYS 133 TO 136

Figure II.2c

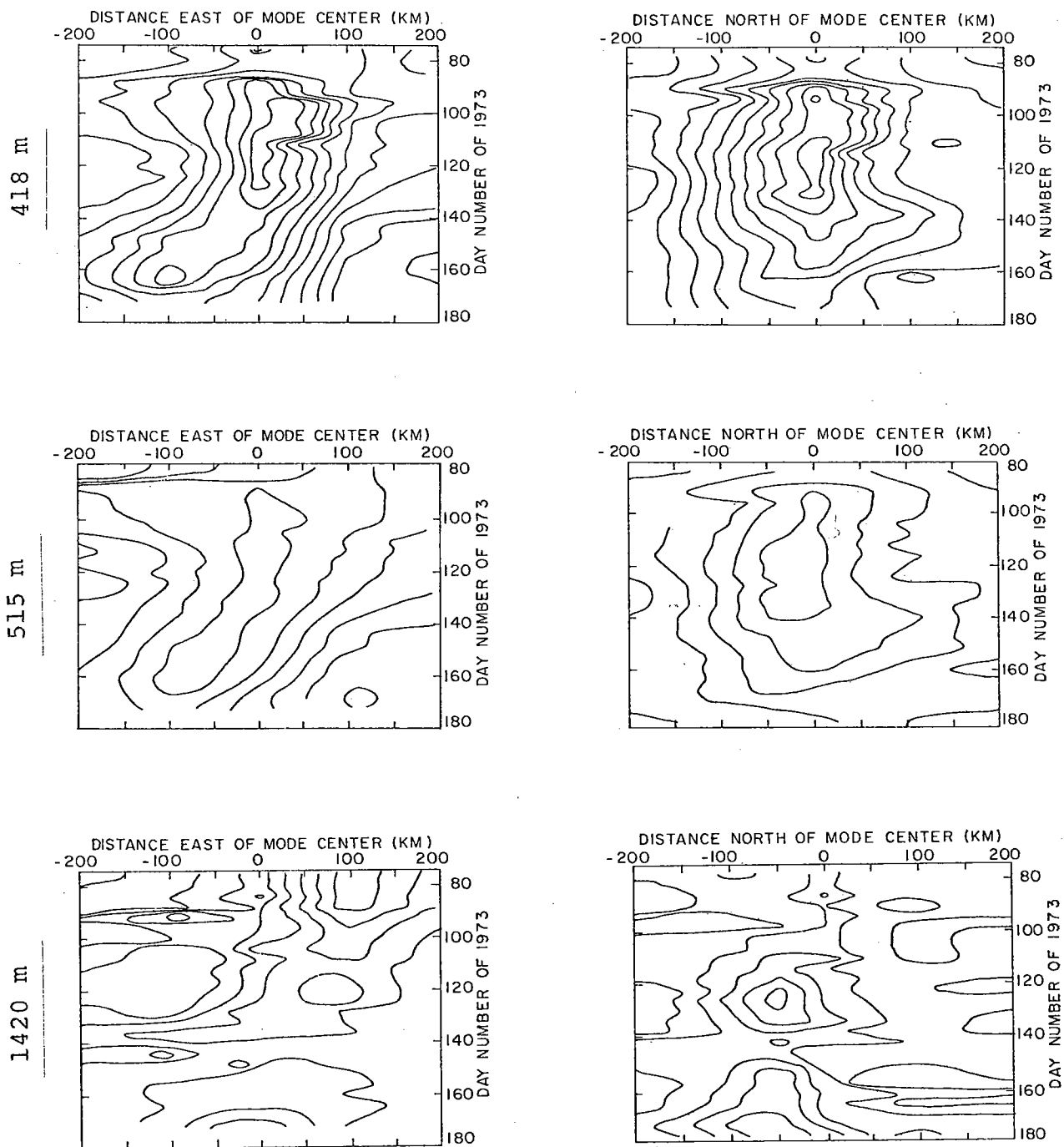


Figure II.2d

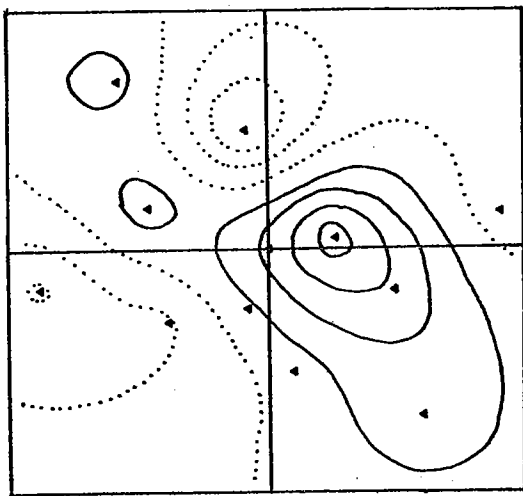
of the eddy occurs during the next month. Throughout the experiment as the warm core moves westward at 418 m the eastern temperature maximum weakens but never disappears. The warm core in the main thermocline at 515 m and the western maximum at 418 m move through the array disappearing out of the array to the west.

Mediterranean water

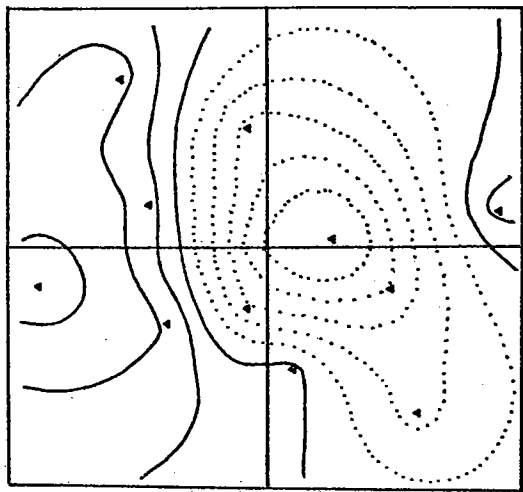
The temperature field at 1420 m could be described as a cold trough along a NNW-SSE line moving very slowly westward with superimposed smaller scale fluctuations. Unlike the main thermocline where no spatial mean temperature variation is obvious during MODE-I, in the region of Mediterranean water influence at the base of the thermocline the mean field variation is twice the spatially averaged rms temperature fluctuations. The mean spatial structure during MODE-I obscures the features of the fluctuating field in the maps. To avoid this difficulty the temperature fluctuations are mapped in Figure II.3.

Initially in the fluctuating field there is a warm core eddy in the eastern half of the region. This warm core eddy moves westward - corresponding to a weakening of the cold trough in the mean field - and moves entirely across the array. A cold eddy follows the warm eddy and corresponds to a deepening of the cold trough at the end of the experiment. The resemblance of the fluctuating field to the main thermocline is greater than that of the

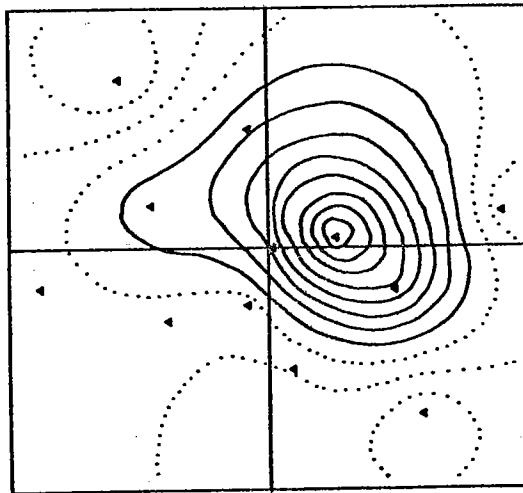
Figure II.3: Objective maps of 1420 m temperature fluctuations (25 m°C contour interval with dashed contours negative fluctuations) (a) and x-t phase diagrams for 1420 m temperature fluctuations along 28° N (b)



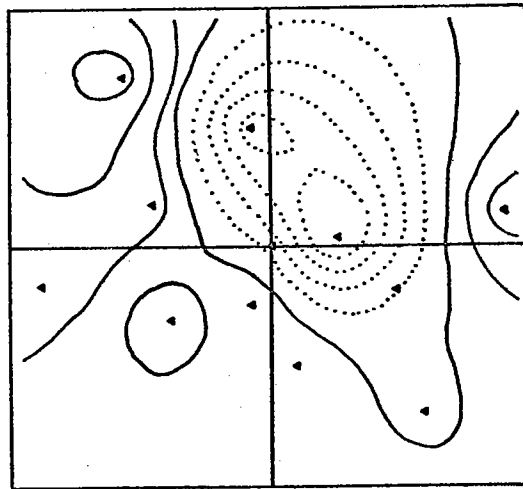
DAYS 133 TO 136



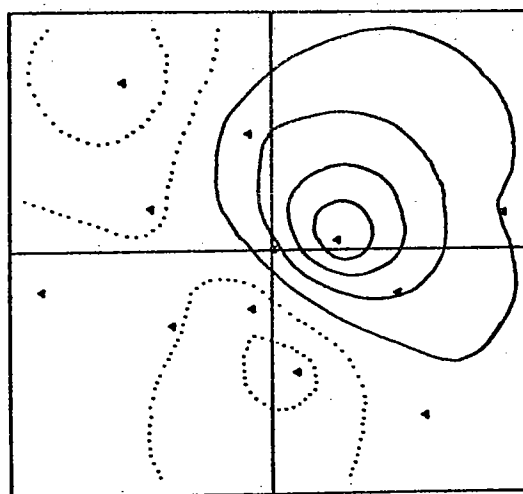
DAYS 173 TO 176



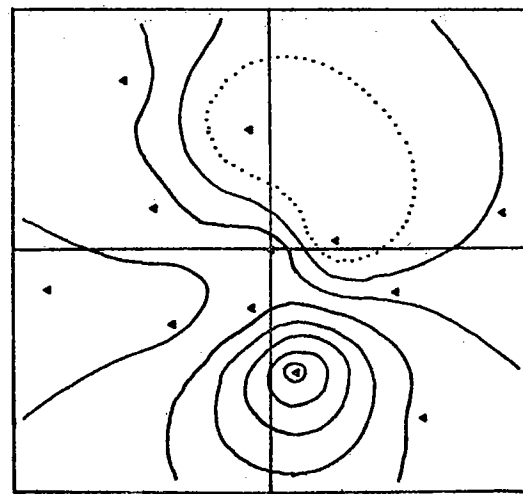
DAYS 121 TO 124



DAYS 157 TO 160



DAYS 109 TO 112



DAYS 145 TO 148

Figure II.3a

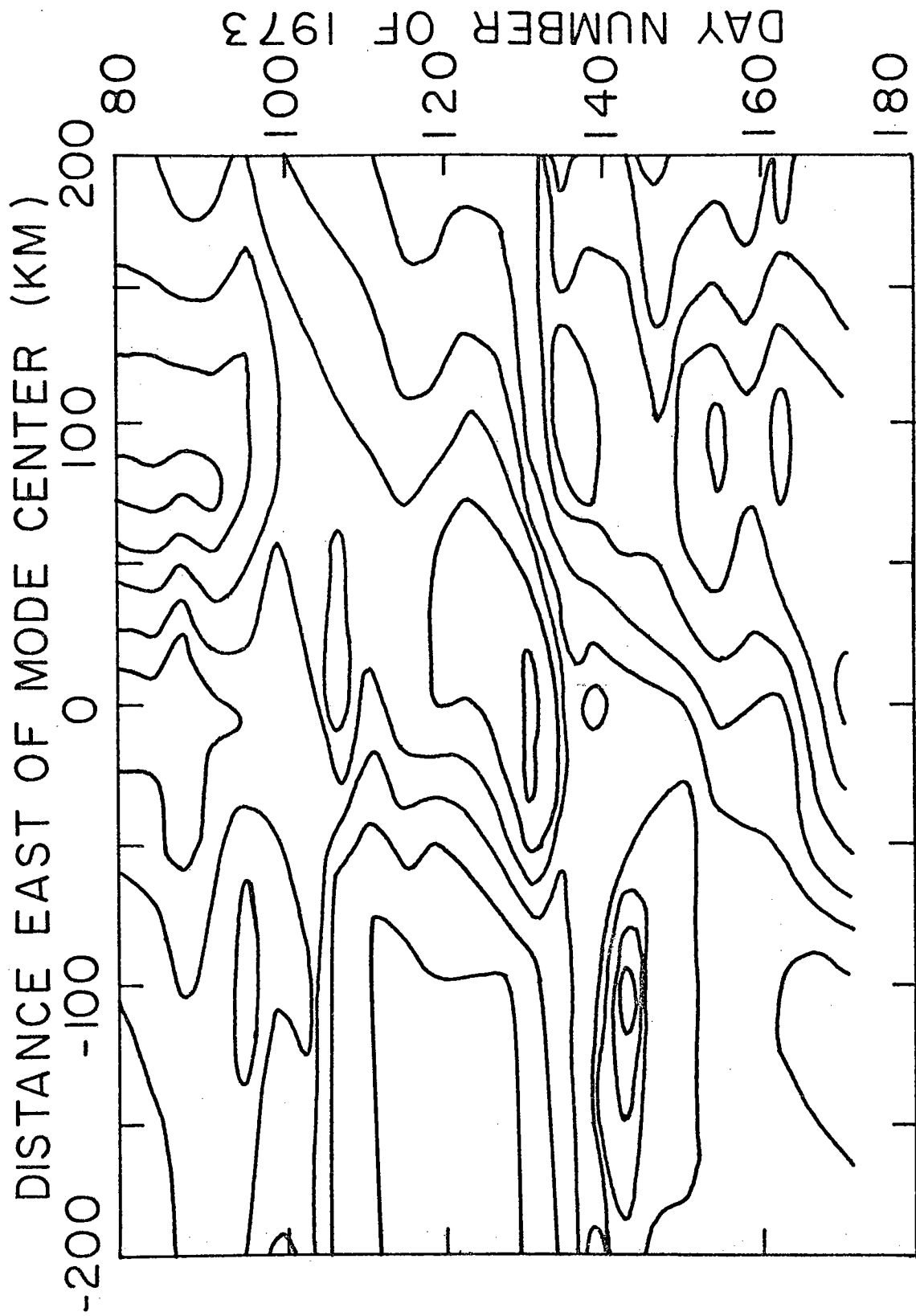
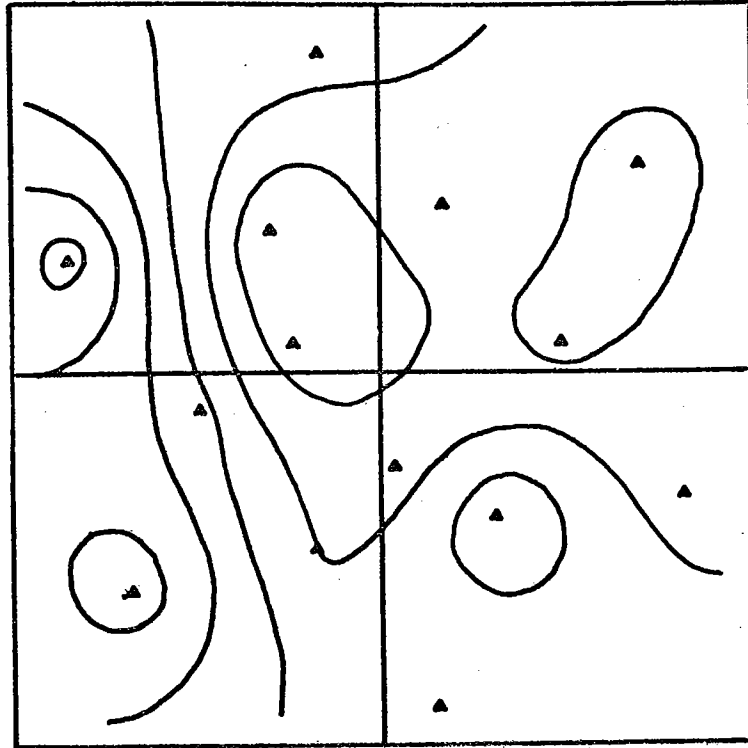


Figure II.3b

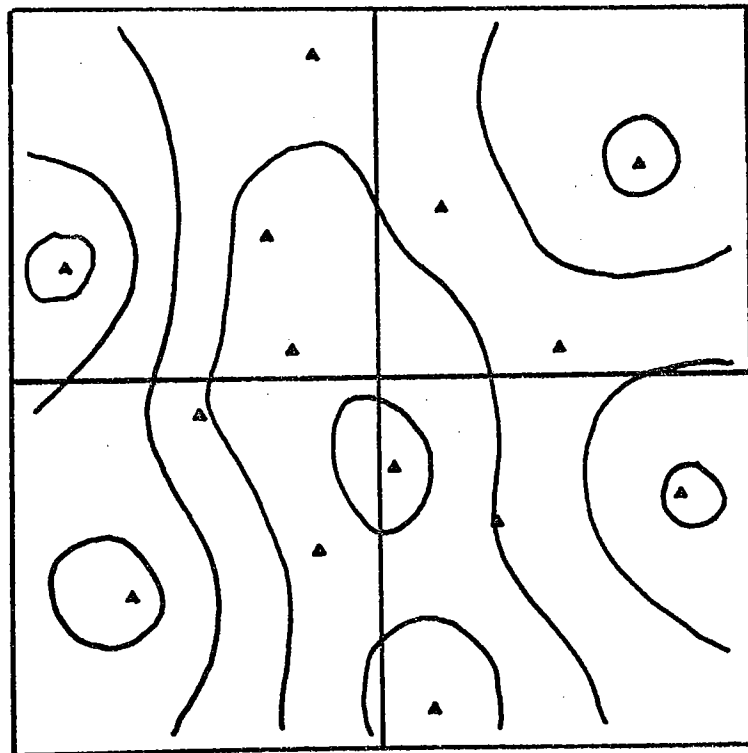
absolute temperature field. However, the apparent horizontal scale of the eddy field at 1420 m is shorter than in the thermocline. In addition to the two eddies observed, there are smaller scale thermal events on the periphery of the mapping region possibly associated with the small time scale variability seen in Fig. I.2. Because of the loose T-S correlation, temperature fluctuations can occur in the Mediterranean water without an actual density change (see Appendix A). No correlation of the small scale temperature fluctuations is observed over 100 km spacing (Hayes, 1975). Thus, the small scale thermal events in the maps may be patches of Mediterranean water advecting along density surfaces, while the larger scale fluctuations are assumed to be associated with the mesoscale circulation.

Deep water

In the deep water as in the Mediterranean water, an apparent mean spatial variation of the temperature field obscures the fluctuations in the maps. The mean spatial variation in the deep water resembles the cold trough at 1420 m as can be seen in two objective maps near the beginning and end of MODE-I in Figure II.4. However, we should note that the instruments have possible thermistor offsets of 10 to 20 m°C, which makes the detection of a weak, order 20 m°C, trough structure unreliable. A systematic raising of the temperature at cold instruments and lowering at warm instruments by increments within the



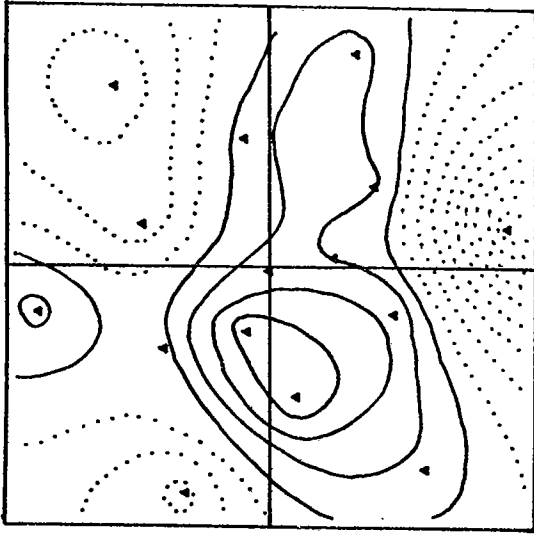
DAYS 101 TO 104



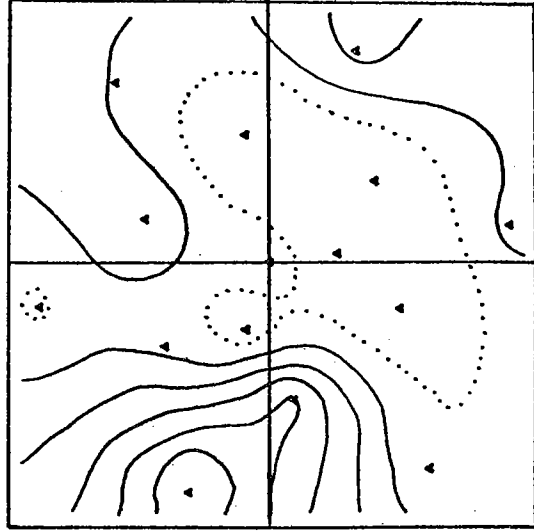
DAYS 169 TO 172

Figure II.4: 4000 m temperature objective maps

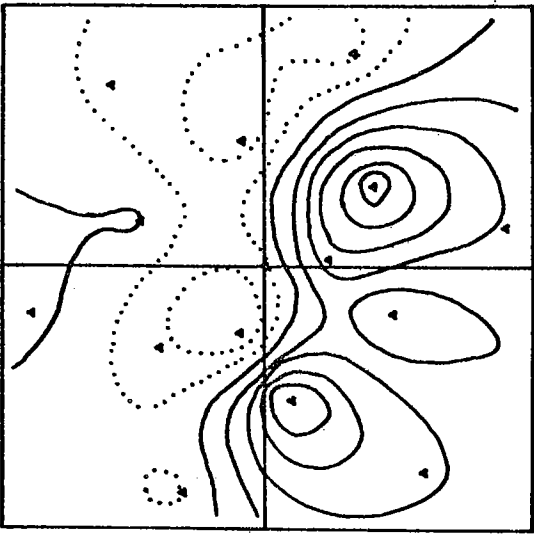
Figure II.5: Objective maps of 14 day average temperature fluctuations at 4000 m (2 m°C contour interval with dashed contours negative fluctuations)



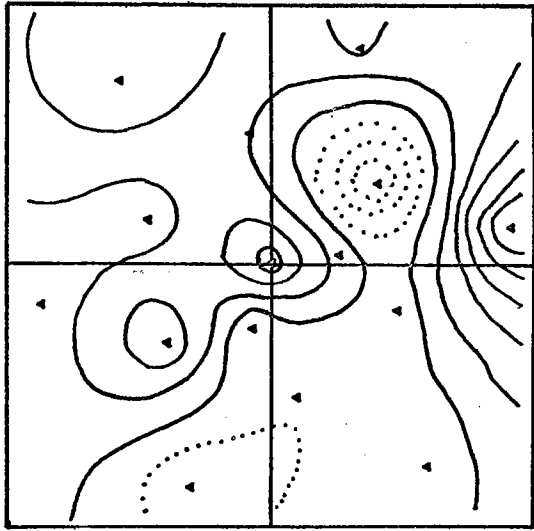
DAYS 118 TO 132



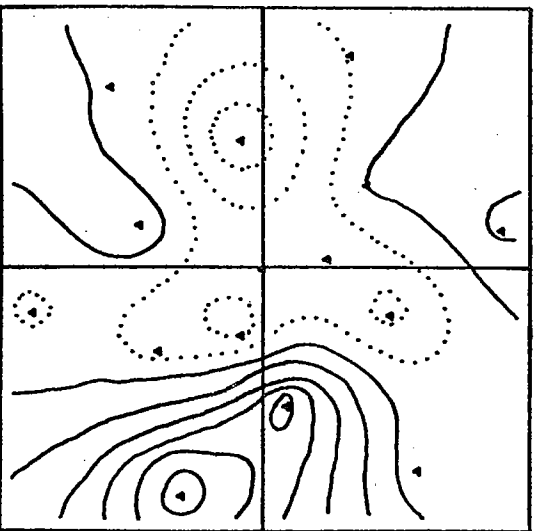
DAYS 163 TO 177



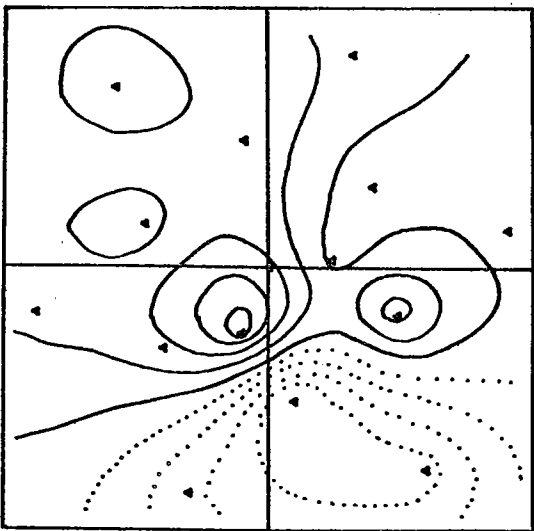
DAYS 107 TO 117



DAYS 148 TO 162



DAYS 88 TO 102



DAYS 133 TO 147

expected offset range could level the mean field.

To avoid difficulty with the mean spatial variation in the deep water, objective maps of the two week average deviations from the mean temperature at a mooring during MODE-I are shown in Figure II.5. Initially a cold pool dominates the abyssal hills and part of the abyssal plain with a warm pool to the west over the base of the Outer Rise. Warm water intrudes from the south during the next two weeks with the cold pool spreading westward to cover the northern half of the array. Between days 118 and 132 a cold event occurs at the southernmost mooring. The warm pool now dominates the center of the region. This warm pool diffuses over most of the array with a cold pool forming over the Outer Rise. Between days 148 and 162 a warm event occurs at the southernmost mooring. The last map shown is similar to the beginning of MODE-I.

No westward motion is evident in the deep temperature field. The deep water appears as weak warm and cold pools superimposed on a quasipermanent trough structure in a manner unlike the Mediterranean water where the temperature fluctuations clearly moved westward across a similar quasipermanent trough structure. Length and time scales for the fluctuating deep water pools are shorter than the eddy length and time scales in both the main thermocline and Mediterranean water, even though the same correlation function is used to draw the maps at all depth levels.

Phase diagrams

A dominant feature of the temperature field maps is the westward motion of the eddy. Using the maps we can construct east-west and north-south phase diagrams along 28°N and $69^{\circ}40'\text{W}$ respectively. We note in advance that some sharp variations in the phase diagrams will be an artifact of the array sampling and objective mapping technique. The phase diagrams are noisy until after day 94 when all the moorings are in place.

The motion of the main thermocline pattern cannot be described by a constant westward velocity (Figure II.2d). During the early part of MODE-I the phase speed is approximately 1.2 km/day increasing to 3.3 km/day after day 130. Mean pattern velocity during MODE-I is 2.2 km/day. There is no appreciable north-south motion of the main thermocline eddy.

Freeland and Gould (1976), assuming the observed velocity field is horizontally non-divergent and may be represented by the curl of a streamfunction, find a westward phase speed of 2.2 km/day for the pattern motion of the objectively mapped streamfunction consistent with the temperature pattern motion. The maps of temperature and streamfunction in the thermocline are visually similar. Later, we shall observe for quasigeostrophic dynamics that the temperature (actually density) is the vertical derivative of the streamfunction.

In the Mediterranean water, westward motion of the eddy at 2 to 3 km/day is apparent in both the absolute temperature field (Figure II.2d) and in the deviation temperature field

(Figure II.3b). However, at this depth, Freeland and Gould find a streamfunction phase speed of 5.1 km/day and there is little visual similarity with the temperature maps.

In the deep water, no westward motion of the temperature field is evident during MODE-I. No phase diagram for the deep water is shown because the short length and time scales make a sensible contouring of the diagram difficult. Unlike the temperature field, westward motion at approximately 5 km/day is evident for the geostrophic streamfunction (Freeland and Gould). We shall discuss later possible reasons for the differences in the deep temperature and velocity fields.

Summary

Objective maps of the temperature at four depth levels during MODE-I show that at two levels in the main thermocline a warm core eddy with length and time scales comparable to the duration of MODE-I moves westward at approximately 2 km/day. This eddy dominates the main thermocline temperature and no mean spatial variations in the MODE region are obvious. At the deeper levels, in the Mediterranean water and in the deep water, the magnitude of the time mean spatial variation of the temperature is comparable to the eddy field. In the Mediterranean water, the eddy field again moves westward at 2 to 3 km/day, but visual coherence with the main thermocline is low. Length and time scales of the temperature fluctuations decrease with depth. No westward propagation of the

temperature fluctuations is observed in the deep water where the low frequency temperature variations appear as small scale standing warm and cold pools superimposed on a larger scale mean field.

II.2 Statistical assumptions

In the previous section, the temperature field is dominated by an eddy with length and time scales comparable to the duration of MODE-I. We would like to know if the results from MODE-I are, in any sense, typical of the MODE region. It is obvious from the qualitative results already displayed that the field during MODE-I cannot be regarded as either spatially or temporarily homogeneous in all frequency bands. Among other things in this thesis, we are investigating the statistical properties of the very low frequency flow. The stability of the estimates of a statistical property can be determined if the probability distribution of the flow and the number of independent samples are known.

II.2.1 Probability distribution of temperature

In this section, we shall consider the degree to which the temperature can be considered a normally distributed process. The cumulative probability density distribution for the thermocline and deep water daily averaged temperature at MODE Center are shown in Figure II.6. For comparison to a gaussian distribution, the temperature has been

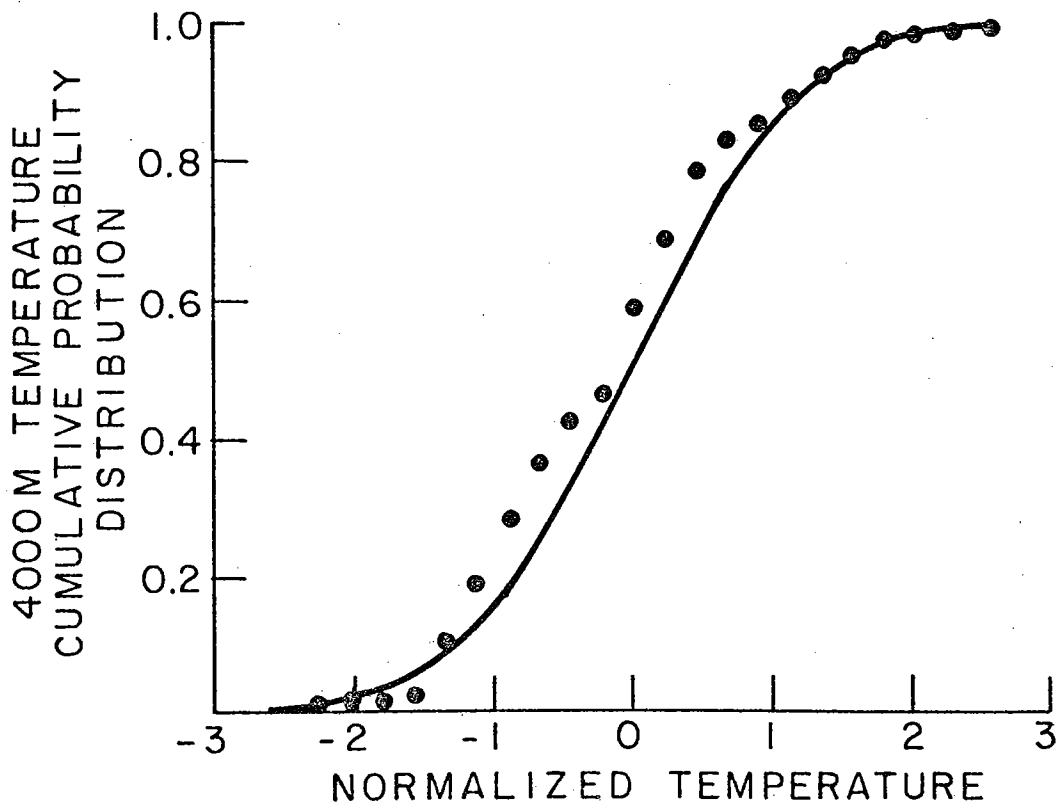
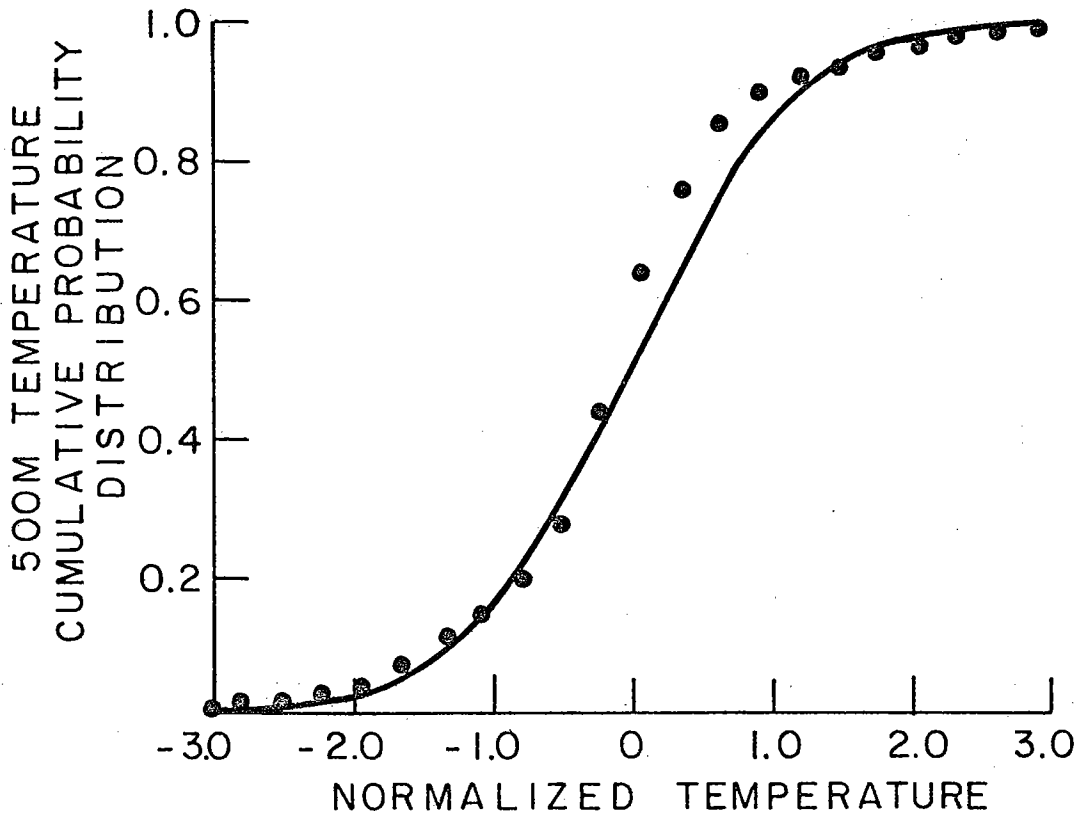


Figure II.6: Cumulative probability distributions for main thermocline and deep water temperature at MODE Center

normalized as follows

$$T'(t) = (T(t) - \bar{T})/\sigma \quad (\text{II.2.1})$$

where T' is the normalized temperature, T is the time mean temperature and σ is the sample standard deviation of the temperature. The temperature at each depth level is sorted into 23 bins to obtain the sample probability distribution. A simple test of the hypothesis that the temperature is normally distributed is given by the Kolmogorov-Smirnov goodness-of-fit test (Massey, 1951). A new random variable d with a known distribution is defined by

$$d = \text{maximum} (|S_n(x) - F(x)|) \quad (\text{II.2.2})$$

where $S_n(x)$ is the sample cumulative probability distribution for the random variable x , n is the number of independent observations, and $F(x)$ is the proposed distribution. The hypothesis is tested for the probability that d exceeds an expected deviation ϵ . For a large number of observations n , the expected deviation $\epsilon(\alpha, n)$ is given asymptotically by

$$\epsilon(\alpha, n) \sim \left[\frac{\ln(1/\alpha)}{2n} \right]^{1/2} \quad (\text{II.2.3})$$

where α is the probability that the deviation exceeds ϵ

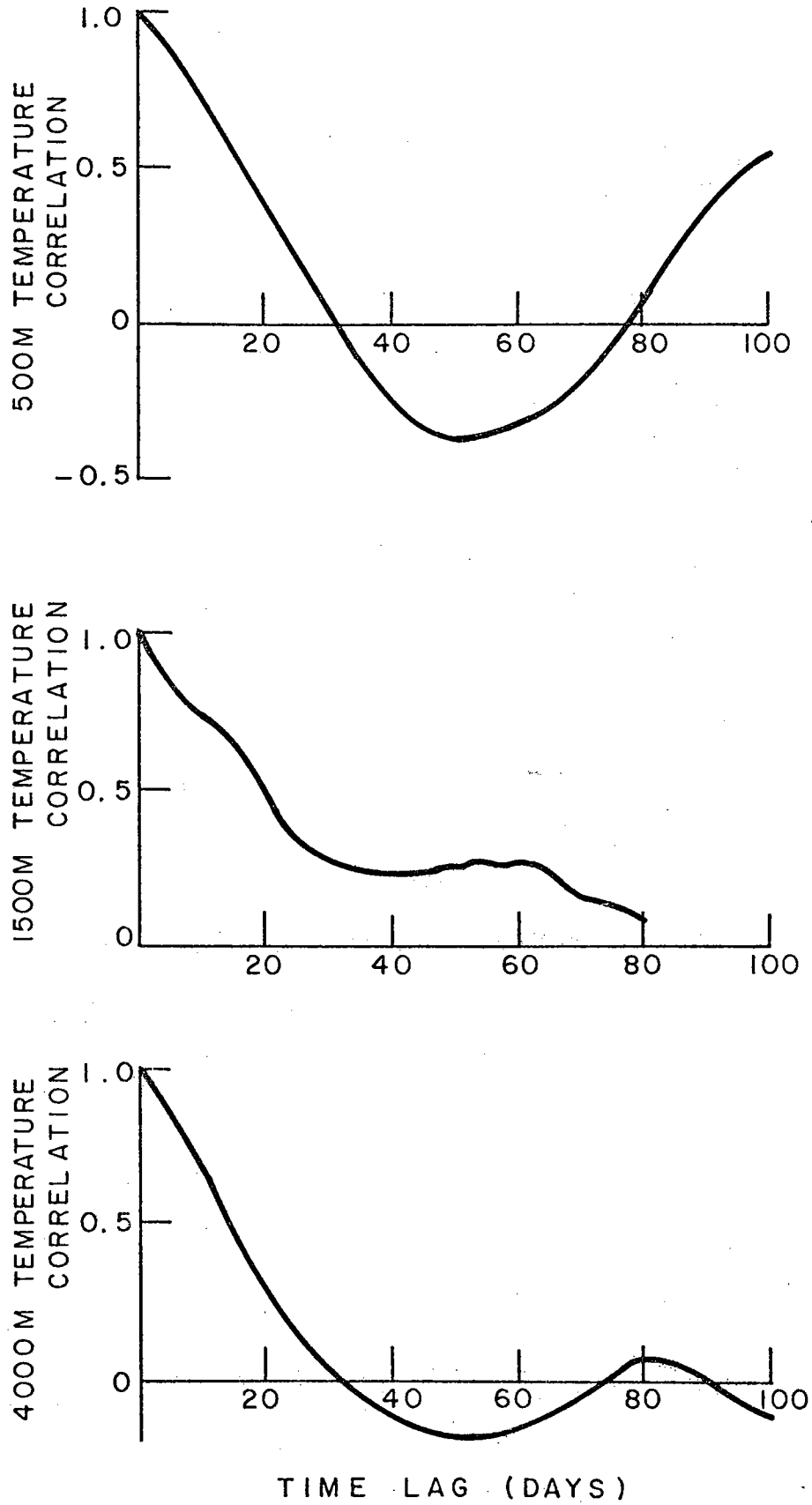


Figure II.7: Temperature autocorrelations at MODE Center

(Miller, 1956). To apply the K-S test for normality, we need to know the number of independent estimates in the sample probability distribution. If the data samples are not independent and the number of degrees of freedom overestimated, then the observed probability distribution might appear to deviate from normality based upon K-S statistics even though the process is gaussian.

The temperature at all depths is significantly correlated at time lags of 10 days and more (Figure II.7). The daily averaged temperature is obviously not independent. Now we want to obtain a rough measure of the correlation time for the daily averaged temperature to estimate the number of independent samples. One possible measure is the area under the correlation function, commonly referred to as the integral time scale (Taylor, 1921). However, when the correlation function contains large negative lobes such as the main thermocline temperature, the integral time scale is decreased while actually the field is correlated at larger time lags. Thus, the integral time scale seems inappropriate for the low frequency temperature field. Instead, we shall use an integral time scale based upon the square of the correlation. This time scale is a rough, somewhat ad hoc, estimate of the number of independent samples obtained by considering the behavior of the estimated correlation function at large time lags. If the true correlation at lag k , ρ_k , becomes negligibly small for all lags greater than m , then the variance of the

correlation estimate at lag k , r_k , for $k > m$, obtained from N samples is

$$\text{variance } (r_k) = N^{-1} \sum_{L=-m+1}^{m-1} \rho_L^2 \quad (\text{II.2.4})$$

(Kendall and Stuart, 1975). Now, for independent gaussian white noise, the variance of the correlation estimate is N^{-1} . Thus, if we assume that the variance of the estimated correlation function, when the true correlation is zero, depends only on the number of independent samples used in the estimate, then the square integral time scale is a measure of the time between independent samples.

Using the observed correlation function to estimate the square integral time scale, given in Table II.1, we find that the 36 day time scale in the thermocline is greater than the 23 day time scale in the deep water consistent with the qualitative estimates of the time scales from the objective maps. For 490 days of temperature, the numbers of independent samples are 13 and 21 in the thermocline and deep water respectively. Then using K-S statistics, the observed temperature distribution is not significantly different from gaussian at 95% confidence.

For both the thermocline and deep water the observed probability of small thermal fluctuations is greater than that of a normal process, although the difference is not significant. We may relate the deviations of the observed

Square integral correlation time scale
at MODE Center

Depth	Temperature	Zonal Velocity	Meridional Velocity
500 m	36.4	70.0	23.3
1500 m	32.4	20.4	27.8
4000 m	22.8	21.2	25.8

Table II.1: Number of days required for
independence of temperature and
velocity observations

probability distribution from a normal distribution to the higher moments of the temperature. If we define the excess E as

$$E = \langle T'^4 \rangle - 3 \quad (\text{II.2.5})$$

where T' is the normalized temperature given by II.2.1 and the skewness S as

$$S = \langle T'^3 \rangle \quad (\text{II.2.6})$$

then for a normal distribution both the skewness and the excess would be zero. The observed excess is negative for both the thermocline and deep water, although neither is significantly different from zero. The deep water and thermocline temperature are positively skewed, although again the skewness is not significantly different from zero at 90% confidence,

Several effects can cause the observed probability distribution to be non-gaussian, for example, intermittency and nonlinearity. If the temperature is dominated by an intermittent process, the observed excess would be positive (Monin and Yaglom, 1975). We reject the hypothesis that the low frequency temperature is intermittent, since the observed excess is not significantly different from zero. Significant deviations from normality could be caused by nonlinear dynamics in the mesoscale flow. Suppose the

temperature field is a random superposition of independent waves; then regardless of the exact nature of the probability distribution of the wave amplitudes, the field will tend to be normally distributed in the limit of a large number of waves. Nonlinear interactions will increase the correlations between waves. The time scale of the interactions compared to the dominant eddy time scale will be important in determining the magnitude of the deviations from normality. For weak interactions with small growth rates, dispersion of interacting wave groups will tend to decrease the correlations and prevent significant deviations from a basic gaussian state. We shall observe later that horizontal advection is an important contribution to the thermal balance.

The above discussion is limited to the temperature field. Similar results (not shown) apply to the velocity field. The velocity at all depths is significantly correlated at time lags of 10 days and more. Reducing the number of independent samples by the factors given in Table II.1, the observed probability distribution for the velocity is indistinguishable from a normal distribution. We also note that the time scale for the zonal flow in the thermocline is long, 70 days, while the time scales for the deeper zonal flow and meridional flow are nearly the same as the time scale of the deep water temperature and shorter than the zonal thermocline flow. This long time scale will decrease the stability of statistical estimates involving the zonal thermocline flow.

In later discussions of the scales and energy levels of the flow, we shall estimate the statistical stability of the results using a normal probability distribution with a reduced number of independent samples.

II.3 Horizontal variation of temperature

The objective maps of the temperature, discussed in section II.1, give a qualitative picture of the spatial and temporal variability during MODE-I. MODE-I is too short to yield a statistical description of the variability in the region. However, the detailed spatial coverage of MODE-I provides an unique opportunity to indicate potentially relevant length and time scales of motion.

II.3.1 Spatially averaged temperature spectra

Time scales of the temperature fluctuations can be estimated from the spectra. For a given depth level, the spectrum may be estimated by spatially averaging the periodograms. The power in the temperature fluctuations during MODE-I in both the thermocline and deep water is dominated by three time scales: semidiurnal, diurnal, and very low frequency.

In the deep water, the high frequency roll off of the temperature at the local buoyancy frequency, approximately 2.4 cph, can be observed (Figure II.8). In the thermocline, the highest resolved frequency is less than the local buoyancy frequency and the roll off cannot be observed. The

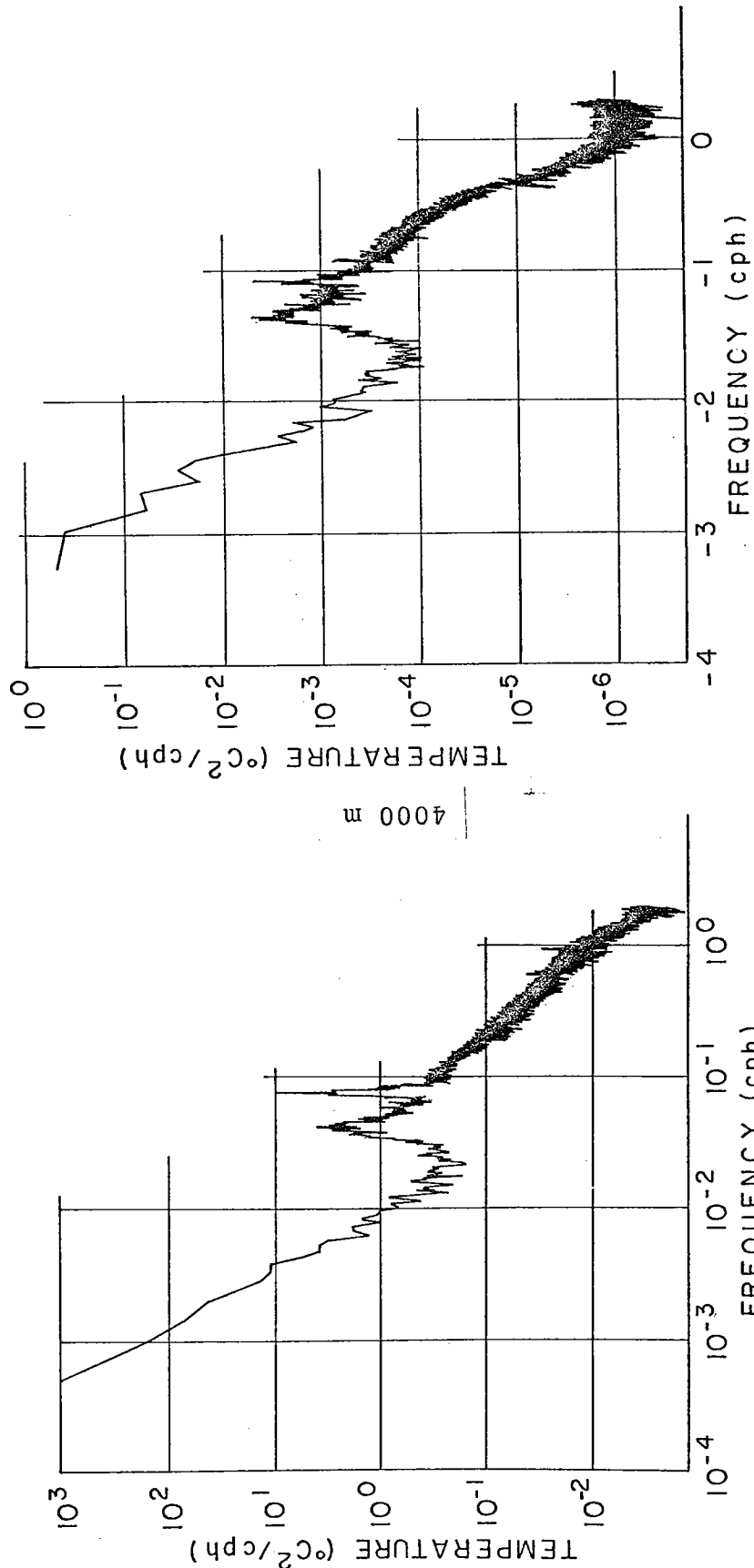


Figure II.8: Spatially averaged temperature spectra during MODE-I

deep water has a shorter low frequency time scale than the thermocline. While the thermocline spectrum is still "red", with the power increasing with decreasing frequency, to periods of 83 days, the deep water spectrum begins to level off at periods greater than 42 days. The low frequency variance cannot be measured during MODE-I, but the spectra suggest a time scale of 16 days and greater in the thermocline and a potentially shorter 7 days and greater in the deep water. Wunsch (1972) computed the power spectrum of the main thermocline temperature fluctuations at Bermuda where the spectrum is red to periods of nearly two years. However, most of the power in the spectrum is in the period band between 50 and 200 days. Later, using the site mooring data, we shall discuss the very low frequency variance unresolved by MODE-I.

The temperature variance levels are not directly comparable because the temperature gradient changes by almost two orders of magnitude between the thermocline and deep water. For comparison, the temperature spectra are divided by the cube of the buoyancy frequency and shown in Figure II.9. The above scaling follows from the WKB approximation to the high mode vertical structure of linear quasigeostrophic motions in a flat bottomed ocean (c.f. section IV.1). For the WKB scaling, an available potential energy, defined by

$$PE = g \alpha / 2 \overline{T'^2} \left(\frac{d\Theta}{dz} \right)^{-1} \quad (\text{II.3.1})$$

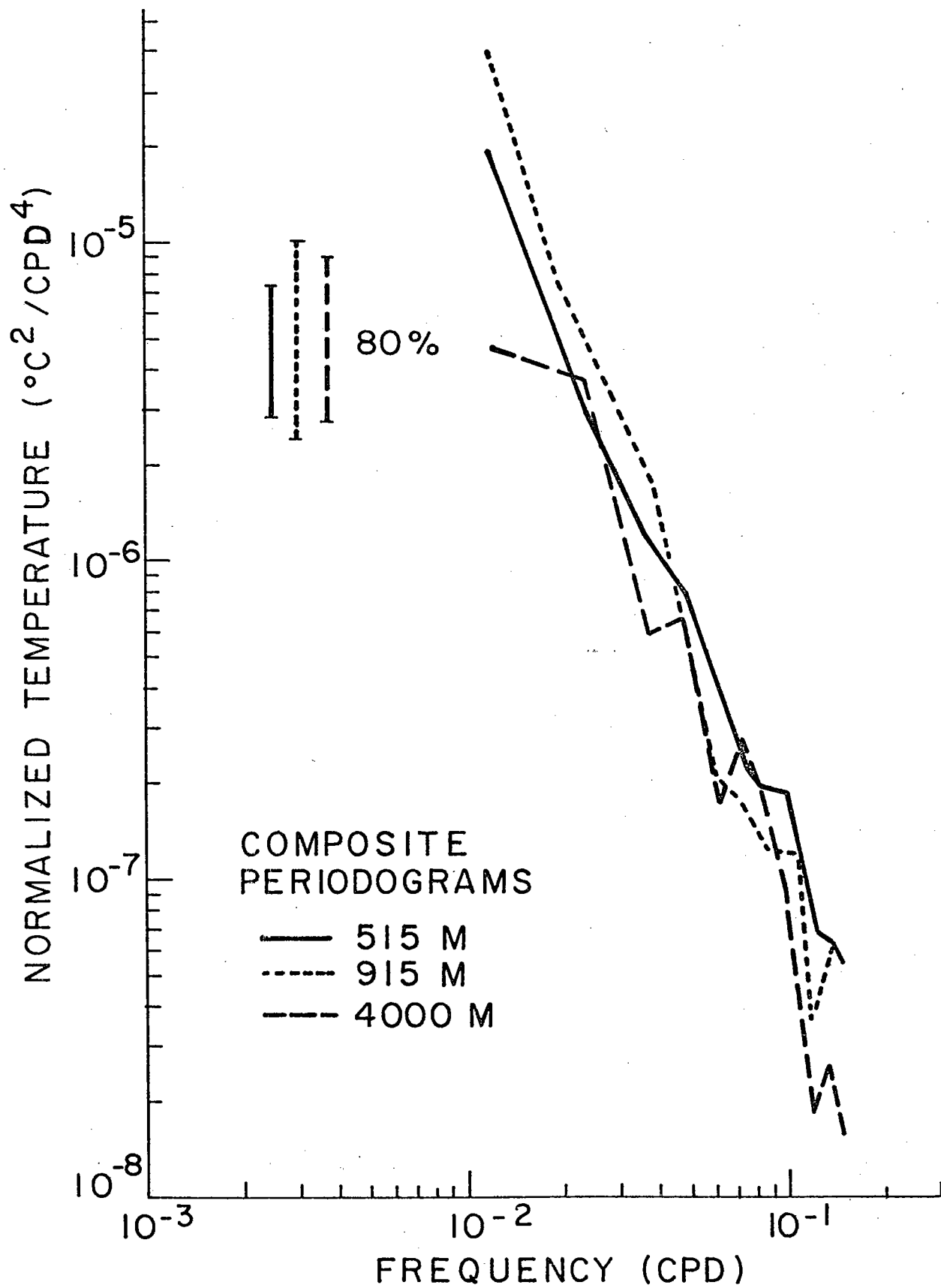


Figure II.9: WKB normalized composite temperature spectra

where α is the thermal expansion coefficient including the effects of salinity from a tight θ -S correlation and $\frac{d\theta}{dz}$ is the vertical potential temperature gradient, should vary as the buoyancy frequency and the isotherm displacement as the inverse square of the buoyancy. For periods less than 30 days the temperature spectra scale in the WKB sense at the 90% confidence level. For the confidence limits shown in Figure II.9, each instrument is assumed independent with 15 instruments at 515 m, 7 at 915 m and 10 at 4000 m. The independence assumption is reasonable for periods less than 30 days where the coherence between instruments is insignificant for separations greater than 50 km (the smallest instrument separation). However, for lower frequencies, the coherence between instruments is not negligible. Using equation II.2.4 and the isotropic correlation functions in section II.3.2, the estimate of the number of degrees of freedom in the spectra is reduced to approximately 4 in the thermocline and deep water.

For periods less than 30 days, the spectra in both the thermocline and deep water may be described by a power law indistinguishable from ω^{-3} , consistent with the results of Wunsch (1972) for the main thermocline at Bermuda. However, we note again that the very low frequency variance is not resolved during MODE-I. The main thermocline spectra are indistinguishable from the spectrum of a sine wave with

period twice the duration of MODE-I. If the very low frequencies are determining the shape of the spectrum at higher frequencies, then the low and high frequency length scales will appear similar. As we shall observe later, the higher frequency length scales are shorter than the low frequency scales. Thus, the spectrum of the high frequency fluctuations is not determined by the unresolved very low frequency fluctuations, at least not directly.

II.3.2 Isotropic correlation functions

To draw the objective maps of the temperature, an exponential correlation function with a 100 km decay length scale is assumed. While the mapping technique is not very sensitive to the correlation function, the apparent eddy length scales decrease with depth, inconsistent with the correlation function used to draw the maps. In Figure II.10, the estimated temperature correlation functions (assumed isotropic) at 515 m in the thermocline, 1420 m in the Mediterranean water and 4000 m in the deep water are shown. The correlation estimates are averages over all mooring pairs within 25 km bins. A general feature of the correlation at all depths is the rapid decrease in correlation with increasing separation with the rate of decrease increasing with depth.

The temperature observations at each mooring are not necessarily spatially independent. If we assume, at first, that each instrument is independent and allow 3 to 4 degrees

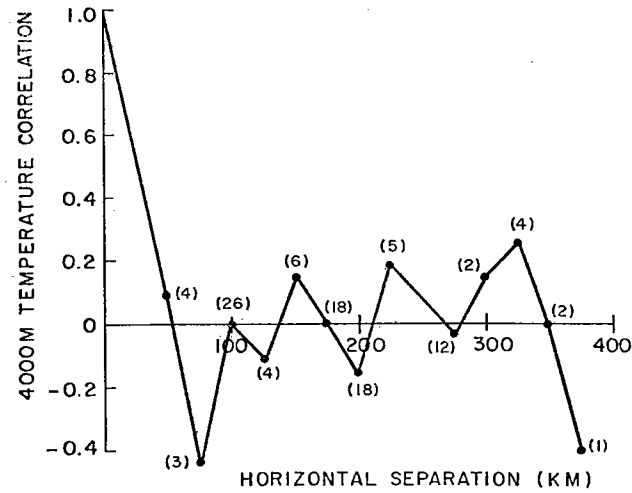
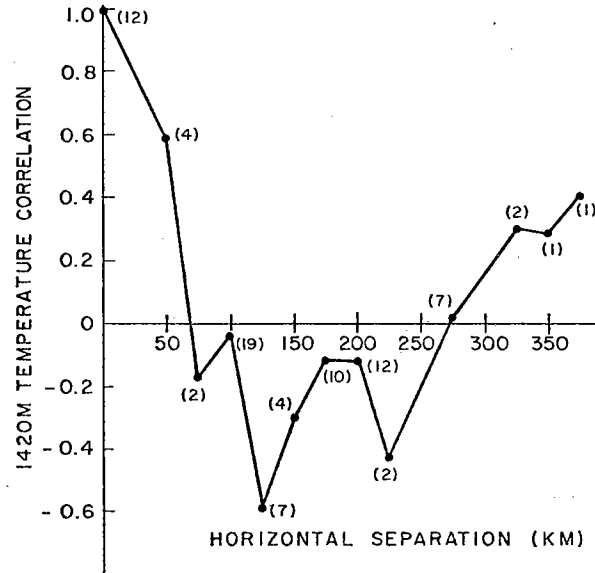
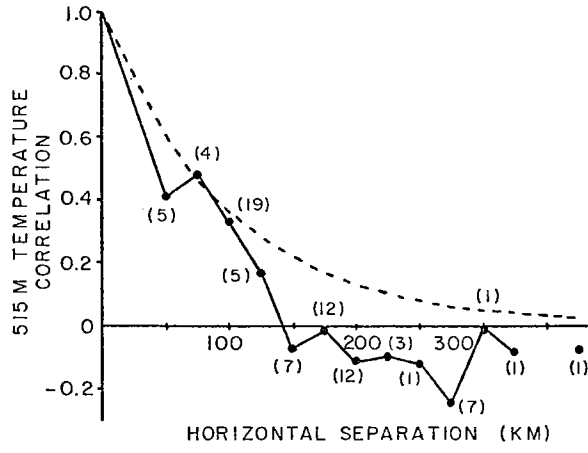


Figure II.10: Isotropic spatial temperature correlation functions

during MODE-I (dashed line is exponential with 100 km decay length)

of freedom per instrument from time averaging, then the only correlations distinguishable from zero occur at 100 km separation in the thermocline and 125 km separation in the Mediterranean water. This does not imply necessarily that the other correlations are zero, but just that we lack the data to distinguish them from zero within the large error bounds. In the deep water, the assumption that the temperature observations are independent for separations greater than 50 km seems reasonable. At the shallower depths, the observed correlations indicate a lack of independence between moorings. Using II.2.4, the separation required for independence is estimated at approximately 100 km for the thermocline and 75 km for the Mediterranean water. With this assumption the thermocline remains significantly correlated at 100 km separations and, in fact, is indistinguishable from the exponential with 100 km decay length used to draw the objective maps. However, the Mediterranean water correlation at 125 km separations is no longer significant. Thus, the independence length scale of the Mediterranean water is intermediate between the short deep water scale and the thermocline scale of 100 km.

For a temperature field with a dominant wavelength λ , the correlation function will oscillate with the first zero crossing at $\lambda/4$. It is obvious that the zero crossing will be unreliably estimated here. With the low number of degrees of freedom (N) in the observed correlation functions the zero

significance error bars will depend on N, but will be large, greater than ± 0.3 . Proceeding nevertheless, the zero crossing systematically decreases with depth from approximately 140 km at 515 m to 70 km at 1420 m and 55 km at 4000 m. The decrease in scale with increasing depth is consistent, as it must be, with the visual scale determination from the objective maps and with the dynamic height correlation functions calculated by Scarlet (1974b) from the density observations.

II.3.3 Horizontal coherence

The correlation function is a measure of the horizontal variation of the temperature over a broad frequency range. Because the power in the spectra is dominated by the low frequencies, the correlation functions will be more sensitive to the variation at low frequencies rather than higher frequencies. Another measure of the horizontal variation is the coherence with the advantage of being able to focus on a frequency range of interest. Again assuming an isotropic temperature field and averaging over 25 km bins, the coherence is estimated by

$$\text{coh} = N(s_1, s_2)^{-1} \sum_{s_1 < s \leq s_2} \frac{\phi_{ij}(\omega, s)}{\phi_i(\omega)^{1/2} \phi_j(\omega)^{1/2}} \quad (\text{II.3.2})$$

where $\phi_{ij}(\omega, s)$ is the cross spectral density of the temperature at instruments i and j separated by distance s, $\phi_i(\omega)$ is the power density at the ith instrument and $N(s_1, s_2)$

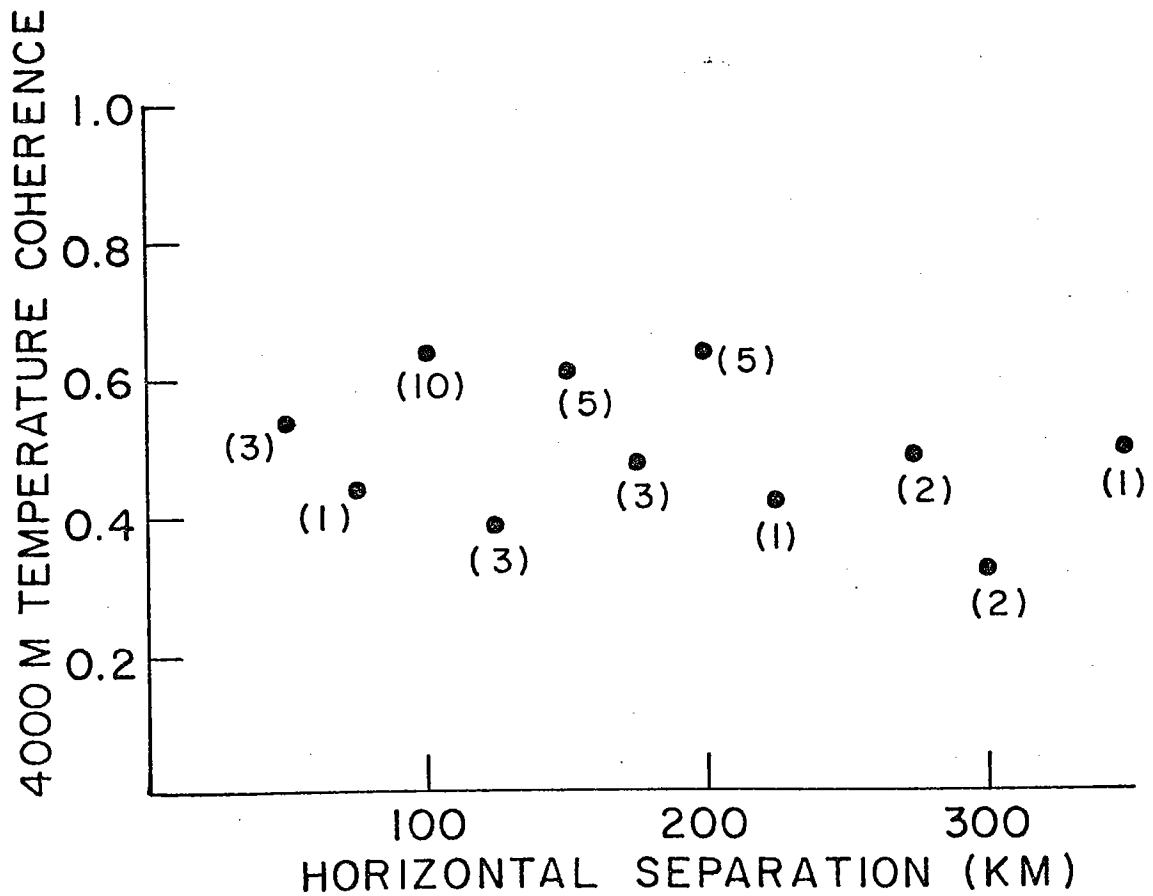
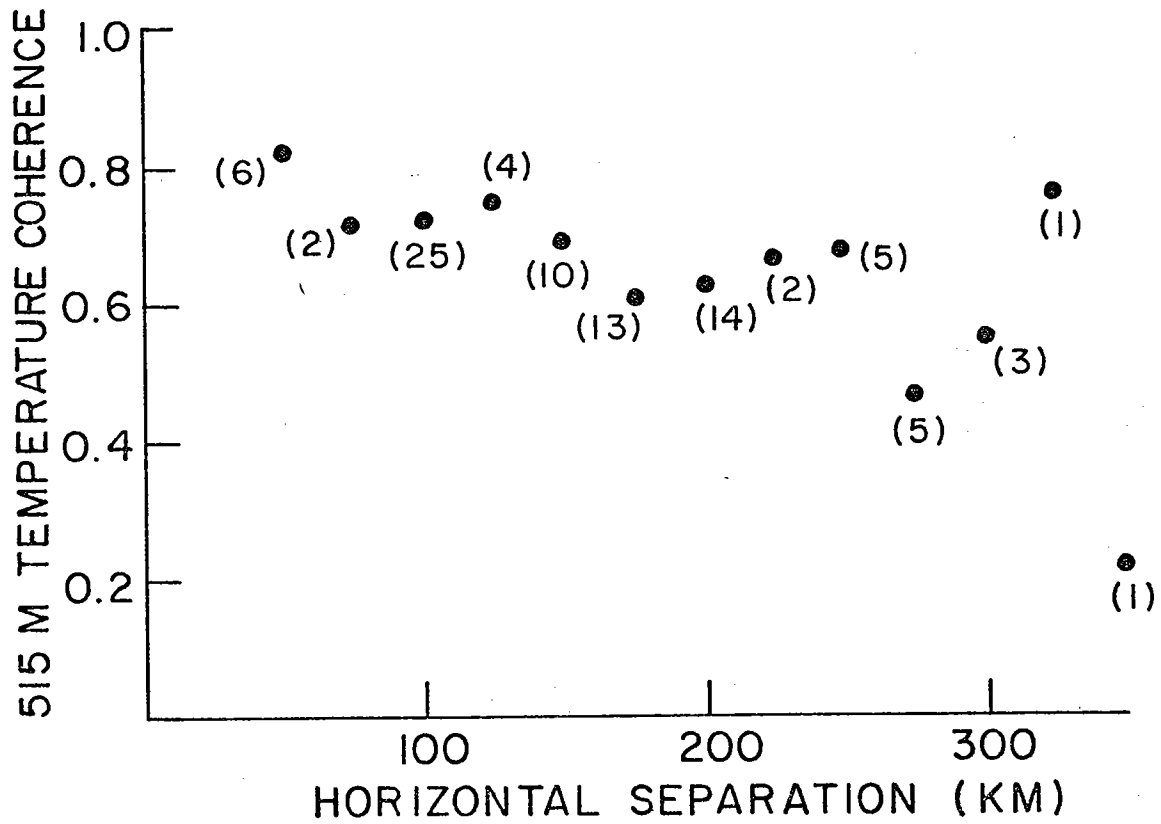


Figure II.11: Isotropic horizontal temperature coherence

is the number of instruments separated by a distance between s_1 and s_2 .

In the main thermocline, the horizontal coherence for 7 to 78 day periods, with approximately 4 degrees of freedom per instrument, decreases nearly linearly with increasing separation, falling below zero significance at 95% confidence (Amos and Koopmans, 1963) beyond separations of 325 km. At higher frequencies from 2 to 7 day periods, the coherence is insignificant even at the smallest separation of 50 km. In the deep water, the horizontal coherence from 7 to 78 days is nearly constant with separation at a level of approximately 0.5 and falls below significance at 95% confidence for separations greater than 200 km.

The horizontal coherence is a function of frequency and depth. At low frequencies, the horizontal scale in the thermocline is 50 to 70 km, while the scale at relatively higher frequencies is too small to be determined from the observations. In the deep water the coherence is lower than in the thermocline with an apparent scale of 35 km and which is associated with a shorter time scale as well (discussed in section II.3.1).

II.3.4 Wavenumber spectra

So far in this section we have considered the horizontal variation of the temperature assuming an isotropic field. The mesoscale variations of the velocity and temperature are

not necessarily isotropic as noted by Freeland, et al. (1975) and as is clear by visual inspection of the objective maps (section II.1).

The instrument array at a given level can be used as an antenna to determine the direction and wavelength of the temperature fluctuations. The conventional "beamforming" estimator of the wavenumber spectrum $p(k_x, k_y, \omega)$ is

$$p(k_x, k_y, \omega) = M^{-2} \sum_{i,j=1}^M \frac{\phi_{ij}(\omega) \exp(i\mathbf{k} \cdot (\mathbf{r}_j - \mathbf{r}_i))}{\phi_i^{1/2}(\omega) \phi_j^{1/2}(\omega)} \quad (\text{II.3.3})$$

where $\phi_{ij}(\omega)$ is the cross power density between the i th and j th sensors located at \mathbf{r}_i and \mathbf{r}_j respectively, $\phi_i(\omega)$ is the power density at the i th sensor, and M is the total number of sensors. The wavenumber spectrum is subject to a doubly periodic aliasing (c.f. Wunsch and Hendry, 1972). Since the smallest separation is 50 km, the beam pattern of the array will be repeated on the order of 0.01 cpkm. Wavenumbers greater than approximately 0.01 cpkm will not be distinguishable from smaller wavenumbers. The beamforming estimate computes the wavenumber spectrum based upon the phase differences between sensors. Thus, if the field is composed of standing waves, the beamforming estimate will yield a peak at zero wavenumber and not at the wavenumber of the standing waves. For a single wave with wavenumber \mathbf{k}_0 and amplitude a , the resultant wavenumber spectrum will be $a^2/2 |B(\mathbf{k} - \mathbf{k}_0)|^2$ where

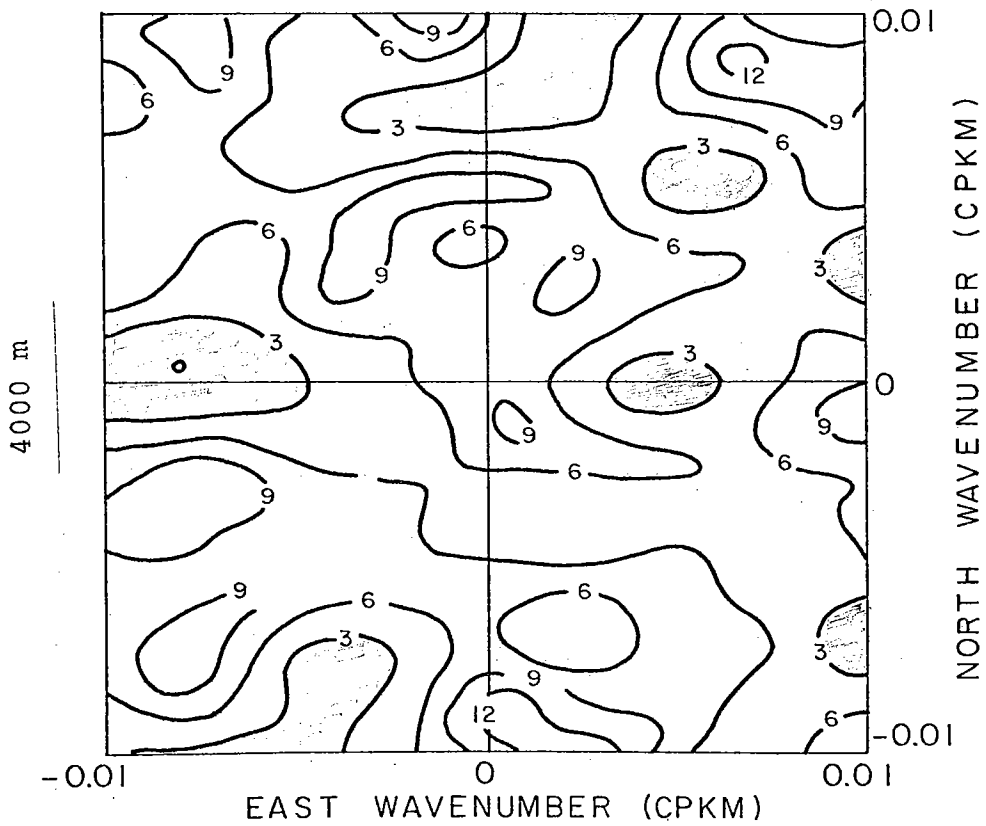
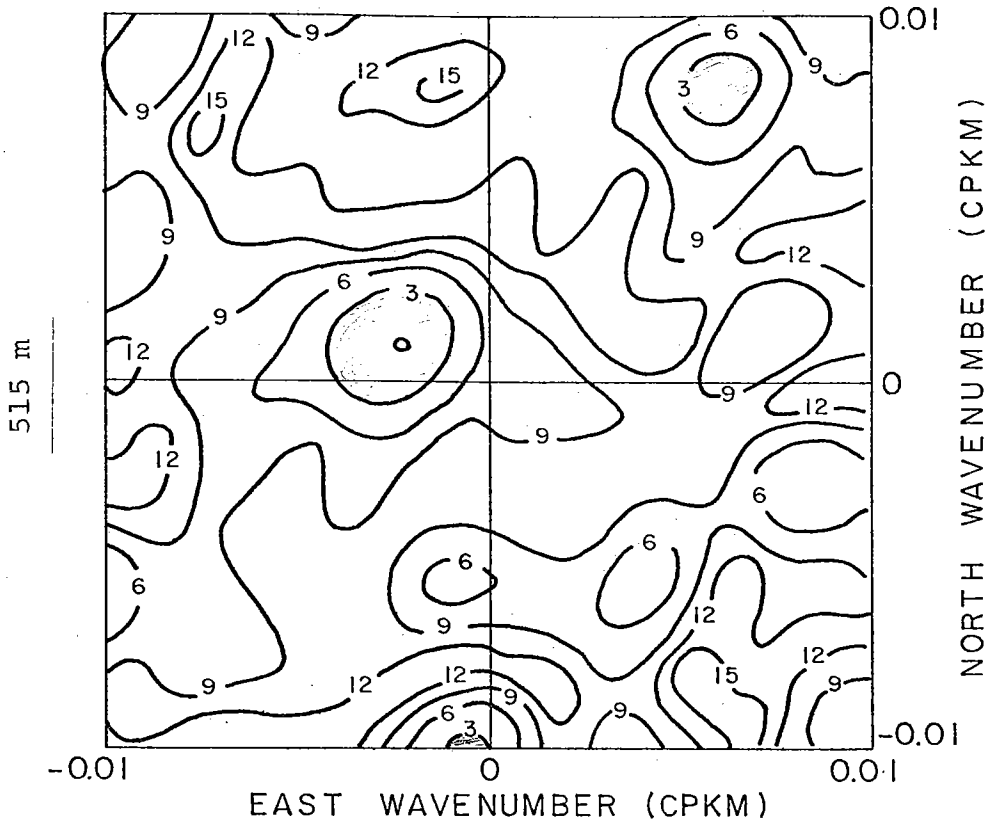


Figure II.12: Temperature horizontal wavenumber spectra during MODE-I

$$B(\underline{k}) = M^{-2} \sum_{i,j=1}^M \exp(i \underline{k} \cdot (\underline{r}_i - \underline{r}_j)) \quad (\text{II.3.4})$$

and $|B(\underline{k})|^2$ is the beam pattern of the array. In principle, the wavenumber spectrum for a field of N uncorrelated waves would be $a_i^2/2 |B(\underline{k} - \underline{k}_i)|^2$. However, if the records are not sufficiently long, the waves will be spuriously correlated over the dataset and spurious peaks of the form $\text{RE}(a_i a_j B(\underline{k} - \underline{k}_i) B^*(\underline{k} - \underline{k}_j))$ will be added to the beamforming estimate. The very low frequency temperature is not stationary over the duration of MODE-I. The shortness of MODE-I will cause spurious wavenumber information to be added to the beamforming estimate.

Keeping this in mind, the wavenumber spectrum for the thermocline is shown in Figure II.12. Contours of the spectrum are negative decibels. An increase in 3 db represents a decrease by half the power. Wavenumber spectrum estimates should be distributed as χ^2 (Capon and Goodman, 1970) with the 95% confidence limits approximately ± 3 db. In the thermocline, 60% of the power from 7 to 78 day periods lies in a peak with wavelength 370 ± 50 km. The north-south wavenumber is indistinguishable from zero at 95% confidence. The wavenumber spectrum is consistent with the objective maps showing an approximately 60 km scale eddy moving westward. During MODE-I the north-south variation appear as standing oscillations and thus no scale information can be obtained from the wavenumber spectrum.

In the deep water, the temperature variations in the objective maps appear as standing oscillations. The wavenumber spectrum at this depth will not be particularly informative, although it is shown anyway in Figure II.12. Shorter scales are more energetic in the deep water than in the thermocline.

MODE-I is too short to assess the mean isotropy of the temperature field. In the main thermocline, the dominant feature is the westward motion of a 60 km scale eddy while in the deep water the horizontal scale decreases to 35 km.

II.4 Vertical variation of temperature

From what we have already seen, the dominant horizontal length and time scales are longer in the thermocline than in the deep water. With the depth variation of the scales, it is of interest to determine the corresponding vertical scales.

II.4.1 Vertical coherence

The vertical coherence of the temperature may be estimated in two ways

$$\text{coh} = \left| \frac{\langle \hat{T}_i \hat{T}_j^* \rangle}{\langle |\hat{T}_i|^2 \rangle^{1/2} \langle |\hat{T}_j|^2 \rangle^{1/2}} \right| \quad (\text{II.4.1})$$

and

$$\text{coh} = \left| \left\langle \frac{\hat{T}_i \hat{T}_j^*}{|\hat{T}_i| |\hat{T}_j|} \right\rangle \right| \quad (\text{II.4.2})$$

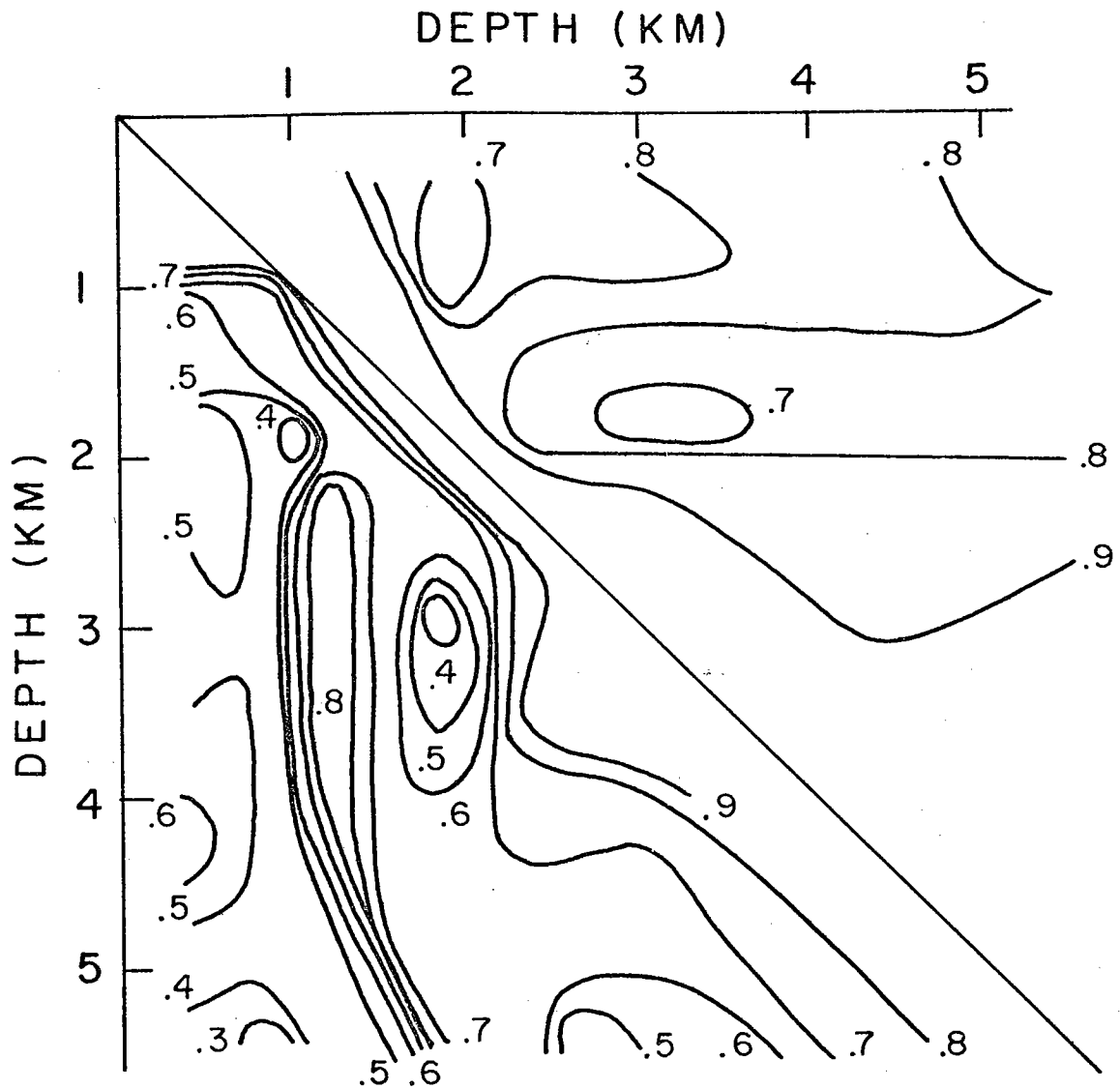


Figure II.13: Vertical coherence of temperature during MODE-I
 (upper triangle is power weighted estimate
 II.4.1 and lower triangle is broad band
 estimate II.4.2)

where \hat{T}_i is the Fourier transform at the i th instrument and $\langle \rangle$ denotes averaging over frequency bands. For gaussian white noise both estimators would yield the same result with the 95% confidence limit for zero coherence with 10 degrees of freedom at 0.48 (Amos and Koopmans, 1963). However, for a red spectrum the first estimator (II.4.1), which weights the contribution of each frequency band by the power in the band, will be dominated by the lowest band. The number of degrees of freedom is reduced and consequently one expects a higher coherence. When the proper number of degrees of freedom is determined, both estimators yield a consistent description of the coherence.

As an example, the vertical coherence of the temperature at the heavily instrumented central mooring during MODE-I is shown in Figure II.13 for 22 to 112 day periods. Visual inspection of the temperature records at mooring 481 (Figure I.2) suggest that the thermocline and deep water are coherent with a loss of coherence in the Mediterranean water and very near the ocean bottom. Allowing for the reduced number of degrees of freedom in the power weighted estimate, both estimators give high coherence with insignificant phase differences in the thermocline and deep water. Coherence between the thermocline and deep water drops, but is significantly nonzero at 95%. The coherence is lowest in the Mediterranean water, where temperature variations are not always associated with density changes, and very near the

bottom, where a bottom mixed layer is present (Armi and Millard, 1976 and Richman and Millard, 1976).

At higher frequencies, for 7 to 22 day periods, the only significant coherence at 95% occurs within the main thermocline. Thus, the thermocline is coherent over a wide frequency range. The vertical scale of the very low frequencies is of the order of the ocean depth, while at higher frequencies, corresponding approximately to the band where the temperature scales with the WKB approximation, the scale decreases to 500 m or less. Later in section III.2, we shall discuss the vertical coherence for longer records at the site moorings.

II.4.2 Empirical vertical structure

Because the vertical scale of the very low frequency motions is comparable to the ocean depth, a plausible way to describe the variation of the temperature is by expansion in a set of functions spanning the ocean in the vertical. The choice of basis functions is in general arbitrary. However, the physical interpretation is aided by an appropriate choice. One possible set of basis functions is the linear quasigeostrophic wave modes (c.f. section IV.1). Later, in section V.1, we shall consider wave models of the MODE data. Here, we shall use the technique of empirical orthogonal functions to find a set of basis functions that describe the most energy in the variations.

Empirical orthogonal functions

Suppose we consider the daily averaged temperature or velocity as an ensemble of sample random functions $T(z_i; t_j)$ defined at the depth levels z_i , we want to find the function $\phi(z_i)$ that best resembles the sample functions statistically. Using the technique of empirical orthogonal expansion introduced by Kosambi (1943) and discussed by Obukhov (1960) and Busch and Petersen (1971), we can express the sample functions in terms of a set of orthogonal functions $\phi_n(z_i)$

$$T(z_i; t_j) = \sum_n a_n(t_j) \phi_n(z_i) \quad (\text{II.4.3})$$

where the expansion coefficients $a_n(t_j)$ are uncorrelated and $\phi_n(z_i)$ maximize the correlation with the sample functions. Busch and Petersen (1971) have shown for a discretely sampled scalar process that the empirical modes are the solution to the vector equation at N depth levels

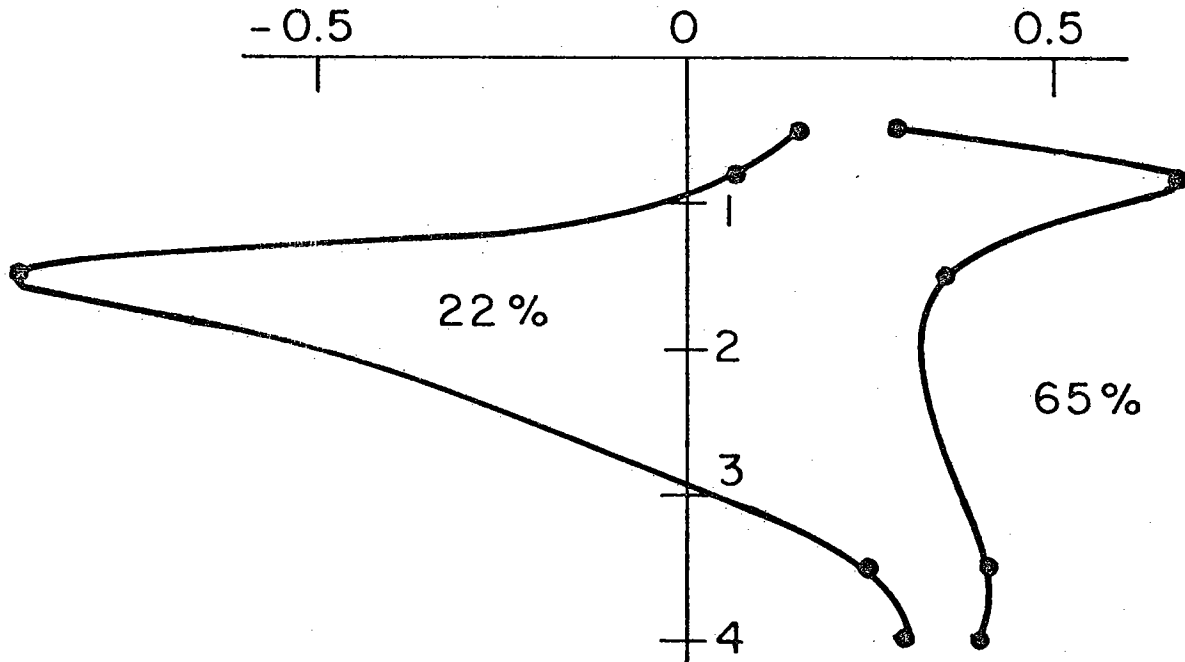
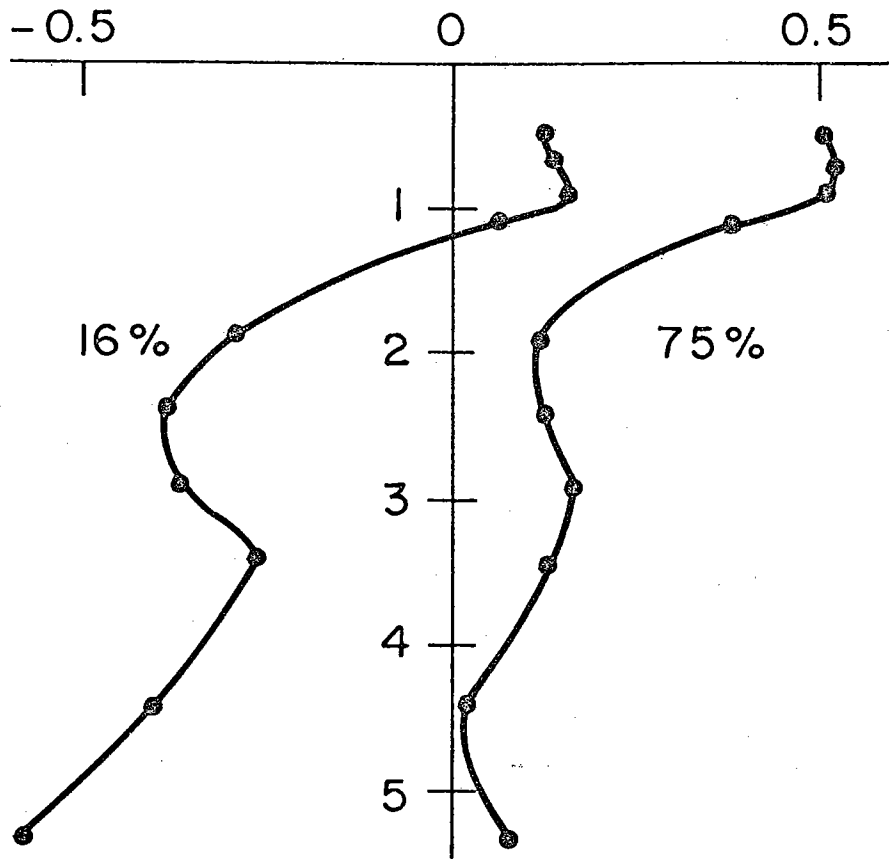
$$\sum_{i=1}^n R(z_i, z_j) \phi_n(z_i) = \lambda_n \phi_n(z_j) \quad (\text{II.4.4})$$

where $R(z_i, z_j)$ is the covariance of the process at the depths z_i and z_j obtained by ensemble averaging over the M realizations

$$R(z_i, z_j) = M^{-1} \sum_{k=1}^M T(z_i; t_k) T(z_j; t_k) \quad (\text{II.4.5})$$

Figure II.14: Empirical displacement modes and percentage of the total potential energy in each mode at mooring 1 (upper plots) and at MODE Center (lower plots)

EMPIRICAL DISPLACEMENT MODES



The eigenvalue λ_n is the amount of energy in the process described by the eigenvector ϕ_n and is given by the expected value of the nth expansion coefficient

$$\lambda_n = \langle a_n^2(t_j) \rangle \quad (\text{II.4.6})$$

Since the covariance matrix R is real and symmetric, the eigenvalues λ_n are real and nonnegative and the eigenvectors are real and orthogonal.

Displacement empirical modes

The central mooring (481) during MODE-I was instrumented to measure temperature at 12 depths, allowing the greatest resolution of the vertical structure. Using the empirical expansion, 91% of the displacement variance is described by two modes with 75% in the lowest mode. For the first empirical mode, the maximum displacement is at 800 m with secondary maxima at 3000 m and near the bottom. The mode is in phase at all depths, while for the second mode the thermocline displacement is small and out of phase with the deep water. Because the covariance matrix is used to generate the empirical modes, they represent the vertical structure of the very low frequencies. Less energetic high frequency motions with small vertical scales will not be described by the empirical modes. A two mode structure, one dominant in the thermocline and the other dominant in the deep water,

describes the observed vertical coherence with a coherent thermocline and deep water and a loss of coherence between the thermocline and deep water. At least two modes are required to yield different length and time scales in the thermocline and deep water.

Is the vertical structure of MODE-I typical of the mesoscale displacement field? Using 300 days of data at MODE Center, the empirical modes for a longer time series are shown in Figure II.14. Three modes describe 97% of the variance with the first mode having maximum displacement in the thermocline and in phase variations with depth and the third mode having equal but out of phase displacements in the thermocline and deep water. The second mode has a maximum displacement in the Mediterranean similar to the weak third mode during MODE-I (not shown). Thus, the displacement field in the MODE region may be described in general by a dominant mode with maximum thermocline displacement and a weaker mode with out of phase thermocline and deep water displacements.

II.4.3 Velocity vertical structure

So far we have considered only the vertical structure of the temperature field. Current meter data return during MODE-I is too small to make direct comparisons between the velocity and temperature fields. However, Davis (1975)

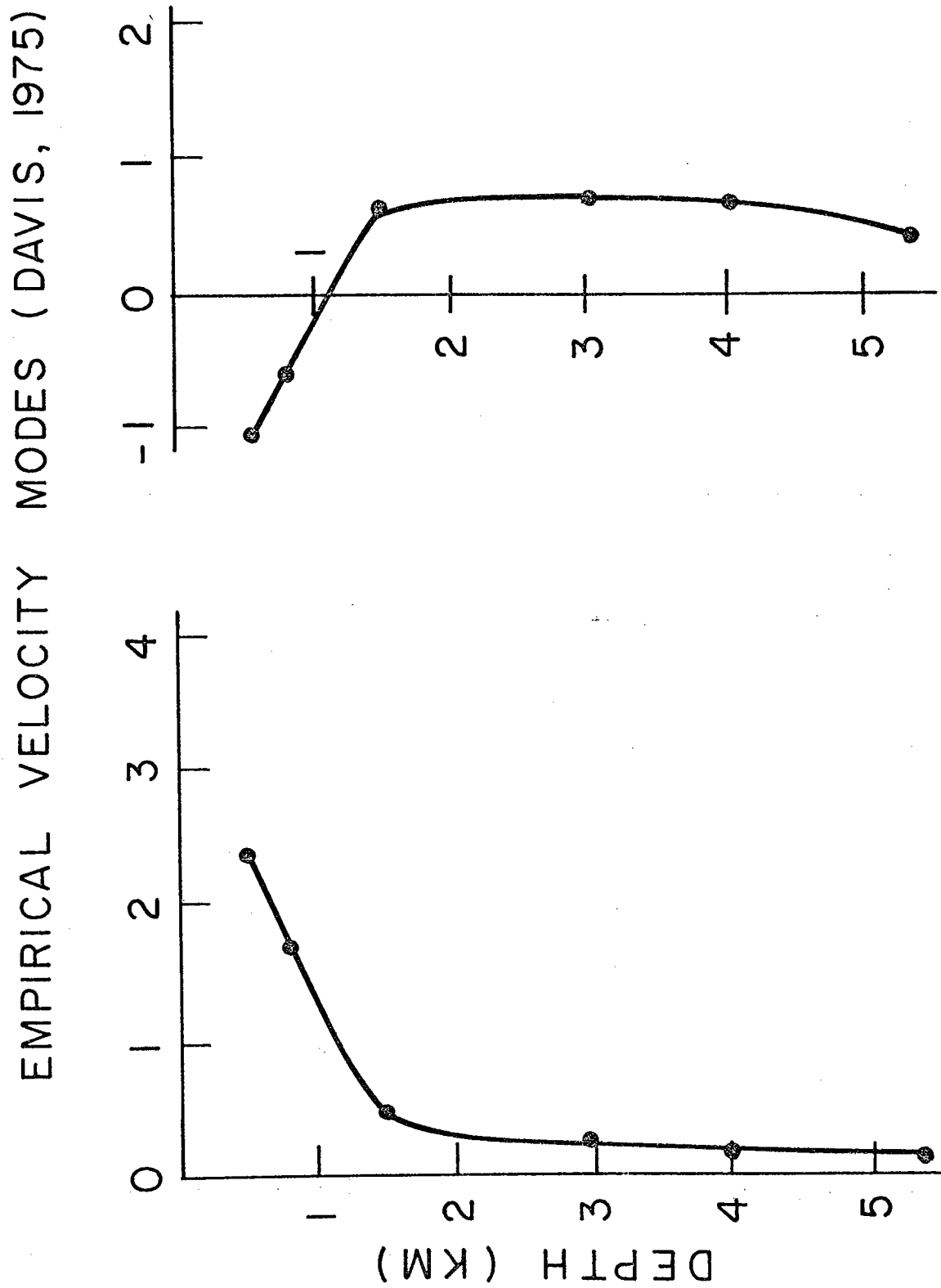


Figure II.15: Isotropic empirical velocity modes (after Davis, 1975)

has computed the velocity empirical modes assuming an isotropic field during MODE-0 and MODE-I, shown in Figure II.15. The first mode with 70% of the kinetic energy has a maximum near the surface and in phase currents, while the second mode with 22% of the kinetic energy has out of phase currents between the thermocline and deep water. A two mode description of the velocity field is consistent with the streamfunction objective maps of Freeland and Gould (1976) showing a large slowly moving feature in the thermocline and small rapidly moving features in the deep water with little correlation between the two.

During MODE-I, detailed vertical profiles of the velocity field were obtained by Pochapsky (1976) and Sanford (1975) using acoustic and electromagnetic dropsondes, respectively. The visual similarity between the empirical modes and the mean meridional velocity profile is high, both having a near surface maxima. Because the electromagnetic dropsonde measures only the baroclinic component of the flow, comparisons can be made only with the current shear. The vertical shear of the zonal flow is less than the meridional and is not well represented by the empirical modes. Later, we shall consider differences between the zonal and meridional components of the flow and possible dynamical implications of this anisotropy.

Dropsonde profiles during MODE-I near the central mooring are consistent with a low mode, large vertical scale

description of the velocity field. However, significant deviations from this simple picture of the vertical structure can occur. Using an electromagnetic dropsonde Hogg (1976) observed a decrease in the vertical shear near an abyssal seamount, indicating that at least in some regions topography can interact strongly with the mesoscale flow.

II.5 Kinetic and potential energy in the MODE region

During MODE-I, the main thermocline is dominated by a 50 to 70 km scale eddy moving westward, while the deep water is dominated by shorter length and time scales. Is the MODE-I eddy at all typical of the spatial and temporal variation in the region? Using the longer but spatially limited site mooring records, we can begin to answer such a question. In this section we shall consider overall variations in the kinetic and potential energy between the site moorings. Later, in Chapter III, we shall use the spectra for a detailed description of the variability.

II.5.1 Mean flow

Before we discuss the eddy energy levels at the site moorings we shall consider briefly the mean flow in the MODE region. Later, when considering possible dynamical mechanisms for the mesoscale flow, it will be useful to know that the mean flow is small except in the deep water over the abyssal topography.

In the main thermocline, the time averaged flow at

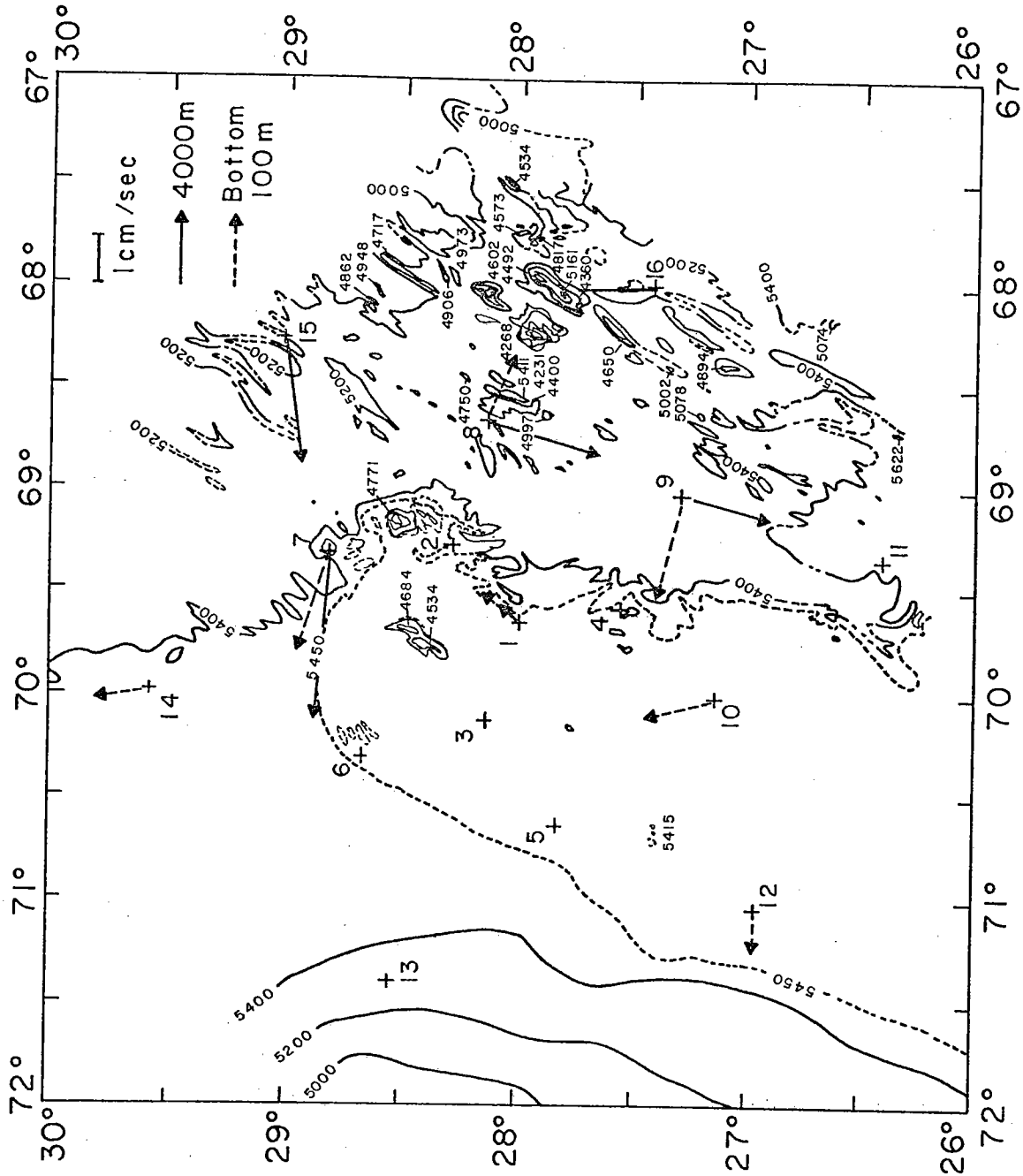


Figure II.16: Mean flow in deep water in MODE region

both site moorings is approximately 2 cm/sec in an easterly direction, but not significantly different from zero. The mesoscale motions are vigorous in the thermocline with significant contributions to the kinetic energy at very low frequencies. Thus, we require large amounts of data to distinguish a mean flow from the dominant mesoscale flow. McWilliams (1974), using historical density data to estimate geostrophic shears, found no significant density differences in the main thermocline over 1000 km in the MODE region, indicating little mean flow below 400 m.

In the Mediterranean water, the average flow at both site moorings is to the southwest, but is not significantly different from zero in magnitude. Freeland, et al. (1975) using SOFAR float trajectories estimated a significantly nonzero pseudo-Lagrangian mean flow of 0.9 cm/sec to the west. For small but finite amplitude waves, the difference between the Eulerian and true Lagrangian mean flow is the Stokes drift, of order $\overline{u'^2} T/L$, where $\overline{u'^2}$ is the fluctuation variance, T the dominant time scale, and L the dominant length scale (Longuet-Higgins, 1969). For the MODE region the Stokes drift thus would be of order 1 cm/sec, indicating that the float and moored mean flow estimates are not inconsistent.

In the deep water, there is a significant southwesterly mean flow at MODE East (Schmitz, et al., 1976), but no significant flow at MODE Center. Historically from water

mass analysis and bottom photographs, the mean flow in the MODE region is a weak northward flow of Antarctic Bottom Water and southward flow of North Atlantic Deep Water above the bottom and in the western boundary undercurrent along the Outer Rise (Hollister and Heezen, 1972). All of the bottom current meters during MODE-I over the abyssal plain have at least a weak northerly component, although this is probably fortuitous. The results for the bottom current meter at mooring 8 are questionable since the vane was stuck much of the time. The mean flow at 4000 m over the abyssal hills is confused. The northern meters during MODE-I have an easterly flow and the southern meters are directed north-south. However, the observed pattern does suggest some topographic control of the deep flow.

II.5.2 Kinetic energy

The kinetic energy in the low frequency fluctuations is much greater than the mean kinetic energy even in the deep water where a nonzero mean flow is observed. Using the site mooring data, we can consider the variation of the kinetic energy between velocity components at a given location and between moorings.

In the thermocline, the zonal kinetic energy exceeds the meridional kinetic energy at both moorings by approximately a factor of 1.6, while the total kinetic energy levels are not significantly different between the moorings. When we discuss

Depth	\bar{u}	\bar{v}	$\overline{u^2}$	$\overline{v^2}$	$\overline{T^2}$	$\overline{u'v'}$	\int_{rms}
500 m	MODE	-1.1	49.3	29.6	0.27	-2.7	34.4
	Center	+2.6	+15.5	+3.6	+0.07	+4.8	
1500 m	MODE	0.3	39.7	26.3	0.19	-3.1	28.5
	Center	+2.4	+14.7	+4.5	+0.08	+5.1	
4000 m	MODE	-0.5	7.2	7.6	5.9×10^{-3}	2.3	32.5
	Center	+0.8	+1.1	+1.3	$+0.6 \times 10^{-3}$	+1.6	
4000 m	MODE	-0.2	3.3	2.8	1.1×10^{-2}	1.3	44.8
	Center	+0.6	+0.5	+0.5	$+0.5 \times 10^{-2}$	+1.0	
4000 m	MODE	0.3	7.5	9.7	8.6×10^{-5}	3.7	39.9
	Center	+0.3	+1.3	+1.6	$+2.8 \times 10^{-5}$	+3.0	
4000 m	MODE	-0.7	4.2	10.5	4.1×10^{-5}	2.6	27.7
	Center	+0.3	+0.5	+1.7	$+1.7 \times 10^{-5}$	+1.5	

Table II.2a: Time average mean zonal (\bar{u}) and meridional (\bar{v}) flow, velocity and temperature variance, and Reynolds stress ($\overline{u'v'}$) for the two site moorings, MODE Center (28°N, 69°40'W) and MODE East (28°10'N, 68°40'W)

the velocity spectra in section III.2, we shall find that the zonal kinetic energy is dominated by very low frequencies. This result is consistent with the long zonal correlation time found in section II.2.1.

In the Mediterranean water at 1500 m, the zonal and meridional kinetic energy are nearly equal. However, the total kinetic energy decreases by at least a factor of 2 between MODE Center and MODE East. This eastward decrease was noticed by Freeland, et al. (1975) from the SOFAR floats and by Schmitz, et al. (1976) in the site mooring data. Possible reasons for this decrease in kinetic energy over a distance comparable to the eddy scale will be discussed later.

In the deep water, the meridional kinetic energy exceeds the zonal at both moorings, although the difference (a factor of 2.5) is significant only at MODE East. The total kinetic energy is nearly the same at both moorings. For quasigeostrophic dynamics, the effect of topography is to polarize the flow along contours of f/h . The principal axis of the flow at MODE East is oriented approximately along the axis of Swallow Knoll, again suggesting possible topographic control of the deep flow at this mooring.

The kinetic energy is greatest in the thermocline, decreasing in the Mediterranean water and then increasing in the deep water. With the eastward decrease in kinetic energy in the Mediterranean water, the vertical shear is greater at MODE East than at MODE Center. One possible

Depth		Kinetic Energy (ergs/gm)	Potential Energy (ergs/gm)
500 m	MODE Center	39.4	59.6
	MODE East	33.0	40.9
1500 m	MODE Center	7.4	8.2
	MODE East	3.0	15.7
4000 m	MODE Center	8.6	1.8
	MODE East	7.3	0.9

Table II.2b: Kinetic and potential energy levels
at the two site moorings

way to describe the variation of the velocity vertical structure between the moorings is to decompose the kinetic energy into barotropic and baroclinic components. Using the linear quasigeostrophic normal modes calculated in section IV.1.1 and assuming independent barotropic and baroclinic motions, the barotropic energies are 6.6 and 4.0 ergs/gm at MODE Center and MODE East respectively and the baroclinic energies are 6.9 and 6.1 ergs/gm respectively. Thus, with this simple model, the eastward decrease in kinetic energy is associated with a loss of barotropic kinetic energy and shows up in the Mediterranean water only because the first baroclinic mode has a minimum at that level.

II.5.3 Potential energy

A potential energy for the low frequency flow may be estimated from the temperature variance using equation II.3.1. The temperature records at MODE East are too short to allow meaningful comparisons of the potential energy levels with MODE Center. In general, no significant differences are observed between the moorings. At MODE Center, the kinetic and potential energy are equal at 90% confidence in the main thermocline and Mediterranean water, while in the deep water the kinetic energy is greater than the potential energy. Thus, while the horizontal variation of the potential energy is apparently consistent with the energy model of the previous section, the vertical distribution of potential energy is

not. Relative to the Mediterranean water, the potential energy in the thermocline is greater than expected from a linear first baroclinic mode but not significantly so, while the deep water is greater than expected for a first mode by a factor of 5.

During MODE-I, the spatially averaged temperature variance in the Mediterranean water and deep water is not significantly different from the site mooring variance. However, in the thermocline, the spatially averaged variance is only a third of the site mooring variance. Thus, the potential energy is underestimated in the thermocline during MODE-I, while the apparently shorter length and time scales in the deep water allow a reasonably stable estimate of the potential energy to be obtained there.

II.5.4 Reynolds stresses and heat flux

The zonal and meridional eddy kinetic energy, discussed earlier, are the diagonal terms of the Reynolds stress tensor. In the Mediterranean water and deep water, the off-diagonal Reynolds stress, $\overline{u'v'}$, is significantly different from zero at both site moorings (Table II.2a). At both depths, the momentum flux is greater at MODE Center than at MODE East, although the difference is not significant at 90% confidence. Similarly, the total eddy kinetic energy at these depths decreases to the east, but the difference is significant only in the Mediterranean water. A negative east-west

Depth	$\overline{u'T'}$ (°C cm/sec)	$\overline{v'T'}$ (°C cm/sec)
500 m	0.79	8.9×10^{-2}
1500 m	8.6×10^{-2}	8.4×10^{-2}
4000 m	1.6×10^{-2}	-5.8×10^{-4}

Table II.3a: Velocity-temperature covariance at MODE Center

Depth	Heat Transport	
	Zonal (ergs/sec/cm ²)	Meridional (ergs/sec/cm ²)
500 m	3.3×10^7	3.7×10^6
1500 m	3.6×10^6	3.5×10^6
4000 m	6.7×10^5	-2.4×10^3

Table II.3b: Heat transport at MODE Center

Reynolds stress gradient indicates a convergence of southerly mean momentum. Thus, the eddies may transport momentum to the western boundary undercurrent to the east of the MODE region. Schmitz (1976) has suggested from the large scale variation of the Reynolds stresses that the eddies may be driving the deep mean circulation. We refer the reader to Schmitz (1976) for further discussion of the eddy Reynolds stresses in the western North Atlantic.

The eddies may transport heat as well as momentum. In the deep water at MODE Center, a significantly nonzero zonal heat flux is observed. This is the only velocity-temperature covariance which is distinguishable from zero at 95% confidence. To assess the importance of the eddy heat transport in the thermal balance of the ocean, we shall compare the observed heat flux with the estimated poleward heat flux carried by the ocean annually. Vonder Haar and Oort (1973) estimate the poleward oceanic heat transport of the northern hemisphere oceans at approximately 10^{22} ergs/sec. Assuming an average oceanic depth of 4 km, the average heat flux would be approximately 10^8 ergs/sec/cm². The observed eddy zonal heat flux is two orders of magnitude less than the average annual poleward heat flux. Even in the thermocline, the observed values are an upper bound, and thus are only the same order of magnitude as the poleward heat flux at a maximum. Thus, while the eddy heat transport is potentially important to the oceanic thermal balance, the observed heat

flux in the MODE region is small.

II.6 Summary and discussion

From the objective maps of the temperature during MODE-I, we observed that the main thermocline is dominated by a warm core eddy with 50 to 70 km length scale and approximately 16 day time scale moving westward at 2 km/day. Below the main thermocline a quasipermanent trough structure with amplitude twice the magnitude of the rms fluctuations appears in the temperature field. In the Mediterranean water the eddy length and time scales appear slightly smaller than in the thermocline, but the phase speed of the eddies is nearly the same, approximately 2 km/day. However, in the deep water, no phase propagation is found. The temperature fluctuations appear as standing warm and cold pools superimposed on a larger scale quasipermanent spatial variation. During MODE-I length and time scales of the temperature fluctuations decrease with increasing depth. Coherence between the thermocline and deep water displacements is low. To describe most of the potential energy in the mesoscale eddy field requires at least two modes, one with maximum displacement in the thermocline varying in time and space like the main thermocline eddy and the other with out of phase thermocline and deep water displacements varying with the deep water length and time scales.

A single eddy is not necessarily typical of the

mesoscale variability. With the site mooring data, we can consider what may be representative of the variability in the MODE region. If we use the correlation time from the square sum of the autocorrelation as a time scale, then we find that the time scale of the site moorings does decrease with depth for temperature but not for velocity. At least two modes are required to describe the vertical structure of the temperature. However, from the site moorings, we find two results not observed during MODE-I. In the Mediterranean water, the kinetic energy decreases eastward by a factor of 2 over 100 km and in the deep water there is a net zonal heat flux. Because the dominant time scales are comparable to the duration of MODE-I, the low frequency variability is not well resolved in time. In the next chapter using the site mooring records, we shall look at the frequency distribution of potential and kinetic energy.

III. Temporal Variability

From the spatially averaged temperature spectra, we observed that for periods less than 30 days the potential energy decreases with increasing frequency as $\omega^{-2.5}$ and scales with depth in the WKB sense. The small time scale fluctuations are associated with small horizontal and vertical length scales suggesting a turbulent rather than wavelike regime for these motions. In general both the kinetic and potential energy for periods less than 30 days scale with frequency as $\omega^{-2.5}$ and with depth in the WKB sense. We shall use the similarity of the high frequency spectra to break our discussion of the temporal variability into two parts, the very low frequencies with periods greater than 30 days containing the dominant energetic mesoscale motions and the high frequencies (small scale fluctuations with periods less than 30 days but greater than 10 days).

III.1 Spectral estimation

The expected time scale of the temperature in the thermocline is 15 days and greater (periods greater than 80 days). The site mooring data lengths for velocity and temperature are 2 years or less. With the averaging required for statistical stability, conventional spectral techniques give a very limited frequency resolution. Thus, to investigate the very low frequency behavior of the fields we also shall compute high resolution maximum entropy

spectra (Lacoss, 1971). If the conventional spectral estimator is denoted by

$$P_c = n^{-2} E^T R E^* \quad (\text{III.1.1})$$

where R is the $n \times n$ covariance matrix of the data, E is a complex column vector of elements $\exp(i \lambda (j-1))$ with $j=1, \dots, n$ and λ is the smallest resolvable frequency, the superscript T indicates transpose and $*$ indicates complex conjugation, then the maximum entropy spectral estimator is denoted by

$$P_m = \frac{p \Delta t}{E^T \Gamma^* \Gamma^T E^*} \quad (\text{III.1.2})$$

where

$$R \Gamma = P \quad (\text{III.1.3})$$

with Γ the column vector $(1, \gamma_1, \dots, \gamma_{n-1})$ and P the column vector $(p, 0, \dots, 0)$. Γ is a least squares predictive error filter giving the error in estimating the current value of the data from the previous $n-1$ samples. A brief discussion of the maximum entropy spectral estimator is given in Appendix B.

In the maximum entropy spectra plots, the peak heights do not have a simple meaning, but instead the power under an observed peak is related to the power in a given frequency band (Lacoss, 1971). For example, if the covariance of a process is $\delta_{n0} + \alpha \cos \lambda n \Delta t$ where δ_{n0} is the kronecker delta and $\alpha \ll 1$ and $n \gg 1$, then the peak height of the conventional estimate is $\alpha/2$ while the

maximum entropy peak height is $\propto n^2 \Delta t/4$. The bandwidth of the maximum entropy peak is $\propto n^2 \Delta t/4$. Thus, the power under the maximum entropy peak is proportional to $\propto \lambda$, the true power at frequency λ .

The maximum entropy estimator is especially useful for determining peaks in the spectrum. If the time series has a periodicity, the maximum entropy spectrum will contain a narrow peak, while this periodicity may not be resolvable in the conventional spectrum with the low number of degrees of freedom available from the site mooring data. In the following discussions, we shall use the maximum entropy spectrum to indicate the dominant time scales of the motion and the conventional spectrum for the spectral shape and energy level.

III.2 Very low frequency fluctuations

During MODE-I some of the observed features of the very low frequency flow are: the apparently shorter time and length scales in the deep water than in the thermocline and the anisotropy of the velocity profiles. However, due to the shortness of MODE-I, the question of whether these features are typical of the region remains. Using the longer site mooring velocity and temperature measurements at three depths, 500 m in the thermocline, 1500 m in the Mediterranean water and 4000 m in the deep water, we can consider the above question of typicality and also begin to resolve the frequency dependence of the spatial variability.

In particular, we shall show the existence of at least two very low frequency regimes, an eddy energy containing band of approximately 80 to 120 day periods to which the MODE-I thermocline eddy apparently belongs and very low frequencies, periods greater than 200 days, where the flow is anisotropic with greater zonal kinetic energy than meridional.

Thermocline

The total kinetic energy in the thermocline increases with decreasing frequency out to periods of approximately one year (maximum entropy spectra in Figure III.1 and conventional spectra in Figure III.2). At very low frequencies, periods greater than 200 days, the zonal kinetic energy exceeds the meridional and dominates the total kinetic energy, while at higher frequencies, the kinetic energy is partitioned evenly between the zonal and meridional components. This very low frequency dominance of the zonal kinetic energy leads to a longer time scale for the zonal flow than for the meridional, approximately 60 and 16 days respectively, which is consistent with the long correlation time of the zonal flow compared to the meridional flow (Table II.1). The greatest contribution to the meridional kinetic energy is from the band of approximately 80 to 120 day periods. Peaks in the maximum entropy spectra of the meridional kinetic energy at MODE Center and the temperature at both site moorings are observed in this band. Velocity data returned at MODE East is inadequate

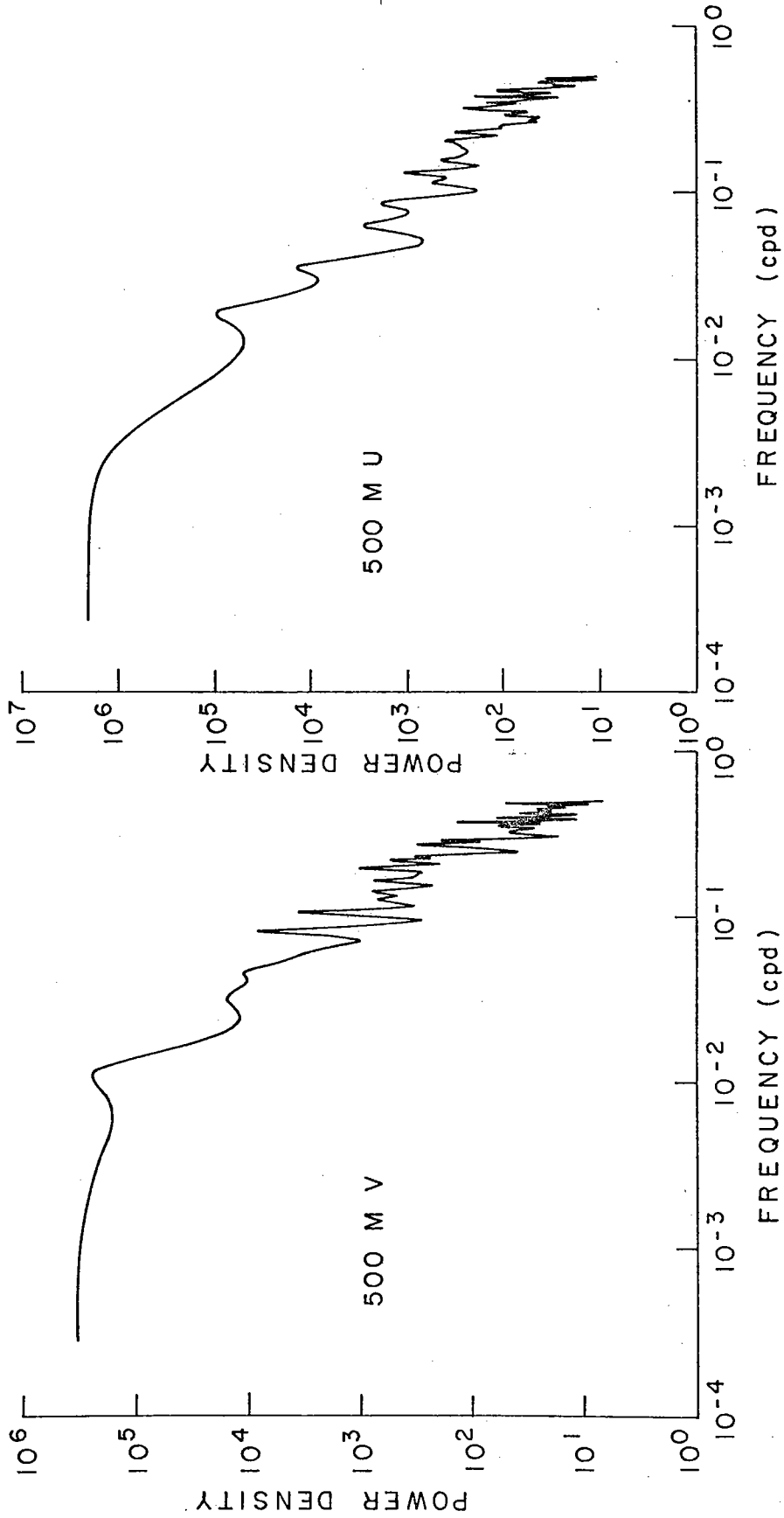


Figure III.1a: Maximum entropy spectra of main thermocline velocity at MODE Center (U--east component, V--north component)

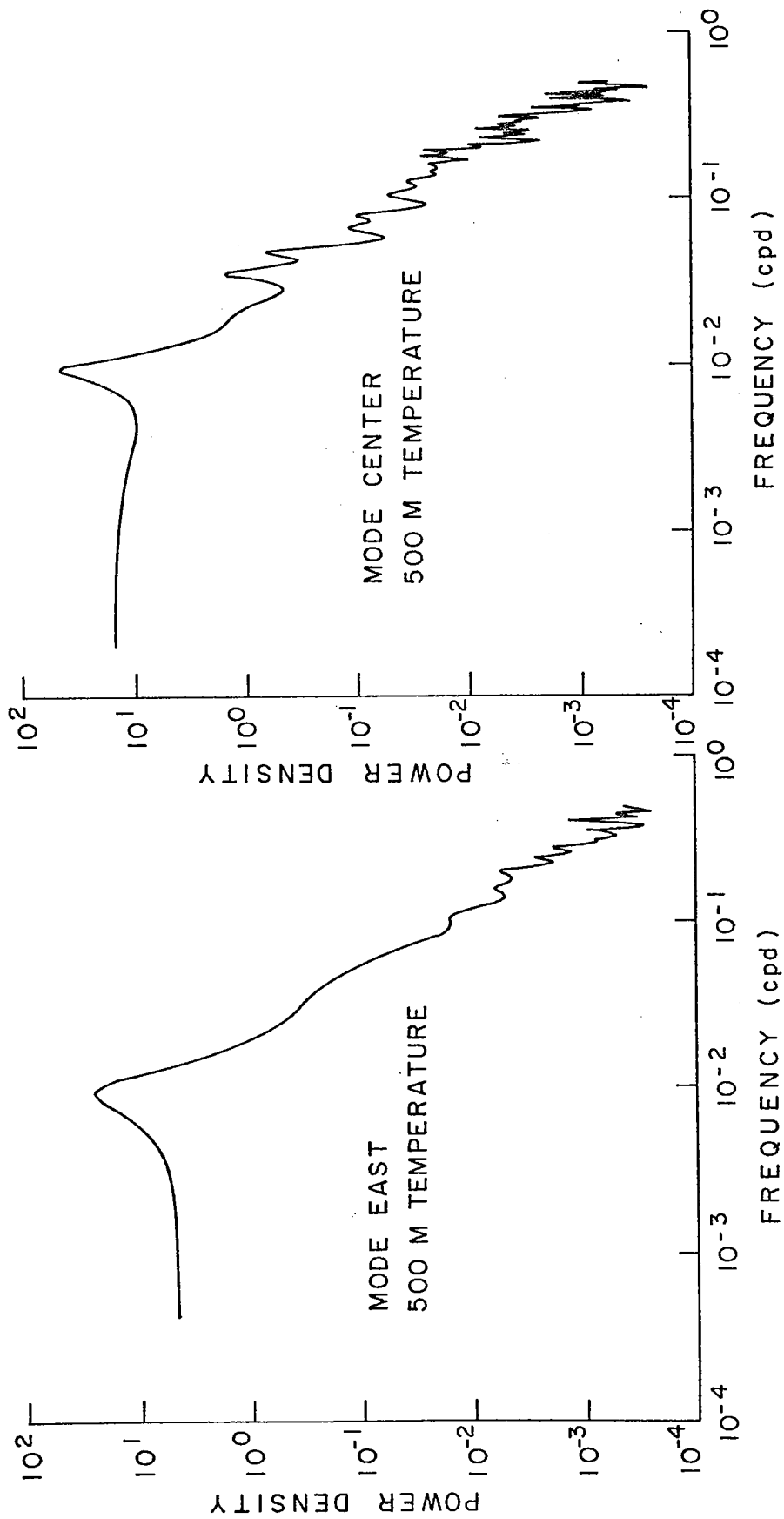


Figure III.1b: Maximum entropy spectra of main thermocline temperature

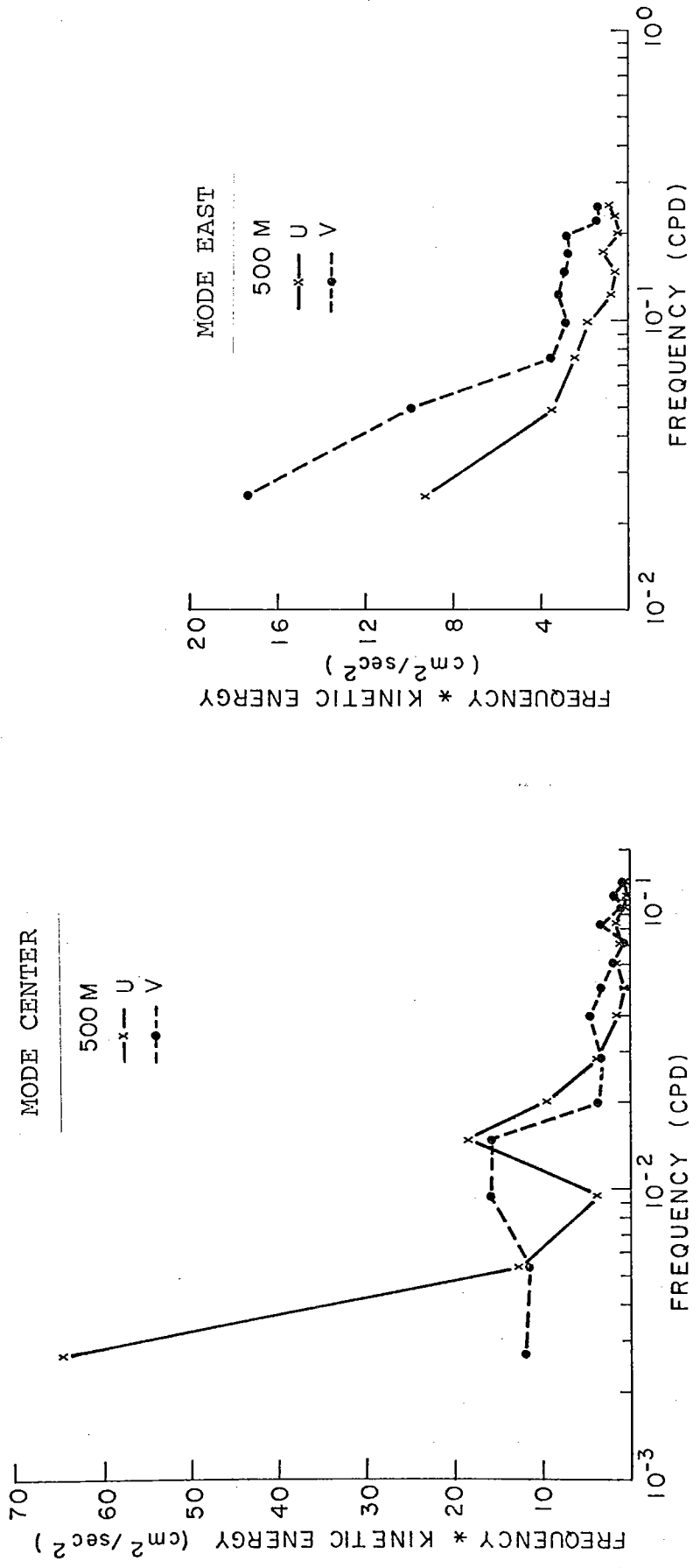


Figure II.2: Zonal and meridional kinetic energy in the main thermocline at MODE Center and MODE East

to discuss the very low frequency fluctuations there.

The dominant time scale for the temperature and meridional flow lies between the purely advective time scale and linear wave periods. A purely advective time scale L_p/U , where U is the rms velocity and L_p the internal radius of deformation, is approximately 10 days, shorter than the observed time scale, while the minimum period for a linear first mode baroclinic Rossby wave is 156 days, greater than the observed period. Thus, the main thermocline thermal balance evidently must include both propagation and advection. Later, in section V.3, we shall estimate the magnitude of both terms in the thermal balance.

Mediterranean water

In the Mediterranean water, the zonal kinetic energy exceeds the meridional at very low frequencies, periods greater than 200 days, although the difference is not significant at 90% confidence. Unlike the thermocline, the total kinetic energy is not dominated by the very low frequency zonal flow. Both the velocity and temperature maximum entropy spectra at MODE Center (Figure III.3) suggest a dominant time scale of 16 days similar to the thermocline time scale. Conventional spectral estimates indicate a broad velocity peak at 50 to 100 day periods and suggest a slightly longer temperature time scale. Low frequency estimates cannot be obtained from the 103 day temperature record at MODE East.

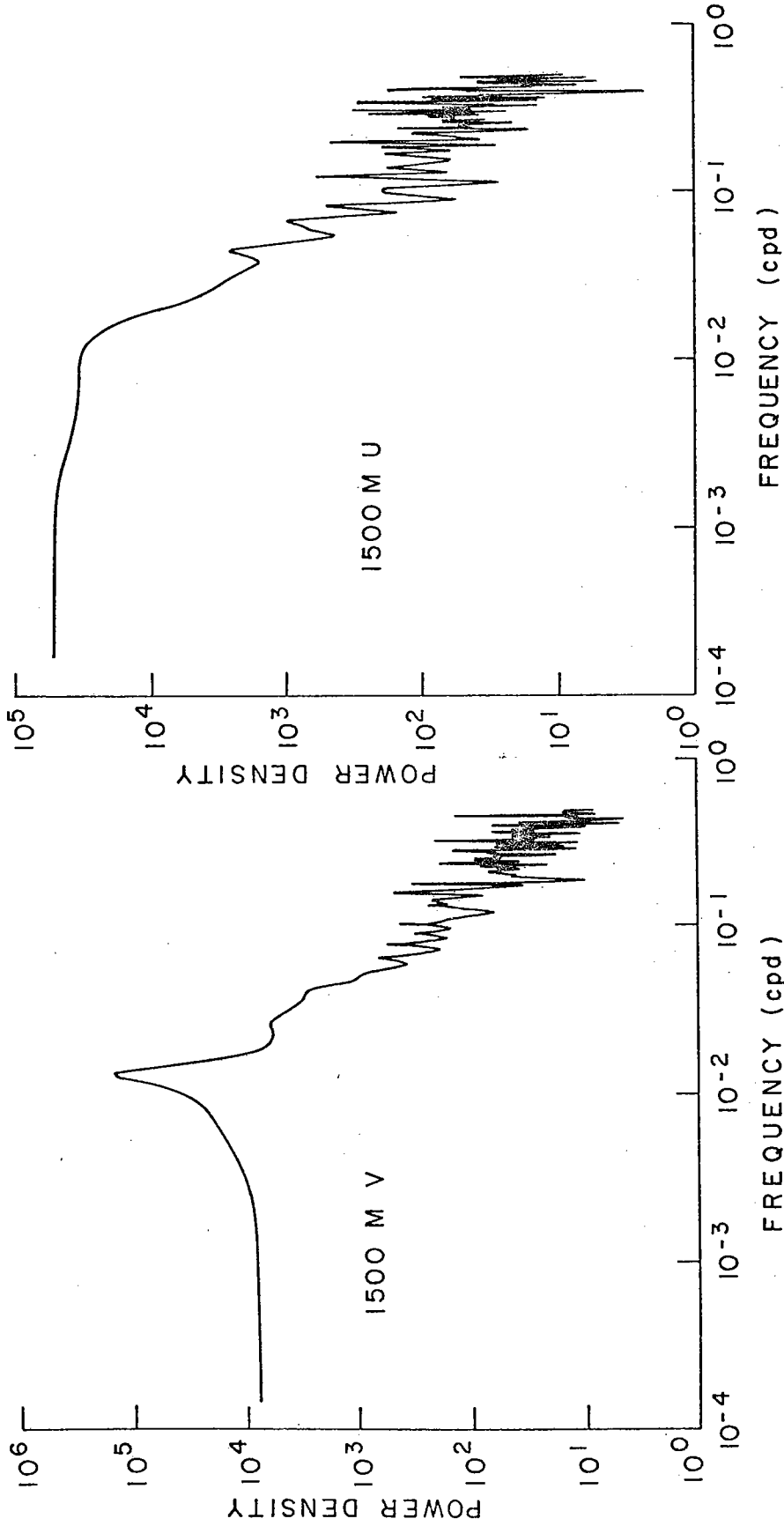


Figure III.3a: Maximum entropy spectra of Mediterranean water velocity at MODE Center

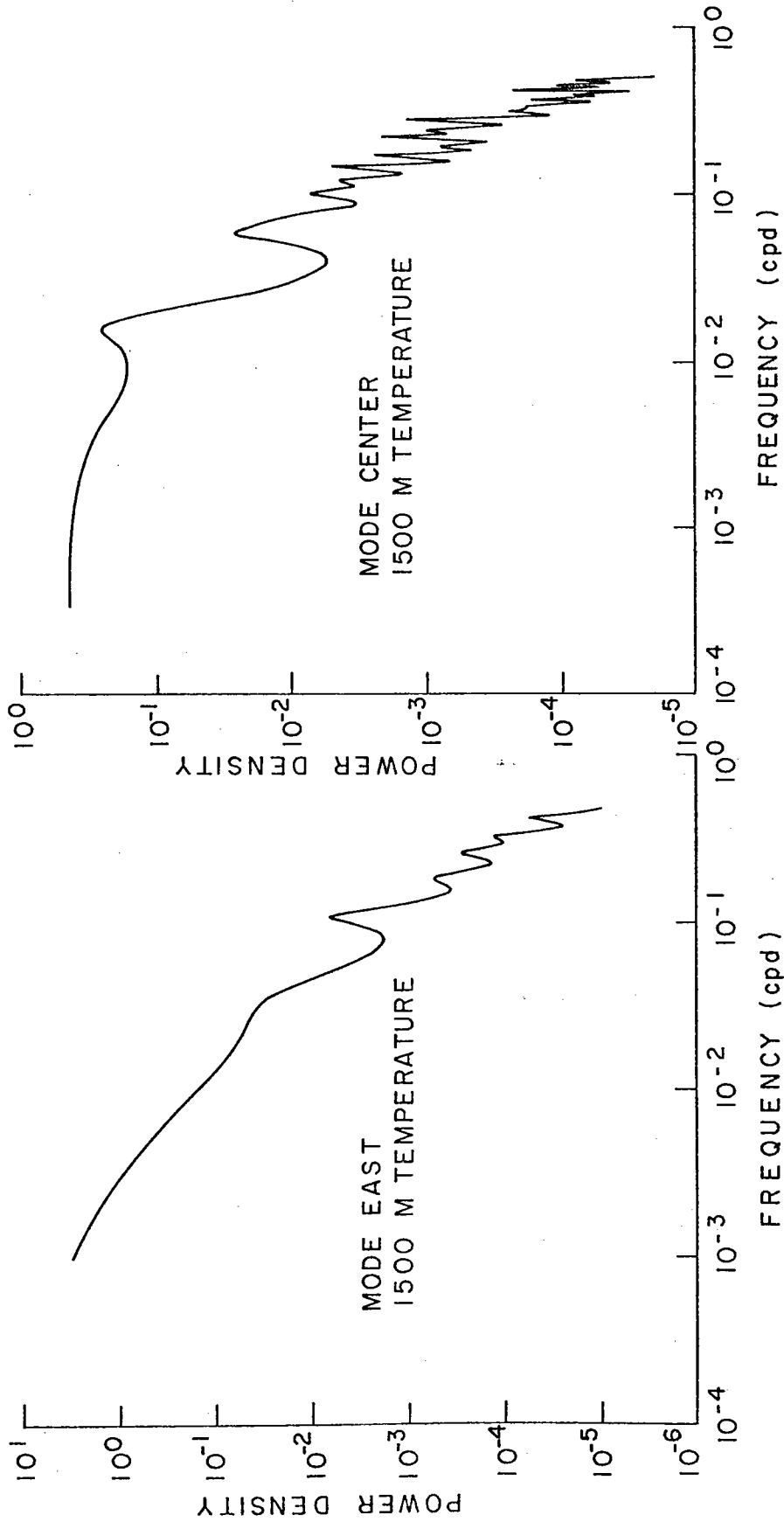


Figure III.3b: Maximum entropy spectra of Mediterranean water temperature

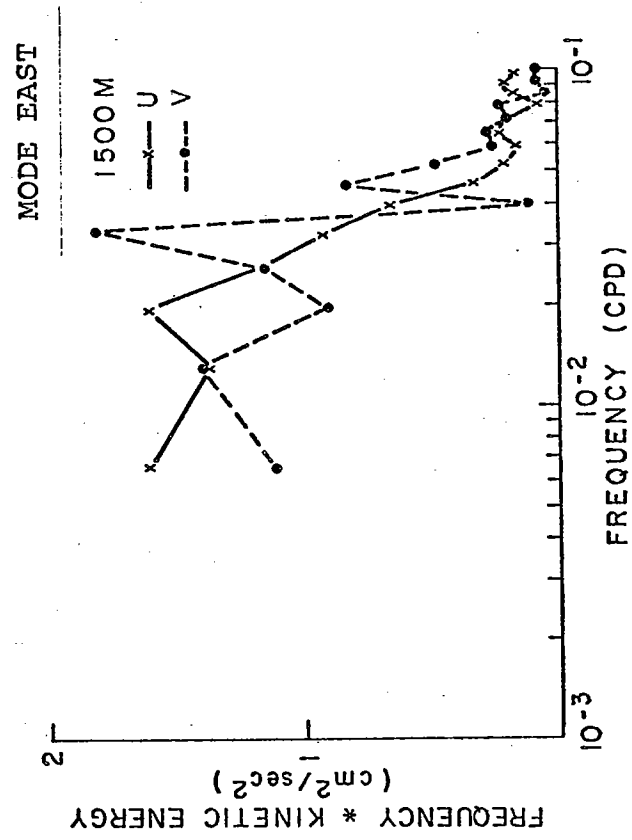
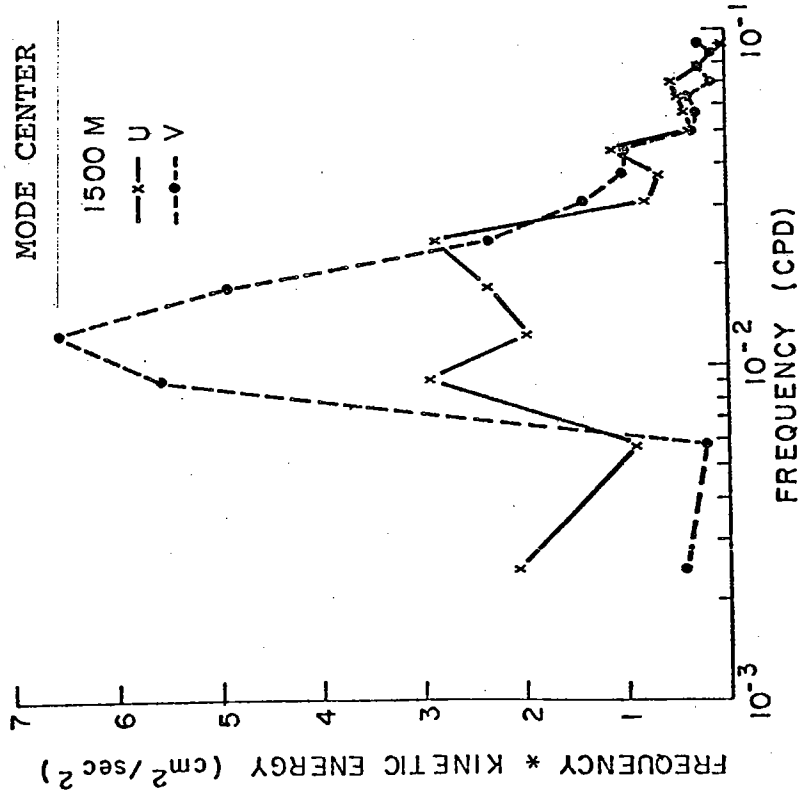


Figure III.4: Zonal and meridional kinetic energy spectra of Mediterranean water

The eastward decrease of kinetic energy, noted in section II.5.2, is obvious in the spectra shown in Figure III.4 and is most pronounced in the meridional rather than zonal kinetic energy. This eastward decrease apparently is confined to the eddy energy containing bands of 80 to 120 day periods. At MODE Center the meridional kinetic energy in this band exceeds the zonal, while at MODE East the meridional and zonal kinetic energy are nearly equal, but smaller than at MODE Center.

Deep water

In the deep water at very low frequencies, periods greater than 200 days, there is a slight excess of zonal kinetic energy over meridional, but it is not significant at 90% confidence. Kinetic energy in the deep water at both site moorings is dominated by a peak between 60 and 120 day periods with the meridional kinetic energy exceeding the zonal. Temperature fluctuations are dominated by a peak between 80 to 100 day periods. The kinetic and potential energy in this band decrease to the east by a factor of two, but the difference is not significant at 90% confidence. At MODE East, the principal axis of the deep flow in the 80 to 120 day band is oriented along geostrophic contours, suggesting topographical control of the flow direction.

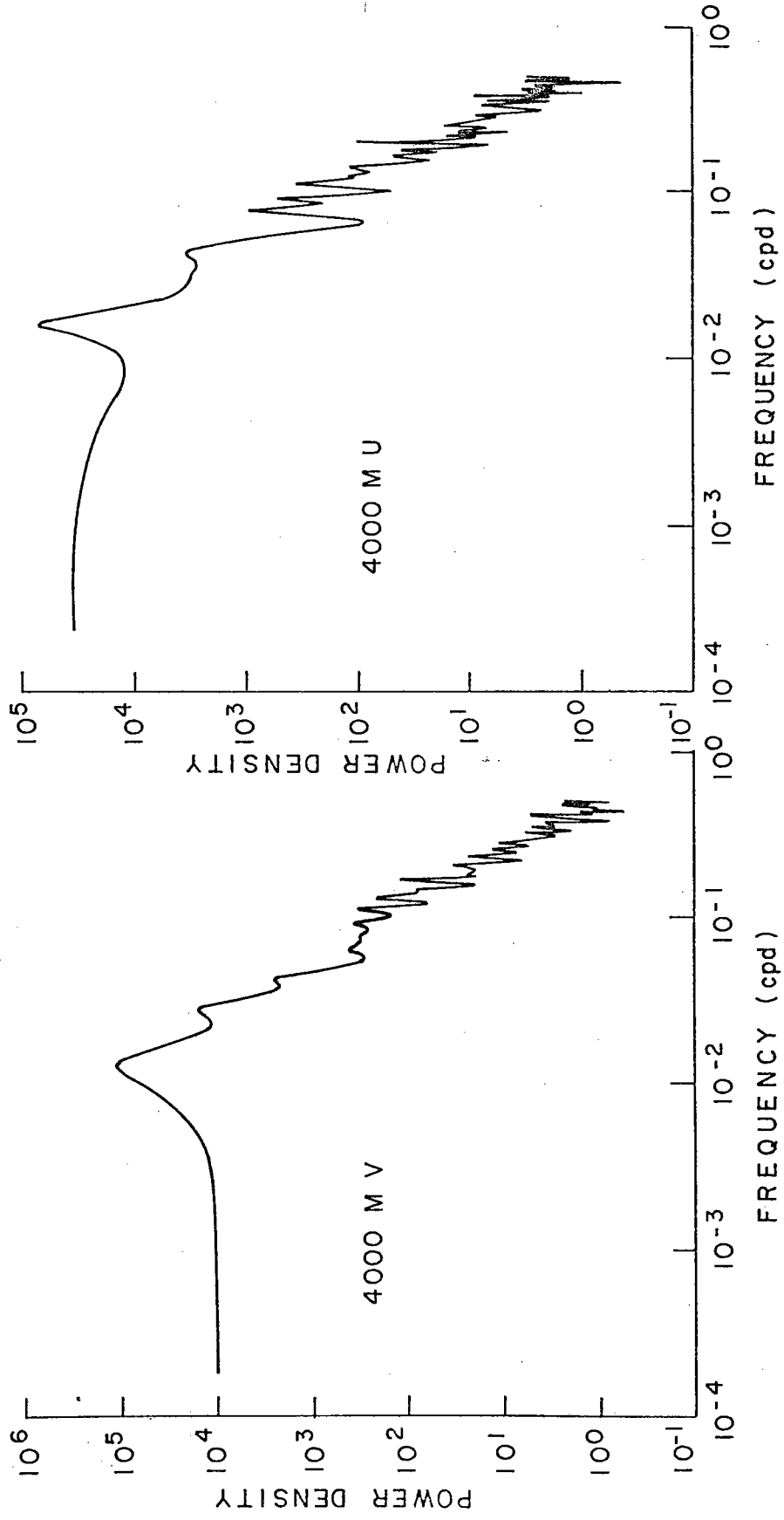


Figure III.5a: Maximum entropy spectra of deep water velocity at MODE Center

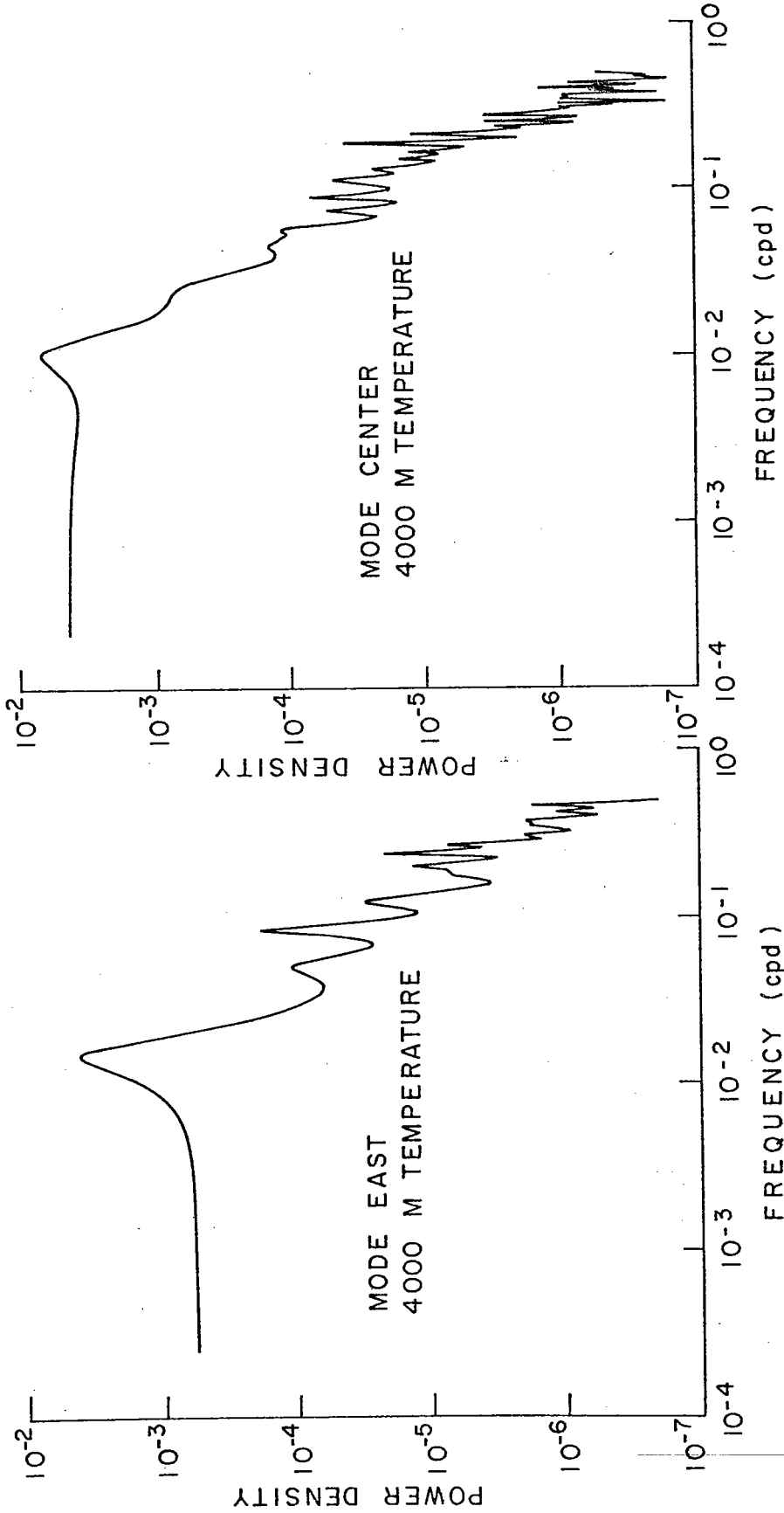


Figure III.b: Maximum entropy spectra of deep water temperature

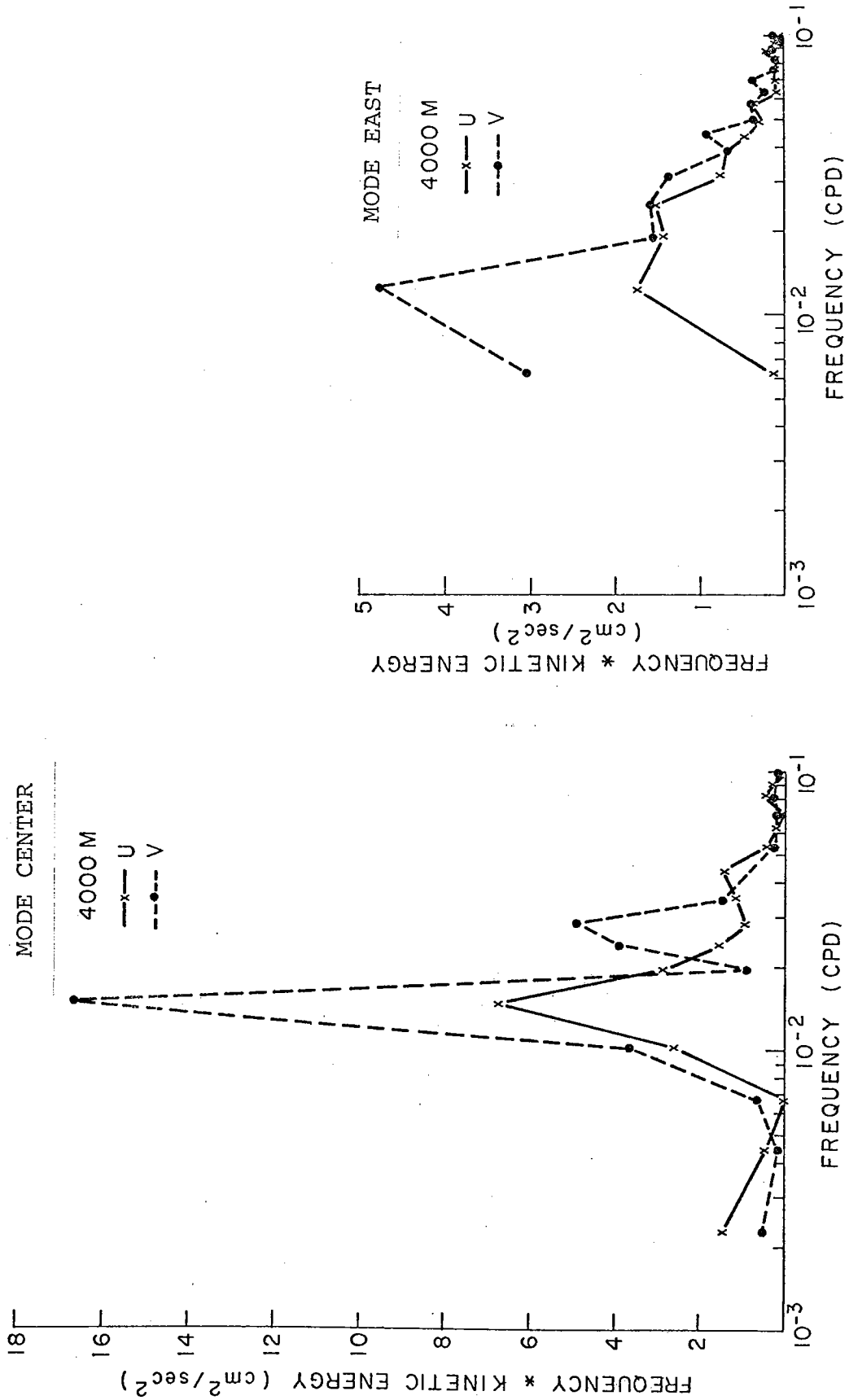


Figure III.6: Zonal and meridional kinetic energy spectra

Vertical comparisons

At MODE Center the kinetic energy spectra at all depths peak between 80 to 120 day periods. In the main thermocline, the dominance of the very low frequency zonal flow partially masks the energy in this band. The greatest contribution to the meridional kinetic energy is from the 80 to 120 day eddy band. Computing the vertical coherence of the velocity at MODE Center by averaging over coincident pieces, the meridional flow in the thermocline is significantly coherent with the deeper flow in both the zonal and meridional components with negligible phase differences at 90% confidence 80% of the time (Table III.1). Leakage of the very low frequency energy into the estimates of the eddy band apparently causes a loss of coherence of the thermocline zonal flow with the deeper flow. Thus, the eddy motion may be characterized by a thermocline intensified flow with no vertical phase difference similar to the first empirical velocity mode calculated by Davis (1975).

At MODE Center as seen in the WKB normalized temperature spectra in Figure III.7, there is a suggestion of a slight shift towards higher frequencies of the eddy energy containing band in the deep water relative to the thermocline. In a broad band from 56 to 306 days, the temperature is coherent with negligible phase difference in the thermocline and deep water with no significant coherence between the two (Table III.2). If the time scale of the temperature decreases with depth, the observed coherence pattern can be reproduced.

Depth	500 m		1500 m		4000 m	
	v	u	v	u	v	
500 m	u	(25°) 0.25	(76°) 0.52	(-120°) 0.54	(133°) 0.50	(-59°) 0.42
	v		(36°) 0.81	(128°) 0.27	(17°) 0.96	(-24°) 0.79
1500 m	u			(-51°) 0.85	(49°) 0.37	(134°) 0.32
	v				(-11°) 0.72	(-14°) 0.81
4000 m	u					(-95°) 0.46

a) 100 day period band

Depth	500 m		1500 m		4000 m	
	v	u	v	u	v	
500 m	u	(127°) 0.36	(-29°) 0.72	(156°) 0.77	(-36°) 0.96	(-177°) 0.43
	v		(89°) 0.64	(59°) 0.69	(-102°) 0.72	(103°) 0.77
1500 m	u			(-80°) 0.94	(-12°) 0.89	(51°) 0.80
	v				(-72°) 0.70	(5°) 0.56
4000 m	u					(-76°) 0.66

b) 50 day period band

Table III.1: Vertical coherence of velocity at
MODE Center

Depth	790 m	1468 m	3492 m	3987 m
495 m	(6°) 0.97	(41°) 0.37	(8°) 0.31	(-10°) 0.31
790 m		(61°) 0.40	(-1°) 0.42	(-9°) 0.38
1468 m			(-130°) 0.32	(-134°) 0.23
3492 m				(10°) 0.94

a) 56 to 305 day period band

Depth	790 m	1468 m	3492 m	3987 m
495 m	(16°) 0.62	(-94°) 0.38	(117°) 0.22	(132°) 0.20
790 m		(-102°) 0.38	(77°) 0.54	(81°) 0.32
1468 m			(163°) 0.61	(134°) 0.29
3492 m				(-8°) 0.48

b) 20 to 56 day period band

Table III.2: Vertical coherence of temperature
at MODE Center

In section II.4.2, two modes, the dominant mode with a thermocline maximum and in phase displacements and a weaker mode with out of phase thermocline and deep water displacements, were required to describe the vertical coherence at MODE Center.

The eastward decrease of kinetic energy apparently is confined to the 80 to 120 day periods band. In section II.5.2, we noted that for a simple kinetic energy model, the eastward decrease is associated with a loss of barotropic energy. At MODE East, the amount of data is inadequate to distinguish a factor of 2 (the magnitude of the kinetic energy decrease) difference in the potential energy levels between the moorings and in the thermocline is inadequate to determine the barotropic and baroclinic kinetic energy in this band. Thus, we cannot determine the vertical structure of the east-west energy differences in the MODE region. The vertical profile data of Sanford and Hogg over the rough topography show a decrease in the vertical shear there compared to the abyssal plain and suggest that the energy difference is also associated with baroclinic motions. If the eastward decrease in kinetic energy is modeled by the scattering of Rossby waves by the abyssal topography (as suggested by Freeland, et al., 1975), then the scattering is confined to the 80 to 120 day band.

In summary, the very low frequency fluctuations in the MODE region have two regimes. For periods greater than 200 days, the zonal kinetic energy is greater than the meridional at all depths. In the thermocline, the very low frequency

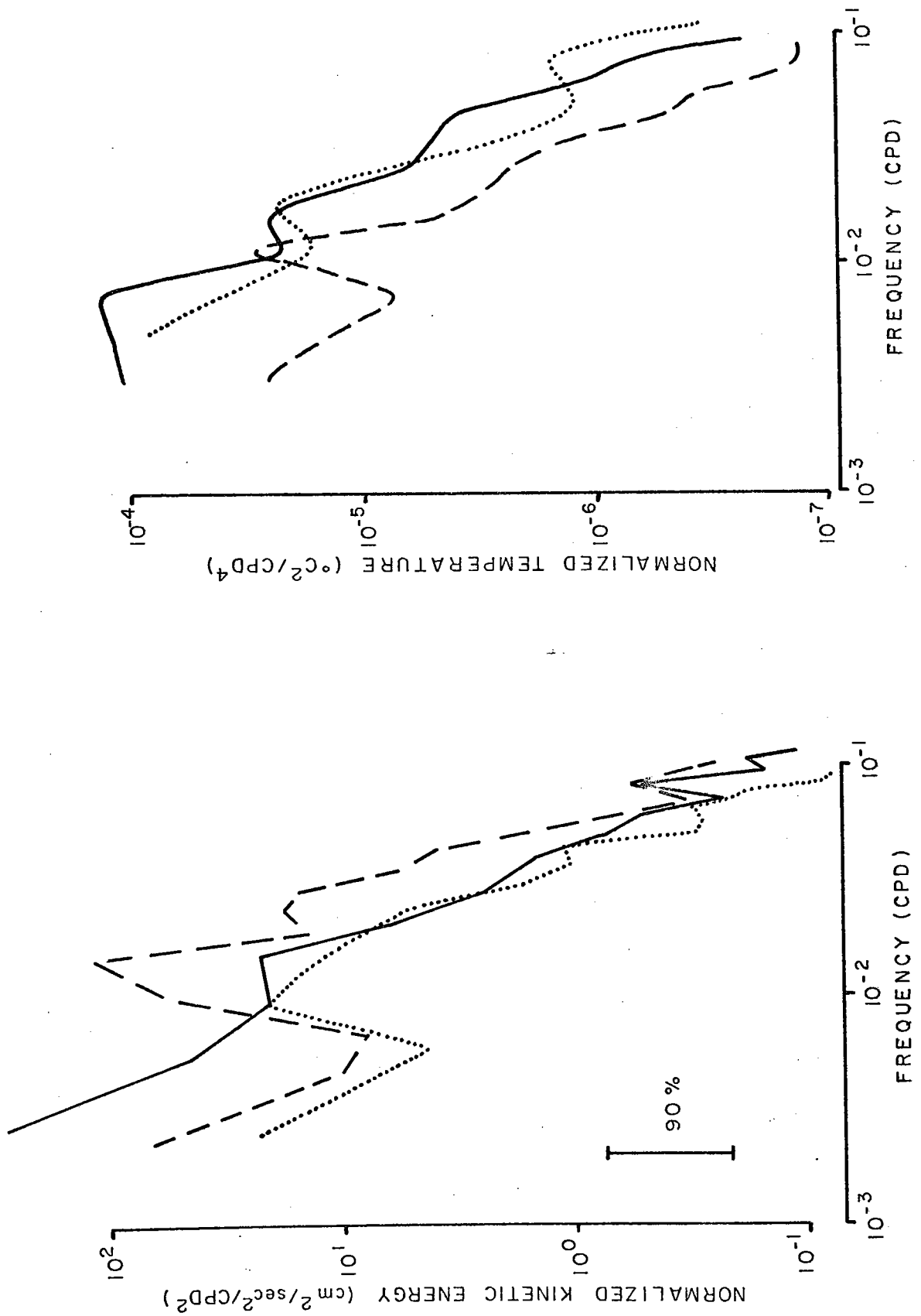


Figure III.7: WKB normalized kinetic energy and temperature at MODE Center

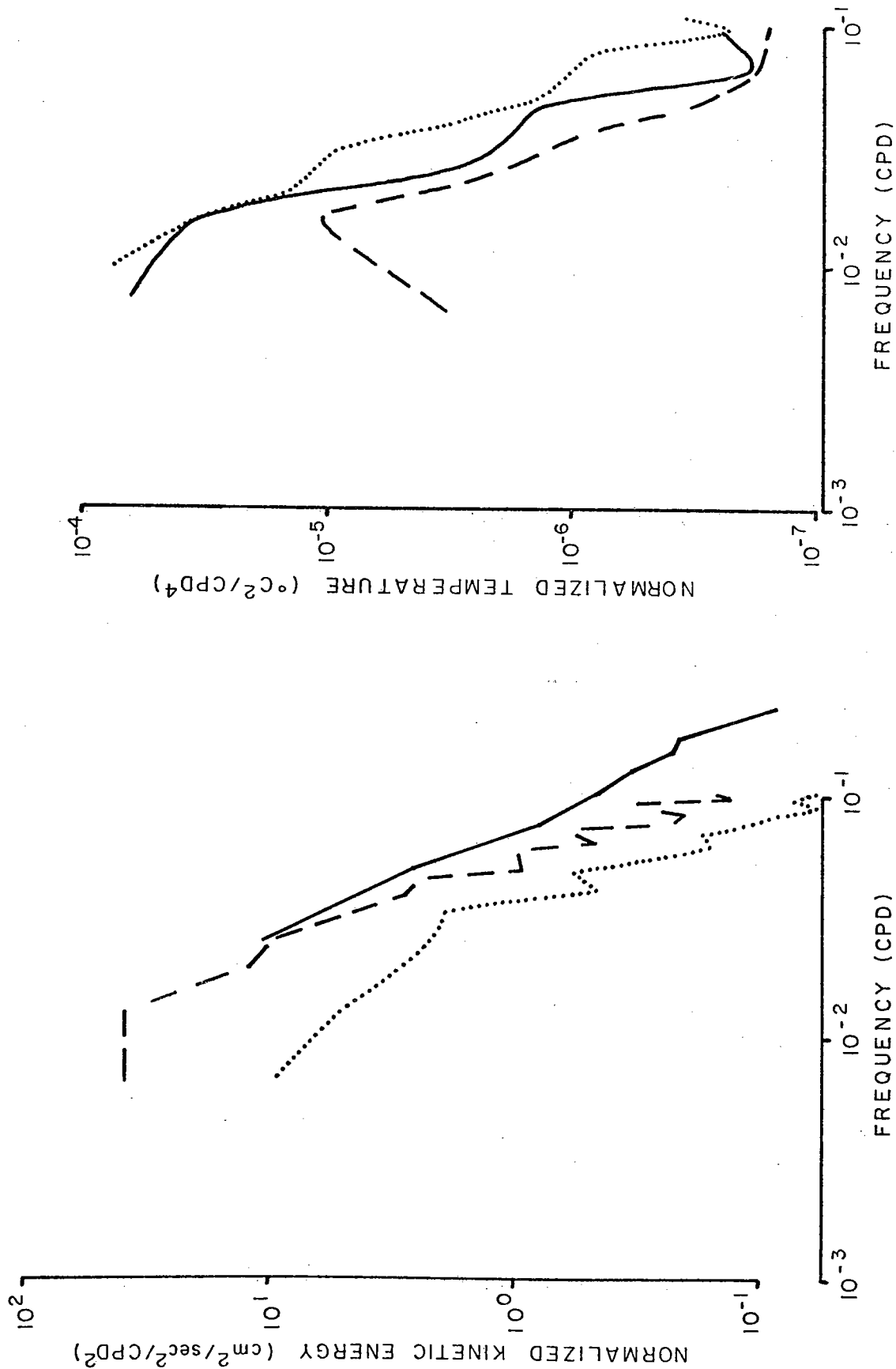


Figure III.8: WKB normalized kinetic energy and temperature at MODE East 500 m (——), 1500 m (.....), and 4000 m (----)

zonal flow dominates the total kinetic energy. At deeper levels and in the thermocline meridional flow, the kinetic energy is dominated by the second regime, an 80 to 120 day eddy energy containing band. The eddy time scale during MODE-I is consistent with the existence of this band. Significant spatial variations of the kinetic energy in this band are observed over the 100 km separation of the site moorings. The mesoscale eddy field in the 80 to 120 day period band is inhomogeneous over the MODE-I spatial scale, at least below the thermocline. Topographic influences are evident at the eastern site mooring and may, at least in part, cause the eddy scale variations.

III.3 Small scale fluctuations

For periods less than 30 days, both the kinetic and potential energy scale with depth in the WKB sense and with frequency as $\omega^{-2.5}$ at both site moorings (see Figures III.7 and III.8). In addition, the partitioning of energy is such that the kinetic energy is divided evenly between the zonal and meridional components and is twice the potential energy. The vertical scale of the high frequency motions is smaller, of the order of 500 m, than for lower frequencies. Temperature coherence is lost for vertical separations greater than 1 km. During MODE-I, the apparent horizontal length scale for these motions was less than 10 km, with no significant coherence over 50 km. However, we should note that a loss of coherence over small separations does not require small

length scales. An isotropic field of independent waves with much longer length scale, such as 50 to 70 km characteristic of the lower frequencies, would show a loss of coherence over 50 km. If the length scale of the high frequencies is as large as 50 km, then we would expect small time scale events to appear at more than one mooring, which is not visually evident in the MODE-I temperature records. While the apparent length scale is short, the kinetic and potential energy are constant over the 100 km separation of the site moorings. Thus, while the eddy energy containing band of 80 to 120 day periods is inhomogeneous over the MODE-I spatial scale, the high frequency band is homogeneous over 100 km.

An occasional intense small scale event is evident in the temperature data, such as the Mediterranean water event around day 140 in 1974, and the thermocline event around day 190 in 1974, at MODE Center, see Figure I.22. While the maximum displacement of 50 m is comparable to the mesoscale eddy displacement during MODE-I, both events have a reversal in the sign of the isotherm displacement over a 1 km depth range unlike the larger scale eddies.

The role of the small scale fluctuations in the redistribution of energy and vorticity is not understood; nor does MODE allow us to investigate these motions. However, the existence of spectral similarity for small scales is suggestive of geostrophic turbulence (Charney, 1971). Later,

in section V.2, we shall consider a comparison of geostrophic turbulence to the small scale fluctuations in the MODE region.

III.4 Summary and discussion

The temporal variability of the low frequency motions in the MODE region may be divided into three regimes. For very low frequencies, periods greater than 200 days, the flow at all depths is anisotropic with the zonal kinetic energy exceeding the meridional. In the thermocline, the very low frequency zonal flow dominates the total kinetic energy. Except for the zonal thermocline flow, the greatest contribution to the kinetic and potential energy tends to come from an eddy energy containing band of 80 to 120 day periods. The observed eddy scale kinetic energy variation is confined to this band. Topographic influences are present at MODE East and may be responsible for the eddy scale variations. At high frequencies, periods less than 30 days, the kinetic and potential energy scale with frequency as $\omega^{-2.5}$ and with depth in the WKB sense. The energy at high frequencies is partitioned evenly between the zonal kinetic, meridional kinetic and potential energy. Unlike the 80 to 120 day eddy band below the thermocline, the high frequency energy at all depths is homogeneous over 100 km.

IV. Possible Dynamical Mechanisms

In the previous chapters, we have looked at the kinematics of the mesoscale circulation, the length and time scales, the energy levels and the anisotropy of the flow. Certain features are apparent. The mesoscale flow is dominated by the very low frequency zonal flow in the main thermocline, by time scales of the order of 15 to 20 days and length scales of the order of 60 km with vertical scale comparable to the ocean depth. At very low frequencies, the flow is anisotropic at all depths with a zonal elongation. For periods less than 30 days, the kinetic and potential energy vary with depth in the WKB sense with vertically similar spectra. The high frequency horizontal length scales are shorter than the low frequencies.

Now, we want to consider some possible dynamical mechanisms for the mesoscale circulation. First, we shall describe the behavior and structure of linear and weakly nonlinear quasi-geostrophic waves in the MODE region. Then, we shall briefly summarize the results of numerical eddy process models (Rhines, 1976) of the development of large scale flow.

IV.1 Quasigeostrophic waves

The idea that the mesoscale flow might be explained in terms of quasigeostrophic waves is not new. Veronis and Stommel (1956) showed that the linear forced response of a baroclinic ocean to a variable wind stress included barotropic and baroclinic Rossby waves. Longuet-Higgins (1965) and

Phillips (1966) considered the Aries observations in terms of Rossby waves while Rhines (1971) suggested that the increase in kinetic energy in the deep water might be due to bottom trapped waves. More recently, Bernstein and White (1974) have noted that the time scales, length scales and phase speeds of temperature fluctuations in the Eastern Pacific are consistent with baroclinic Rossby waves.

In this section we shall compute the structure of linear Rossby waves in a constant depth ocean by a perturbation expansion technique. We shall consider the possible effects of the terms neglected to linearize the quasigeostrophic vorticity equation. Since we expect the nonlinear effects to be important, an analytical theory for weak nonlinear interactions of Rossby waves in a continuously stratified ocean will be presented. Later, the MODE observations will be described in terms of the linear wave modes.

IV.1.1 Computation of the normal modes in the MODE region

If we apply a hydrostatic, quasigeostrophic scaling to the incompressible, Boussinesq equations of motion on a mid-latitude beta plane and expand the equations in powers of the non-dimensional inertial time scale, δ , then we may obtain a vorticity equation at $O(\delta)$

$$\begin{aligned} \nabla_h^2 P_t^{(0)} + \left(\frac{P_z t^{(0)}}{S^2} \right)_z + \beta/\delta P_x^{(0)} & \quad (IV.1.1) \\ = R_0/\delta \left[P_y^{(0)} \nabla_h^2 P_x^{(0)} - P_x^{(0)} \nabla_h^2 P_y^{(0)} - \left(\frac{P_x^{(0)} P_{yz}^{(0)} - P_y^{(0)} P_{xz}^{(0)}}{S^2} \right)_z \right] \end{aligned}$$

(c.f. Eckart, 1960 and Pedlosky, 1971), where β is the non-dimensional gradient of the Coriolis parameter f , $Ro = \frac{U}{f_0 l}$ is the Rossby number, $S^2 = \frac{N^2 H^2}{f_0^2 l^2}$ is the stratification parameter, l is the horizontal length scale, H is the vertical length scale, N is the buoyancy frequency and the pressure $p^{(0)}$ is a geostrophic streamfunction for the lowest order flow. In the MODE region, we expect the order of the non-dimensional parameters to be

$$\delta \sim O(10^{-2}) \quad \beta \sim O(10^{-2})$$

$$S^2 \sim O(1) \quad Ro \sim O(10^{-2} - 10^{-3})$$

While the assumption of linear dynamics is not strictly valid, we will proceed using

$$Ro/\delta \ll 1 \quad \beta/\delta \sim O(1)$$

and consider later the effects of including nonlinearity.

With the additional assumption that the boundary conditions are applied at a rigid surface and flat bottom, we may separate the horizontal and vertical dependence. Thus, the linear vertical structure is determined from the eigenfunctions of the Sturm-Liouville system

$$W' = \rho \tag{IV.1.2}$$

$$\rho' = -m_n^2 S^2 W \tag{IV.1.3}$$

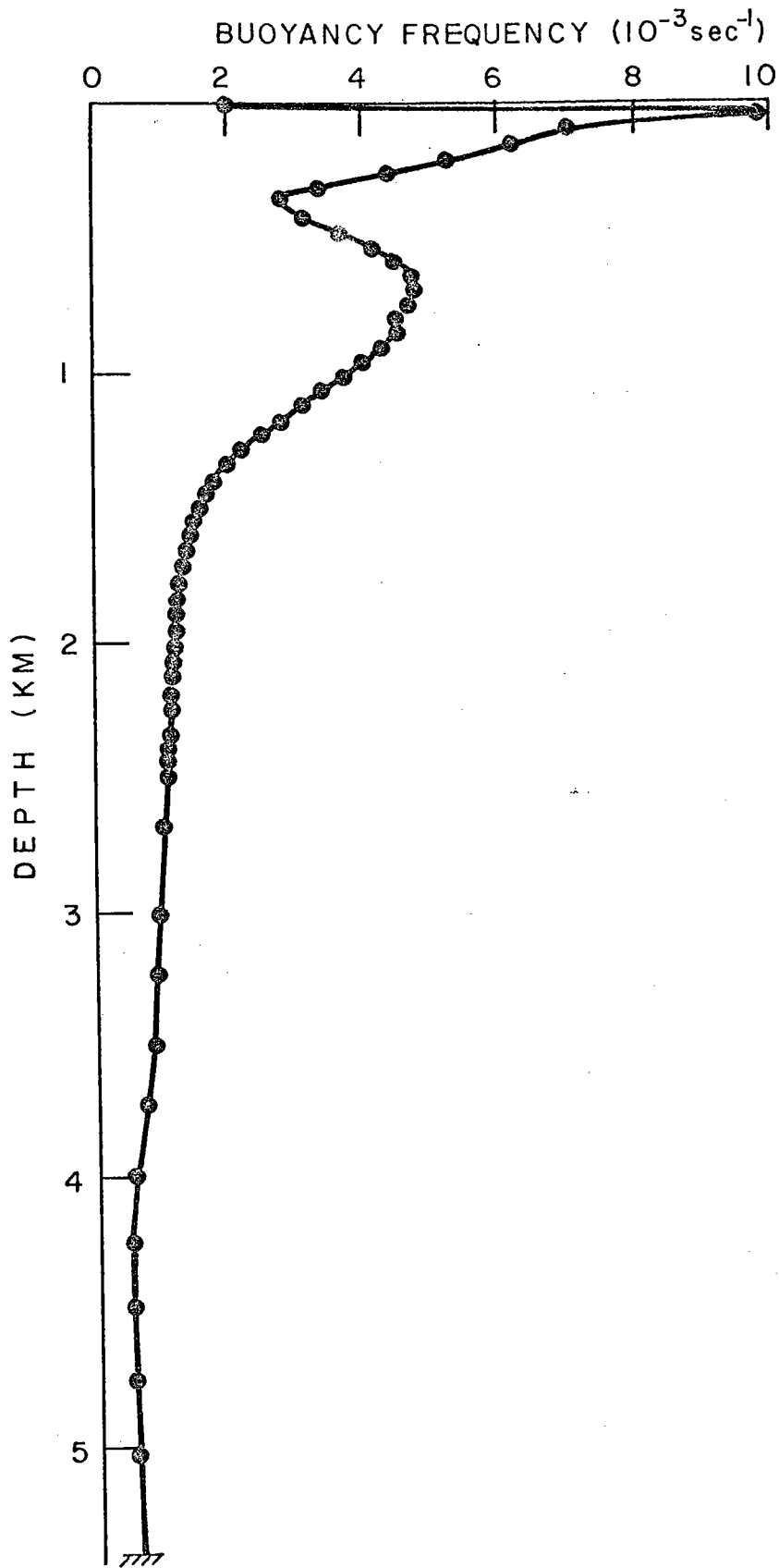


Figure IV.1: MODE region buoyancy frequency profile

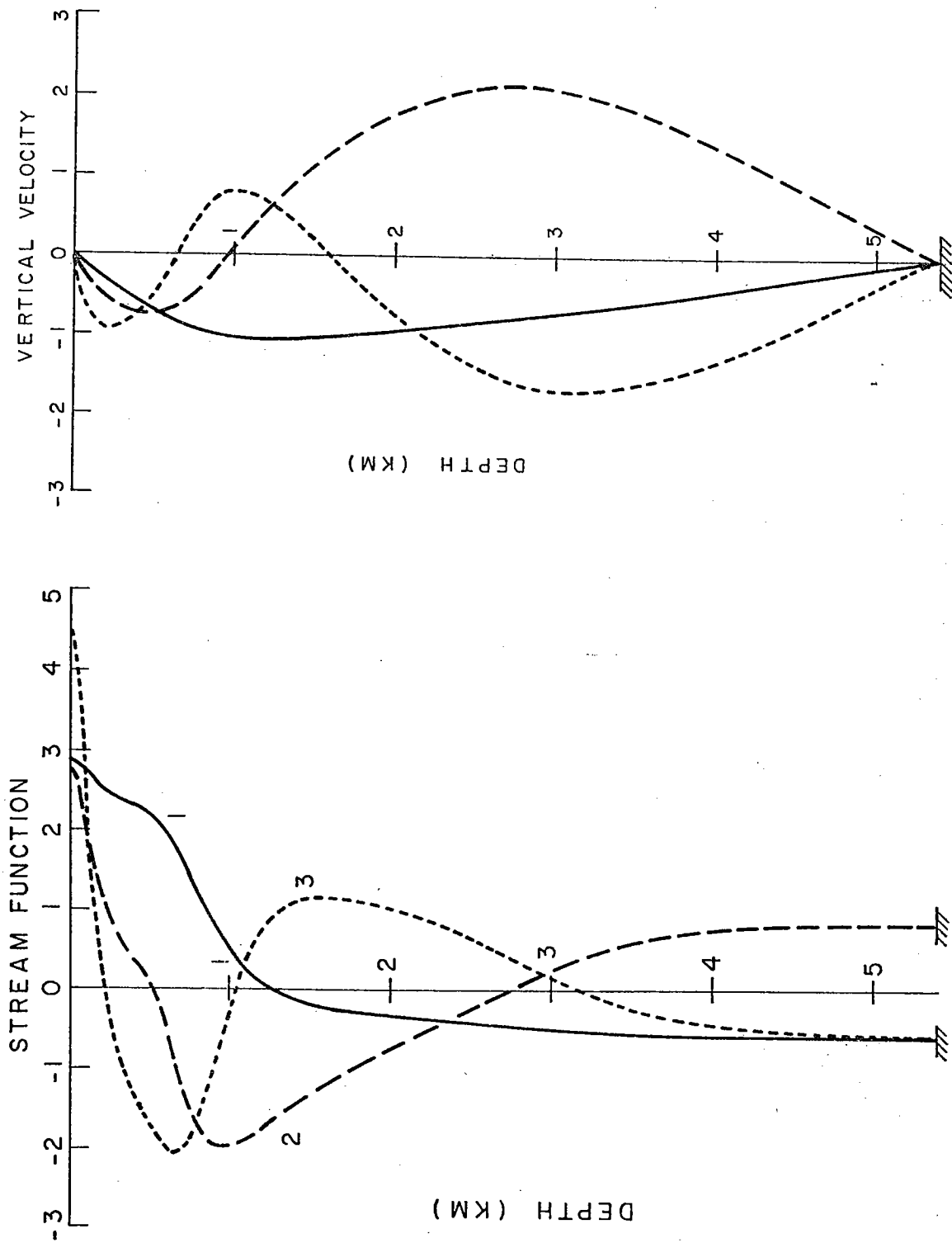


Figure IV.2: Streamfunction and vertical velocity quasigeostrophic normal modes in MODE region

with $w=0$ at $z=0, -1$. For unique eigenvalue m_n^2 , the eigenfunctions are orthogonal with the integral conditions

$$\int_{-1}^0 P_n(z) P_m(z) dz = \delta_{nm} \quad (\text{IV.1.4})$$

and

$$\int_{-1}^0 S^2(z) W_n(z) W_m(z) dz = \delta_{nm} \quad (\text{IV.1.5})$$

where δ_{nm} is the Kronecker delta function. Upon integrating equation IV.1.2 over the water column and applying the boundary conditions, we observe that the streamfunction modes have zero transport. Thus, the barotropic mode

$$P_0(z) = 1 \quad (\text{IV.1.6})$$

is orthogonal to the baroclinic streamfunction modes and accounts for all the net transport. The velocity vertical structure behaves like the streamfunction $U, V \sim P(z)$, while the displacement of the density field behaves like the vertical velocity $\delta = \rho'/\rho_z \sim W(z)$.

For the MODE region, the buoyancy averaged over 20 stations taken during MODE-0 is shown in Figure IV.1 and the corresponding first three normal modes are shown in Figure IV.2. The strongest velocity shears for each mode are confined to the main thermocline and shallower depths and the higher modes dominate the displacement in the deep water.

Mode No.	Eigenvalue (km^{-2})	Equivalent Deformation Radius (km)
1	4.60×10^{-4}	46.7
2	2.53×10^{-3}	19.9
3	4.55×10^{-3}	14.8

Table IV.1: Eigenvalues m_n^2 and equivalent deformation radii $2 / m_n$ for the dynamical normal modes in the MODE region

Mode No.	Maximum Frequency (sec^{-1})	Minimum Period (days)	Wavenumber at Maximum Frequency (km^{-1})
1	4.21×10^{-7}	155	2.14×10^{-2}
2	1.79×10^{-7}	363	5.02×10^{-2}
3	1.34×10^{-7}	487	6.74×10^{-2}

Table IV.2: Maximum frequency baroclinic Rossby wave for MODE region stratification

We may also obtain a dispersion relation for plane wave solutions in the horizontal from the vorticity equation. Assuming solutions of the form $\exp i(kx + ly + \omega t)$ we obtain

$$\omega = - \frac{\beta/\delta \ k}{k^2 + l^2 + m_n^2} \quad (\text{IV.1.7})$$

for each mode. A minimum wave period exists for each mode when the horizontal wavenumber (k, l) is $(-m_n, 0)$. In the MODE region, the minimum period for a first baroclinic mode wave is 155 days and increases for higher modes. An equivalent radius of deformation $2\pi/m_n$ may be defined for each mode. For a first mode baroclinic mode the deformation radius is 47 km comparable to the observed dominant length scale in the main thermocline. The equivalent deformation radius decreases with increasing mode number.

We need to consider at least briefly the possible effects of terms neglected in the perturbation expansion. The largest term is the nonlinearity of the fluctuating field, of order R_0/δ . For a wave field the importance of the nonlinearity may be expressed as U/c , the ratio of the particle speed to the phase speed of the wave. In the MODE region, using the baroclinic energy estimate from the site moorings and assuming near deformation scale westward propagating wave, $U/c = 1.2$, while for the barotropic energy and similar scale wave $U/c = 0.5$. Thus the

nonlinear effects will be important. Gill (1974) found that barotropic waves of all wavelengths are unstable. In the limit as $U/c \rightarrow 0$, the instability takes the form of a resonant triad interaction discussed by Longuet-Higgins and Gill (1967). Kim (1975) investigated the stability of a two layer finite amplitude baroclinic Rossby wave. The instability occurs in both the barotropic and baroclinic mode. The nonlinear interaction transfers energy from both large and small horizontal scales towards the internal radius of deformation. We shall discuss the later weakly nonlinear interactions for a continuously stratified ocean.

Killworth and Anderson (1975a,b,c) in a series of cautionary notes have warned of the possible effects of neglecting advection by the mean flow in computing the vertical structure. For a barotropic mean flow, the eigenmodes are unchanged, but a doppler frequency shift is induced, $\omega = \omega_0 + \bar{u} \cdot \underline{k}$. For a mean westward flow of 0.5 cm/sec, the minimum first mode wave period is decreased to 122 days, closer to the observed dominant period in the main thermocline than a free wave. However, in the presence of mean shear, the eigenvalue problem is changed drastically. The mode shapes depend on both the mean flow \bar{u} and the wavenumber \underline{k} . The resultant eigenmodes are not a complete set. Unstable modes exist converting mean potential energy into eddy kinetic energy. Gill, Green, and Simmons (1974) and Robinson and

McWilliams (1974) have calculated growth rates of the order of a few months for a westward shear of 5 cm/sec in the upper 500 m. McWilliams (1974) estimated the mean shear in the MODE region from the historical data. The small flow is confined to the upper 400 m and predominantly eastward. The resultant modes are stable with the shape changes confined predominantly to the upper 500 m. Thus while advection by the mean shear could potentially affect the interpretation of the vertical structure calculations, we expect the inherent nonlinearity of the mesoscale flow to be more important.

Rhines and Bretherton (1973) considered the effects of bottom topography on propagating Rossby waves. The resultant vertical structure depends on the scale of the wave, the horizontal and vertical scales of the topography and the orientation of the wave. For long waves over isotropic bottom roughness, the frequency of the wave is increased and energy flux decreased. We expect the effects of bottom topography to be confined to the deep water.

In the next section, we shall consider the effects of weak nonlinearity on quasigeostrophic oscillations. While in the weakly nonlinear limit, the vertical structure of the modes is unchanged, the exchange of energy between the modes can lead to a coupling of the modes over a short experiment.

IV.1.2 Weak nonlinear interactions

In section IV.1.1 the normal modes were obtained by assuming the nonlinear interactions were negligible, $R_0/\delta \ll \delta$

We may analytically investigate the weakly nonlinear interactions in a continuously stratified ocean through the technique of two time scale perturbation, assuming $R_0/\delta < \delta \ll 1$ (Cole, 1968). Kenyon (1964) and Longuet-Higgins and Gill (1967) have investigated the resonant interactions of barotropic Rossby waves.

We expand the pressure in terms of the second time scale

$$p^{(0)} = p^{(0,0)} + R_0/\delta p^{(0,1)} + \dots \quad (\text{IV.1.8})$$

The pressure streamfunction $p^{(0,0)}$ is given by equations IV.1.2 and IV.1.3 to $O(R_0/\delta)$. We use the $O(R_0/\delta)$ balance equations to obtain corrections for the variation of the streamfunction on the long time and horizontal length scales,

$$T = (R_0/\delta)^{-1} t \quad \underline{X} = (R_0/\delta)^{-1} \underline{x}$$

as given by

$$\begin{aligned} \nabla_h^2 p_t^{(0,1)} + \left(\frac{P_{zt}}{S^2} \right)_z + \beta/\delta p_x^{(0,1)} - p_y^{(0,0)} \nabla_h^2 p_x^{(0,0)} \\ + p_x^{(0,0)} \nabla_h^2 p_y^{(0,0)} + \left(\frac{p_x^{(0,0)} p_{yz}^{(0,0)} - p_y^{(0,0)} p_{xz}^{(0,0)}}{S^2} \right)_z \\ + \nabla_h^2 p_T^{(0,0)} + \left(\frac{P_{zT}}{S^2} \right)_z + \beta/\delta p_x^{(0,0)} \quad (\text{IV.1.9}) \\ + 2 \nabla_{\underline{X}} \cdot \nabla_h p_t^{(0,0)} = 0 \end{aligned}$$

A single wave obeying the dispersion relation IV.1.7 is an exact solution to IV.1.1. Since the nonlinearity occurs at second order in the weak nonlinear interaction theory for Rossby waves, we expect a resonant triad exchange between waves. Thus we shall consider solutions of the form

$$p^{(0,0)} = \sum_{j=1}^3 P_{n_j}(z) a_j(\underline{X}, T) \cos(k_j x + l_j y - \omega_{j;n_j} t - \phi(\underline{X}, T)) \quad (\text{IV.1.10})$$

where n_j is the mode number of the j th number of the triad, $a_j(\underline{X}, T)$ is the amplitude modulation of the wave due to the exchange and $\phi_j(\underline{X}, T)$ is the phase modulation. To prevent secular growth of $p^{(0,1)}$ in equation IV.1.1, we seek solutions for the amplitude and phase modulation in the resonance equations

$$\begin{aligned} (K_j^2 + m_{n_j}^2) \left(\frac{\partial a_j}{\partial T} + \xi_j \cdot \nabla_{\underline{X}} a_j \right) \\ = \frac{\alpha b}{2} \left((K_l^2 + m_{n_l}^2) - (K_k^2 + m_{n_k}^2) \right) \cos \phi_0 a_k a_l \end{aligned} \quad (\text{IV.1.11})$$

and

$$\begin{aligned} (K_j^2 + m_{n_j}^2) a_j \left(\frac{\partial \phi_j}{\partial T} + \xi_j \cdot \nabla_{\underline{X}} \phi_j \right) \\ = \frac{\alpha b}{2} \left((K_l^2 + m_{n_l}^2) - (K_k^2 + m_{n_k}^2) \right) \sin \phi_0 a_k a_l \end{aligned} \quad (\text{IV.1.12})$$

with the constraint that

$$\sum_{j=1}^3 \psi_j = \phi_0 \quad (\text{IV.1.13})$$

where
$$\psi_j = k_j x + l_j y - \omega_j t + \phi_j(\underline{x}, \tau) \quad (\text{IV.1.14})$$

$$b = \hat{z} \cdot (k_j \times k_k) \quad (\text{IV.1.15})$$

and
$$\alpha = \int_{-1}^0 \rho_{n_j}(z) \rho_{n_k}(z) \rho_{n_l}(z) dz \quad (\text{IV.1.16})$$

where (j, k, l) are cyclic over $(1, 2, 3)$, K_j is the magnitude of the horizontal wavenumber and c_j the group velocity of the j th wave. Forced wave solutions will also exist to IV.1.1, but we shall not consider them formally as their amplitudes will be order R_0/δ .

If $\phi_0 = 0, \pi$ then IV.1.12 reduces to

$$\left[\frac{\partial}{\partial \tau} + c_j \cdot \nabla_x \right] \phi_j = 0 \quad (\text{IV.1.17})$$

and no phase shift of the waves occurs along group velocity rays. If $\phi_0 = \pm\pi/2$, the IV.1.11 reduces to

$$\left[\frac{\partial}{\partial \tau} + c_j \cdot \nabla_x \right] a_j = 0 \quad (\text{IV.1.18})$$

and the wave amplitude is constant along rays. We may also obtain two conservation principles for the interaction:

1) The total energy in the waves is conserved

$$\frac{\partial}{\partial \tau} \left[\sum_{j=1}^3 (K_j^2 + m_{n_j}^2) a_j^2 \right] = 0 \quad (\text{IV.1.19})$$

and 2) the total pseudo-potential vorticity is conserved

$$\frac{\partial}{\partial T} \left[\sum_{j=1}^3 (K_j^2 + m_{n_j}^2)^2 a_j^2 \right] = 0 \quad (\text{IV.1.20})$$

From the conservation principle we can calculate the direction of the energy exchange between the waves

$$\begin{aligned} \frac{K_1^2 + m_{n_1}^2}{(K_3^2 + m_{n_3}^2) - (K_2^2 + m_{n_2}^2)} \Delta_1 &= \frac{K_3^2 + m_{n_3}^2}{(K_2^2 + m_{n_2}^2) - (K_1^2 + m_{n_1}^2)} \Delta_3 \\ &= - \frac{K_2^2 + m_{n_2}^2}{(K_3^2 + m_{n_3}^2) - (K_1^2 + m_{n_1}^2)} \Delta_2 \end{aligned} \quad (\text{IV.1.21})$$

where

$$\Delta_j = a_j^2 (\bar{X}, T) - a_j^2 (\bar{X}_0, T_0) \quad (\text{IV.1.22})$$

the change in the amplitude squared from some initial state.

Assuming that

$$K_1^2 + m_{n_1}^2 < K_2^2 + m_{n_2}^2 < K_3^2 + m_{n_3}^2$$

then the energy is transferred from the higher and lower "wavenumber" waves to the intermediate wave. We note that the transfer relations include the eigenvalue of the vertical mode of each wave (wavenumber associated with the equivalent deformation radius of the mode), as well as the horizontal wavenumber so the usage of higher, lower and intermediate "wavenumber" is not conventional. Similarly, the rate of

change of the phase of the intermediate wave is opposite the rate of change of the other two members of the triad.

In general the interaction rate is governed by the integral IV.1.16 which gives the total overlap of the three interacting modes. The integral condition arises from the expansion of the product of two modal shapes in terms of the normal modes themselves

$$P_{n_j}(z) P_{n_k}(z) = \sum_{m=0}^{\infty} d_m P_m(z) \quad (\text{IV.1.23})$$

Clearly then, one simple class of allowed interactions is a triad consisting of a barotropic wave and two j th mode baroclinic waves. In the case of constant stratification ($S=\text{constant}$), a selection rule for the vertical mode number may be obtained with

$$n_1 \pm n_2 \pm n_3 = 0 \quad (\text{IV.1.24})$$

However, this simple rule does not generalize for arbitrary stratification. For the observed stratification in the MODE region the integral condition IV.1.16 effectively damps very few interactions between low mode numbers.

If we assume that the total phase ϕ_0 of the triad is constant and consider only temporal variation of the amplitude and phase of the waves, then we may obtain solutions to IV.1.11 in terms of Jacobi elliptic functions (Neville, 1944).

The assumption of constant total phase simplifies the interactions, because the phase modulations do not affect the amplitude modulations. If the total phase varies with time, then the amplitude fluctuation will be modified by the phase, complicating the form of the solution. However, the conservation principles governing the energy exchange between the waves are still valid with one wave growing (decaying) at the expense (benefit) of the other two. For constant total phase, the triad amplitude modulations are

$$a_1 = \alpha_1 \operatorname{cn} \left(\left(\frac{T}{T_0} - \lambda \right) | \Upsilon^2 \right) \quad (\text{IV.1.25})$$

$$a_2 = \alpha_2 \operatorname{sn} \left(\left(\frac{T}{T_0} - \lambda \right) | \Upsilon^2 \right) \quad (\text{IV.1.26})$$

and

$$a_3 = \alpha_3 \operatorname{dn} \left(\left(\frac{T}{T_0} - \lambda \right) | \Upsilon^2 \right) \quad (\text{IV.1.27})$$

where cn , sn , and dn are Jacobi elliptic functions of modulus Υ . From the initial conditions at $T=0$ we may obtain

$$\alpha_1 = \alpha_{10} \left(1 - \operatorname{sn}^2(\lambda | \Upsilon^2) \right)^{1/2} \quad (\text{IV.1.28})$$

$$\alpha_2 = \alpha_{20} \operatorname{sn}(\lambda | \Upsilon^2) \quad (\text{IV.1.29})$$

and

$$\alpha_3 = \alpha_{30} \left(1 - \Upsilon^2 \operatorname{sn}^2(\lambda | \Upsilon^2) \right)^{1/2} \quad (\text{IV.1.30})$$

$$T_0 = \frac{2}{\alpha b} \frac{\left[\frac{(K_1^2 + m_{n_1}^2)(K_2^2 + m_{n_2}^2)}{(K_3^2 + m_{n_3}^2 - (K_1^2 + m_{n_1}^2))(K_3^2 + m_{n_3}^2 - (K_2^2 + m_{n_2}^2))} \right]^{1/2}}{\alpha_{30} (1 - \gamma^2 \xi^2)^{1/2} \cos \phi_0} \quad (\text{IV.1.31})$$

$$\lambda = \sin^{-1}(\xi | \gamma^2) \quad (\text{IV.1.32})$$

$$\gamma^2 = \frac{1}{2 \xi^2} - \left[\frac{1}{4 \xi^2} - \frac{(1 - \xi^2) \alpha_{10}^2}{\xi^2 \alpha_{30}^2} \frac{(K_2^2 + m_{n_2}^2)}{(K_3^2 + m_{n_3}^2)} \right. \\ \left. \times \frac{(K_2^2 + m_{n_2}^2 - (K_1^2 + m_{n_1}^2))(K_3^2 + m_{n_3}^2 - (K_1^2 + m_{n_1}^2))}{(K_3^2 + m_{n_3}^2 - (K_2^2 + m_{n_2}^2))} \right]^{1/2} \quad (\text{IV.1.33})$$

and

$$\xi = \left[\frac{(K_1^2 + m_{n_1}^2)(K_3^2 + m_{n_3}^2 - (K_1^2 + m_{n_1}^2)) \alpha_{10}^2}{(K_2^2 + m_{n_2}^2)(K_3^2 + m_{n_3}^2 - (K_2^2 + m_{n_2}^2)) \alpha_{30}^2 + (K_1^2 + m_{n_1}^2)(K_3^2 + m_{n_3}^2 - (K_1^2 + m_{n_1}^2)) \alpha_{10}^2} \right]^{1/2} \quad (\text{IV.1.34})$$

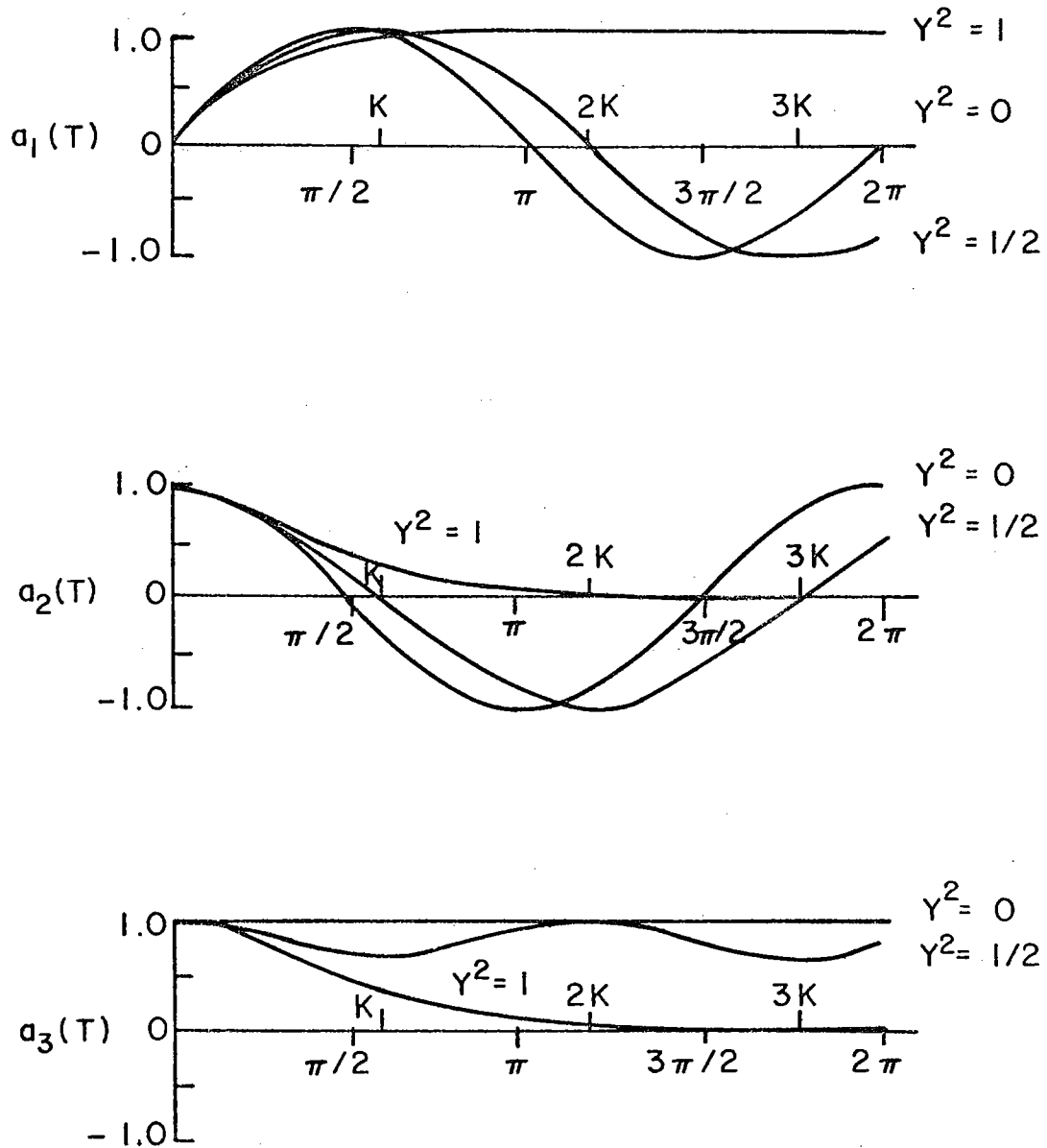


Figure IV.3: Schematic amplitude modulations for interacting triad

The general trend of the amplitude modulations is sketched in Figure IV.3, showing the exchange of energy from the higher and lower waves into or from the intermediate wave as expected from IV.1.21.

We have yet to determine the wavenumber structure of the interacting triads. From IV.1.13 we observe that

$$\underline{k}_1 \pm \underline{k}_2 \pm \underline{k}_3 = 0 \quad (\text{IV.1.35})$$

and
$$\omega_1 \pm \omega_2 \pm \omega_3 = 0 \quad (\text{IV.1.36})$$

are required to form an interacting triad. However, not all of the possible triads will have a nonzero rate of interaction. Substituting the dispersion relation IV.1.7 into IV.1.36 and letting

$$\underline{k}_1 = -\frac{1}{2} \underline{k}_2 + \frac{1}{2} \underline{k}_0 \quad (\text{IV.1.37})$$

$$\underline{k}_3 = -\frac{1}{2} \underline{k}_2 - \frac{1}{2} \underline{k}_0 \quad (\text{IV.1.38})$$

and
$$\underline{k} = K (\cos \theta, \sin \theta) \quad (\text{IV.1.39})$$

we obtain a quartic equation for K_0 in terms of k_2 and θ_0 ,

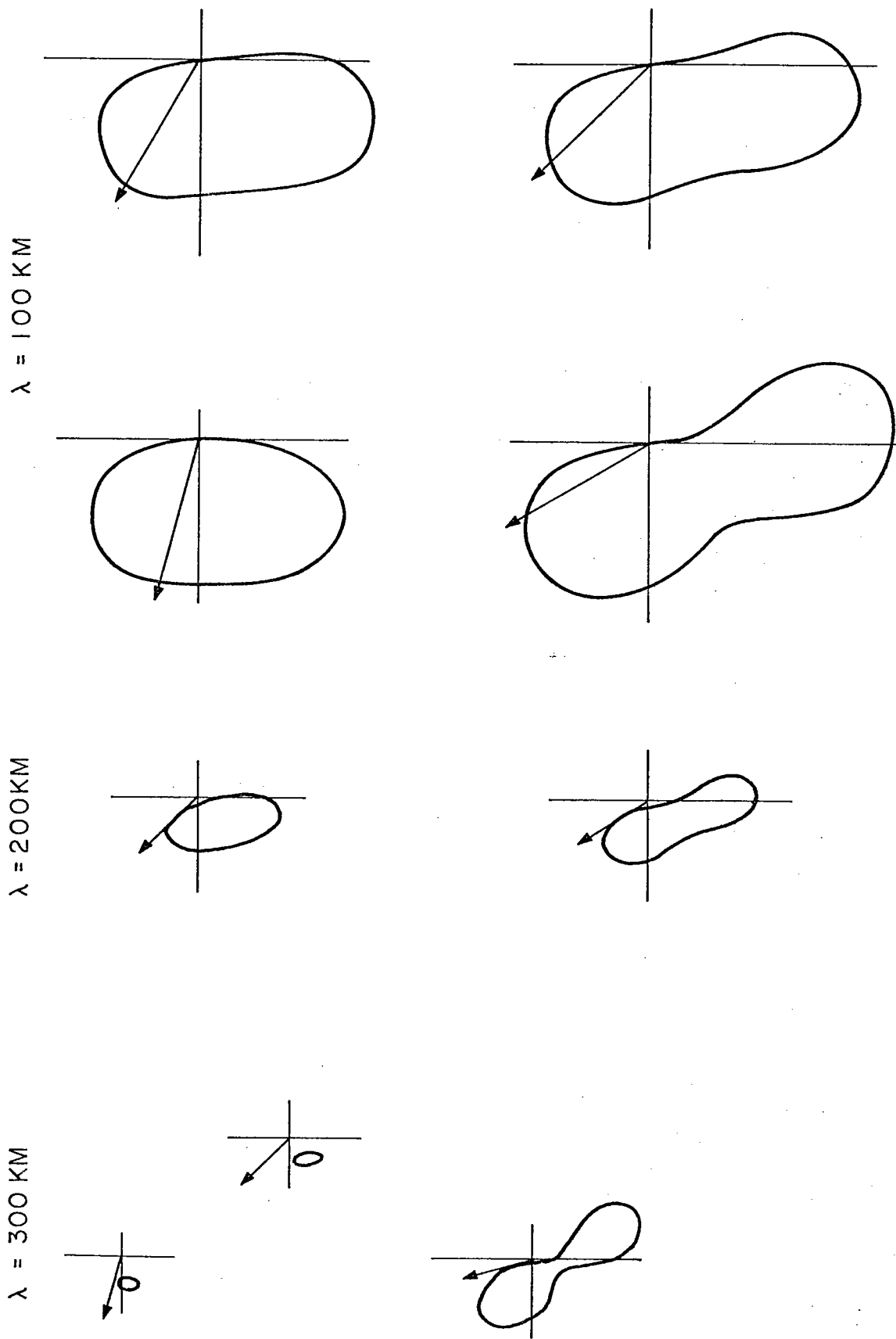


Figure IV, 4: Loci of wavenumbers of first baroclinic mode waves with barotropic wave given by arrow

$$\begin{aligned}
& K_0^4 (K_2 \cos \theta_2) \\
& + K_0^2 \left[8 K_2 (K_2^2 + m_{n_2}^2) \cos \theta_0 \cos \theta_0 - \theta_2 - 2 K_2^3 \cos \theta_2 \right. \\
& \quad - 4 K_2 m_{n_2}^2 \cos \theta_2 - 4 K_2^3 \cos \theta_2 \cos^2 \theta_0 - \theta_2 \\
& \quad \left. + 4 K_2 (m_{n_1}^2 + m_{n_3}^2) \cos \theta_2 \right] \quad (\text{IV.1.40}) \\
& + K_0 \left[8 K_2^2 (m_{n_1}^2 - m_{n_3}^2) \cos \theta_2 + 8 (m_{n_1}^2 - m_{n_3}^2) (K_2^2 + m_{n_2}^2) \cos \theta_0 \right] \\
& \quad + 8 K_2^2 (2 m_{n_1}^2 m_{n_3}^2 - m_{n_1}^2 m_{n_2}^2 - m_{n_2}^2 m_{n_3}^2) \cos \theta_2 \\
& \quad - K_2^2 (3 K_2^2 + 4 (m_{n_1}^2 + m_{n_2}^2 + m_{n_3}^2)) \cos \theta_2 = 0
\end{aligned}$$

If two members of the triad have the same vertical mode number, $n_1 = n_3$, then IV.1.40 reduces to a quadratic equation in K_0^2 and for a given k_2 the other members of a triad may be found. When $m_{n_1} = m_{n_2} = m_{n_3} = 1$, IV.1.40 reduces to the results of Longuet-Higgins and Gill (1967) for resonant interactions of barotropic Rossby waves.

Loci of interacting triads for a barotropic and two first mode baroclinic waves for selected barotropic wave numbers are shown in Figure IV.4. We note the visual similarity of the loci with those for barotropic waves alone shown in Longuet-Higgins and Gill, Figures 1-4. A cutoff exists for the interaction; no triad exists for a barotropic wave with wavelength greater than 325 km in the MODE region.

As the barotropic wavelength increases, the locus of baroclinic triad members decreases and the rate of interaction decreases as the triad members become nearly colinear. Similarly, a cutoff for higher baroclinic waves interacting with a barotropic wave exists at a wavelength slightly greater than 2π times the associated deformation radius of the baroclinic mode. Thus, it is not possible for long barotropic Rossby waves to obtain energy from baroclinic waves.

The effect of the interaction on the structure of the wave field will be governed by the modulus γ and the modulation period T_0 of the Jacobi elliptic functions. As the modulus approaches zero, two waves exchange energy with sinusoidally varying amplitude with the third wave acting primarily as a catalyst. The rate of energy exchange is determined by the period of the modulation and the wave amplitudes. Kim (1975) in a study of the stability of finite amplitude baroclinic Rossby waves found a maximum perturbation growth rate $\alpha/(U/l)$ of 0.5 where the growth rate α has been nondimensionalized by the velocity scale divided by the length scale. For a 5 cm/sec amplitude wave with a 50 km length scale, the growth rate corresponds to a 20 day e-folding time. If we assume the amplitudes of two waves are infinitesimal and the third wave is order 1, then the modulus γ becomes small and the interaction resembles a stability problem for the third wave with a growth rate of $2\pi/T_0$. The growth rate

depends linearly on the amplitude a_{3_0} . For the perturbation expansion to be valid the interaction time must be long compared to the wave period, but we will compute an estimate from IV.1.60 when $R_0/\delta \rightarrow 1$. The maximum growth rate $\frac{2\pi\lambda}{U\tau_0}$ for triads involving a 200 km wavelength barotropic wave is $2.2 R_0 a_{3_0} \cos \phi_0$ for $Y^2 = 0$. Assuming $a_{3_0} \cos \phi_0$ is unity and 5 cm/sec velocity scale and 50 km length scale, the growth rate corresponds to a 45 day e-folding time. Hence, in the finite amplitude limit, we expect considerable energy exchange between waves over time scales comparable to wave periods.

Nonlinear interactions between modes are a possible mechanism for coupling waves and modifying the vertical structure. While the weak nonlinear resonant interaction theory is not strictly valid in the MODE region parameter range where $R_0/\delta \sim 0(1)$ to $0(\delta^{1/2})$ we can use the theory as a guide to the effects of nonlinearity. In the weakly nonlinear regime, the waves interact over many wave periods without change in vertical structure. In the strongly nonlinear regime, the interaction time becomes comparable to the free wave period. The strongly nonlinear waves will combine to give a vertical structure which will be a combination of the linear modes on the average. Westward propagation of the strongly nonlinear waves is still expected, but the dominant time scale is not limited by the free baroclinic wave period. In addition, in the strongly

nonlinear regime, the forced wave solutions to the vorticity equation are the same order as the interacting modes and do not obey the free wave dispersion relation. No energy exchange is possible between long barotropic waves and baroclinic waves in the weakly nonlinear regime - a prediction that may be observable in a larger scale experiment.

IV.2 Numerical models of the large scale development of the mesoscale flow

While quasigeostrophic vorticity waves provide a powerful dynamic concept for the description of mesoscale eddies and some of the properties of the MODE-I eddy are wavelike, such as the length scales and phase speeds, a consistent scaling of the vorticity equation for the MODE region suggests that the nonlinear terms are important. Weakly nonlinear flow can be described analytically as in the previous section. However, for highly nonlinear flows we must look at the results of numerical models. The numerical models may be divided into two general classes, the eddy resolving global models, attempting to determine the role and structure of eddies in ocean general circulation models, and the process models, investigating the eddy dynamics without realistic boundary constraints. In particular, we shall discuss one class of process models, a series of eddy spindown experiments by Rhines (1975, 1976) looking at the evolution in space and time of an existing eddy field. For oceanic energy levels, the energy may travel faster through wavenumber space than physical space, in the

sense that significant horizontal and vertical eddy-eddy interactions can occur before the eddies have propagated over a distance comparable to the length scale. Because the spindown experiments appear to reach a quasisteady statistical equilibrium, the model results may be indicative of the characteristics of fully developed flow in the mid-ocean.

The eddy fields in the process models evolve through nonlinear cascades of vorticity and energy. For initially barotropic eddies with sufficient amplitude in a domain without topography, the enstrophy (squared vorticity) cascades to small scales where it is eventually dissipated and the energy cascades towards larger scales. As the scale increases the relative effect of β increases and the cascade will eventually be cutoff by the propagation of nonlinear Rossby waves with wavenumber $k_\beta = (\beta/2U)$. For the MODE region energy levels, the corresponding length scale is 70 to 100 km. As the scale increases, a zonal anisotropy of the flow develops with the zonal kinetic energy exceeding the meridional kinetic energy.

For baroclinic eddies, the direction of the energy cascade depends upon the magnitude of the initial wavenumber k compared to the internal deformation radius wavenumber k_p . If $k > k_p$, then the energy cascades towards larger scale. As the horizontal scale increases, the vertical scale also increases. At the deformation radius, the eddies occlude to form equivalent barotropic eddies. For equivalent

barotropic eddies, the kinetic energy may vary with depth, but the horizontal variation of the streamfunction does not vary with depth. The equivalent barotropic eddies then cascade towards larger scale as in two dimensional turbulence (barotropic cascade mechanism). If $k < k_p$, then the energy cascades towards smaller scale. At the deformation radius the vertical interactions begin the occlusion process. In both cases, the enstrophy cascades towards smaller scales. The enstrophy cascade is cutoff by the propagation of baroclinic Rossby waves with wavenumber k_p .

Kim (1975) has given a possible mechanism for the transfer of baroclinic energy to barotropic at the deformation radius where occlusion occurs in the process models. Baroclinic Rossby waves are unstable with the growing perturbations in both the baroclinic and barotropic modes. Thus the instability of a baroclinic Rossby wave acts as a vertical interaction transferring baroclinic energy into barotropic.

From the process models, we expect that in fully developed flow the barotropic energy will exceed the baroclinic and the zonal kinetic energy will exceed the meridional in the absence of bottom topography. However, the end state of the cascade process is not certain. Bretherton and Haidvogel (1976) found that when the energy dissipation is negligible, two dimensional turbulence cascades to a minimum enstrophy state corresponding

to anisotropic flow along geostrophic contours, but when the energy dissipation and enstrophy dissipation rates are comparable, the flow does not evolve towards larger scale. Topography acts to prevent the occlusion of baroclinic eddies and the development of a state of barotropy. Owens (1975) observed that as the energy levels increase the deep flow becomes locked to the topography.

The process models indicate that the evolution of an eddy field is a complicated competition of several effects, the cascade and dissipation of both energy and enstrophy, the propagation of Rossby waves and bottom topography. In addition, in the models energy propagates very slowly from regions of high eddy energy to regions of low eddy energy. This result is important when considering the generation of eddies in the large scale numerical models, the eddy resolving general circulation models such as Holland and Lin (1975). The mesoscale eddies are generated by barotropic and baroclinic instability of the boundary currents and by baroclinic instability of the westward return flow. Because energy propagates very slowly if the eddy energy dissipation is significant, then the eddy energy must be advected into regions such as the MODE area where it is observed, but not generated.

So far we have discussed the evolution towards large scales of the flow. Charney (1971) predicts a high wavenumber

region in three dimensional quasigeostrophic flow where the pseudo-potential vorticity and energy are conserved while enstrophy cascades to small scales. For geostrophic turbulence, the wavenumber spectrum scales with wavenumber as k^{-3} . The zonal kinetic energy, meridional kinetic energy and potential energy are all equal and scale with depth in the WKB sense.

IV.3 Summary and discussion

In this chapter, we have discussed briefly some possible dynamical mechanisms for the mesoscale circulation. At first, we considered linear quasigeostrophic waves. For a given length scale, the time scales and vertical structure of baroclinic and barotropic Rossby waves are quite distinct suggesting that a wave description may be a useful first attempt at modeling the flow in the MODE region. Even in highly nonlinear flow, wavelike characteristics can be observed. The propagation of Rossby waves is crucial to the evolution of an eddy field in the process models. However, nonlinear eddy-eddy interactions can occur over time and length scales small compared to linear wave scales making a linear description of the eddy field dynamically suspect.

The process models for the evolution of an existing eddy field suggest several features to be present in fully developed flow. When topographic effects are small and

energy dissipation negligible, large scale zonally anisotropic eddies develop. If the enstrophy cascade mechanism is dominant we should expect high vertical coherence and large horizontal scales with most of the energy in the zonal kinetic energy. However, if the energy dissipation is significant or the topography strong, no large scale flow will develop.

V. Relationship of the Observations to Possible Dynamical Mechanisms

Previously, we discussed two possible dynamical mechanisms, linear and weakly nonlinear quasigeostrophic waves and nonlinear cascades of energy and enstrophy, to generate the observed spectra and scales in the MODE region. Now, we want to compare the velocity and temperature observations during MODE with the results of models of the possible dynamics of the meso-scale flow. First, we shall describe the velocity and temperature vertical structure in terms of linear wave modes. The inability of linear waves to describe the vertical structure and the length and time scales of the flow leads us to consider the effects of nonlinear energy and vorticity exchanges.

From the wave models and comparison to the numerical models we infer the importance of nonlinearity on the mesoscale flow. Following Bryden (1975), we shall estimate the horizontal advection of density at the central site mooring. The advective terms are dominant in the deep water where a significant zonal heat flux is observed.

V.1 Wave models

As a first attempt to describe dynamically the MODE observations, linear waves represent a simple model. For the MODE region parameter range we do not expect the mesoscale flow to be linear and correspondingly we expect a linear model to fail. However, in the numerical models, some linear

wave-like behavior is observed even in highly nonlinear flows. Thus, it is interesting to see where the linear model fails.

Since the linear, flat-bottomed Rossby wave normal modes form a complete set, the low frequency density and velocity fields may be expanded uniquely in a series of the modes. The actual observations are noisy and discretely sampled in space. Thus, we shall estimate the normal mode expansion in a least squares sense, minimizing the mean square residual of the expansion and the observed fields. The vertical scales of the temperature and velocity are large, comparable to the depth of the ocean, for the dominant mesoscale motions and we shall confine our attention to low mode numbers.

In this section we shall describe the vertical structure of the temperature during MODE-I and the site mooring velocity and temperature observations in terms of quasigeostrophic wave modes. Then, we shall compare the observed coherence of the model amplitudes with that expected for linear waves. We note initially that the observed length and time scales do not fit the linear dispersion relation. It is suggested, without proof, that nonlinear interactions may be responsible for the distortion of the vertical structure and length and time scales from those of linear waves.

V.1.1 MODE-I

During MODE-I the temperature vertical structure on 15 moorings was obtained. The number of instrumented levels with

temperature records varied from 4 to 12, with at least one instrument in the main thermocline and one instrument in the deep water. The linear theory used to compute the normal modes applied to the density fluctuations and not the temperature. In Appendix A.2 the question of using temperature alone to represent the density field is addressed. Using the mean θ -S relationship in the MODE region the potential density fluctuations can be calculated from the temperature alone to within 5% accuracy. To compute the potential density the pressure at the depth of the instrument must be known. For the temperature/pressure recorders the pressure was measured directly (Wunsch and Dahlen, 1972) and for the current meter temperature measurements the pressure was obtained by interpolation as discussed in Appendix A.1.

The displacement of the density field is given by

$$\eta = \rho'(T, P; S) / \bar{\rho}_z \quad (\text{V.1.1})$$

where $\rho'(T, P; S)$ is the potential density fluctuation about the time mean calculated from the observed temperature and mean θ -S curve and $\bar{\rho}_z$ is the mean potential density gradient. For each mooring the displacement is least squares fit to the first three vertical velocity modes, such that

$$\xi = \left[\sum_{j=1}^N (\eta(z_j, t) - \sum_n a_n(t) W_n(z_j))^2 \right] = \min \quad (\text{V.1.2})$$

The resultant time series of the modal amplitudes for mooring

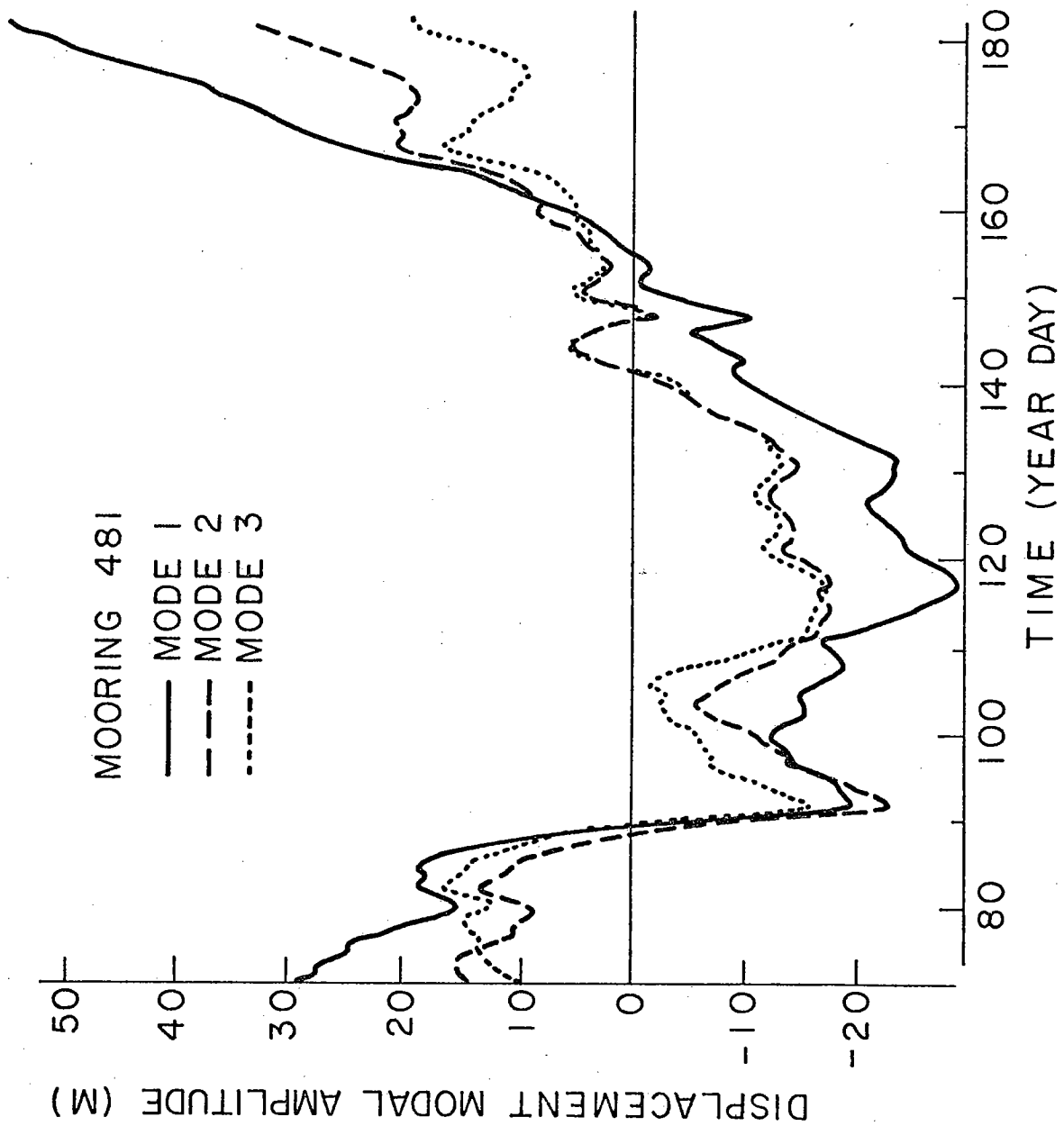


Figure V.1: Displacement modal amplitudes at central mooring (481) during MODE-I

Percentage of variance in 3 mode fit					
Mooring	Total Mode	First Mode	Second Mode	Third Mode	Average Potential Energy (ergs/gm)
1 (481)	87.5%	62.0%	23.7%	14.3%	24.0
3 (499)	93.5	74.6	19.8	5.6	5.0
4 (498)	86.1	92.7	3.5	3.8	15.7
5 (494)	82.7	52.0	29.2	18.8	21.4
6 (493)	95.3	67.4	20.7	11.8	10.2
7 (501)	96.1	40.8	33.6	25.6	11.6
8 (482)	94.7	82.8	13.4	3.8	24.1
9 (497)	87.1	75.7	15.4	8.9	10.8
10 (495)	99.1	7.8	41.7	50.5	2.4
11 (485)	74.6	60.4	18.9	20.7	2.6
12 (486)	98.7	70.6	4.6	24.8	6.2
13 (488)	95.8	72.4	16.9	10.7	18.2
14 (489)	90.8	47.6	22.3	30.1	4.7
15 (483)	83.6	26.7	29.5	43.8	5.4
16 (484)	98.5	56.8	31.5	11.7	7.3
Total	89.6	65.6	20.2	14.2	

Table V.1: Percentage of the total displacement variance described by a three mode fit and relative energies in each density displacement mode

481 (the central mooring instrumented at the most levels) are shown in Figure V.1. The least squares fit describes 88% of the total variance in the displacement fields at the mooring with 62% of the total potential energy in the first baroclinic mode. For the 15 moorings considered (mooring 2 was struck by a towed instrument package part of the way through the experiment and the instrument depths changed as the mooring was stretched) 90% of the variance could be described by the three mode fit with 66% in the first mode. Table V.1 contains the variance and potential energy statistics for each mooring. The worst modal description occurs at mooring 11 where only 75% of the variance is described by the three mode fit. At mooring 11 the days of the poorest decomposition occur when the total variance in the displacement field is low. The vertical structure at these times tends to be in the higher modes. When the variance in the displacement field is large, the lowest mode dominates. At four moorings, 7, 10, 14 and 15, less than half the potential energy is in the first mode and at three of the four moorings the total potential energy is low. Only four instruments worked on mooring 10. With only four observations a three mode fit will describe most of the variance, but will be more sensitive to noise in the displacement calculations. The other three moorings are in the northern part of the array and are either to the north of the observed eddy pattern or on the northern fringe with small displacements.

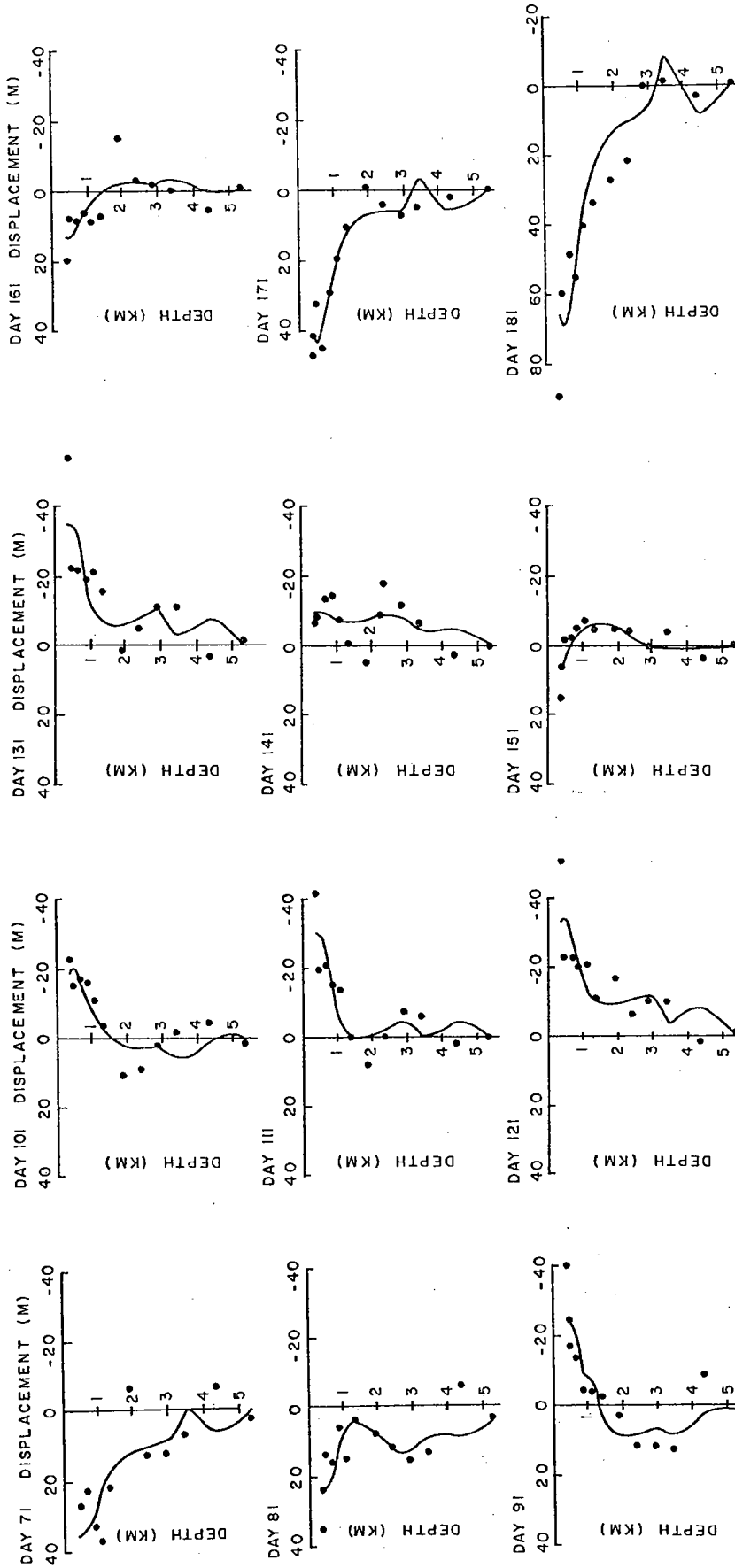


Figure V.2: Displacement (dots) and modal fit (solid line) at central mooring at 10 day intervals during MODE-I

The significance of the results of a given fit will depend on both the ability of the least squares fit to resolve different modes and the energy in the fit compared to the observational noise. Several sources of noise exist. For example, the eddy field is of finite amplitude and may distort the local density profile. The resultant displacement estimate from V.1.1 will then differ from the actual displacement. It is difficult to assess the magnitude of this error. Scarlet (private communication) observed that during MODE-I the density field in the main thermocline was often displaced vertically without distortion. For typical MODE-I displacements the maximum error in estimating the displacement from the temperature is approximately 20%. Also, to resolve a given mode requires a sensor in each lobe of the displacement profile for the mode. For the instrument distribution during MODE-I, only the first three modes can be resolved (see Figure IV.2).

For visual comparison, the observed displacement at mooring 481 and the three mode fit are displayed at 10 day intervals in Figure V.2. While the first mode dominates the displacement decomposition, there is little visual similarity between the observed profiles, generally dominated by the main thermocline, and the first dynamical mode with a maximum at 1300 m. We noted earlier that most of the energy in the displacement field may be described by a mode with maximum displacement in the main thermocline (see Figure II.14). To describe this systematic deviation from a linear first baroclinic mode requires a coupled set of wave modes. As we

found in the previous chapter, nonlinear interactions are a possible mechanism to couple wave modes. However, it is equally possible that free wave modes are dynamically too simple to describe the structure.

Setting aside the question of the significance of the deviations of the vertical structure from free wave modes, we shall use linear waves to describe the gross characteristics of the MODE-I displacement field. The horizontal variation of the first baroclinic mode is similar to that of the thermocline as described in Chapter II with horizontal wavelength of 350 km moving westward at 2 to 3 km/day. One obvious objection to a free wave model is the difference between the baroclinic wave periods and the time scales of the eddy motion. The eddy potential energy in the main thermocline is dominated by 120 day periods which is less than the 155 day minimum period for a first baroclinic mode wave and 487 day minimum period for a third mode.

McWilliams and Flierl (1976), hereafter designated MF, have calculated a number of least squares fits of barotropic and baroclinic Rossby waves to various parts of the MODE-I velocity and temperature data. To obtain closed synoptic patterns resembling the objective maps, MF used two discrete barotropic and two first mode baroclinic waves. We can compare only with the baroclinic calculations. MF consider only temperature and density measurements above 2000 m and thus are describing just the main thermocline. In all

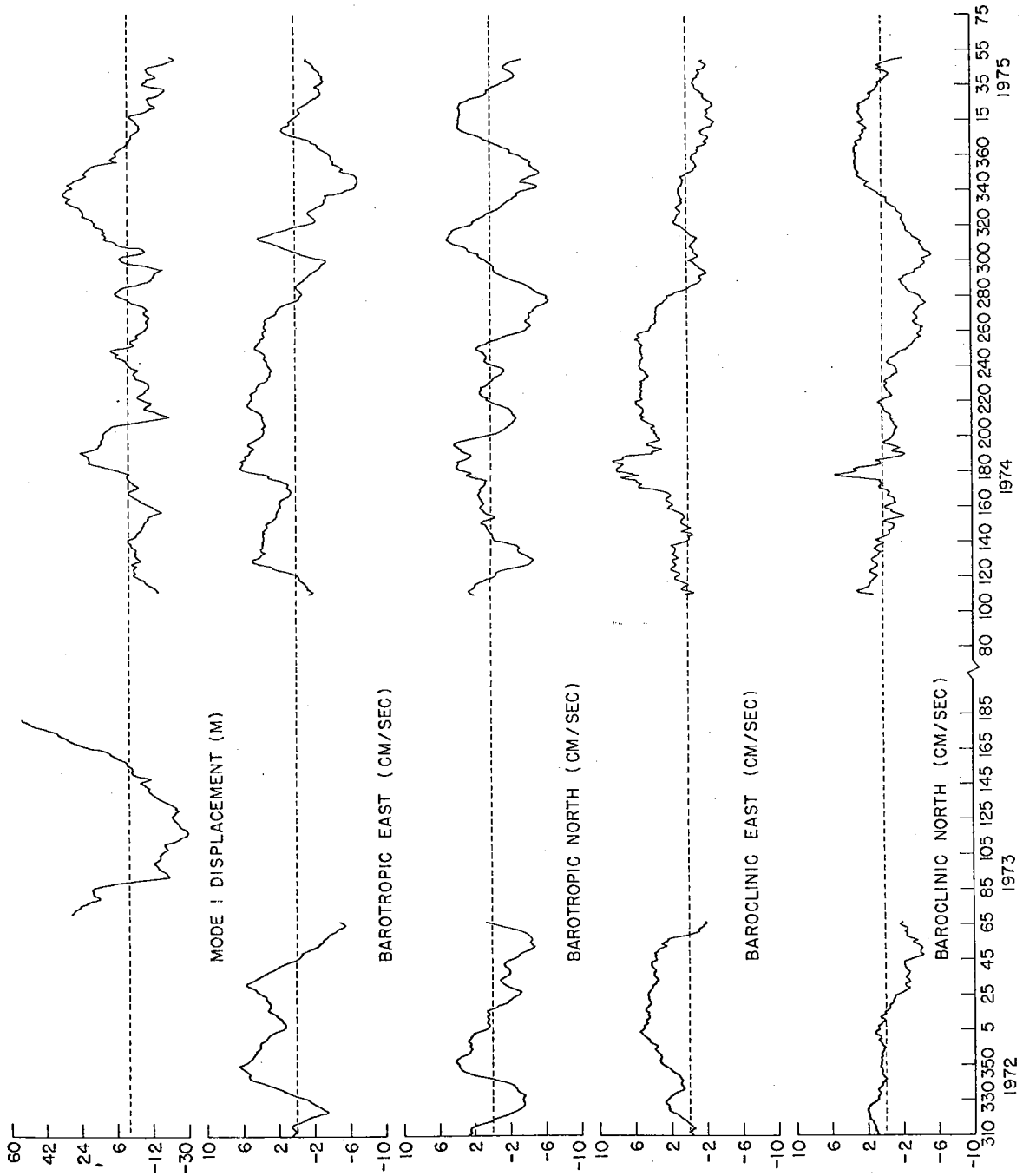


Figure V.3: Barotropic and first baroclinic velocity
and displacement at MODE Center

baroclinic cases, the dominant wave has approximately 300 km wavelength and 2 km/day phase propagation consistent with observed wavenumber spectrum in the main thermocline. However, they find that only 40% of the total variance may be ascribed to their two waves. The ability of the wave fits to describe the gross, albeit not very well defined, characteristics of MODE-I does not imply that linear dynamics govern the fields. Killworth and Anderson (1975c) point out that similar quality wave fits may be obtained to the data with drastically different physics.

In the deep water, not considered by MF, small spatial scale motions are associated with small time scales. High mode baroclinic fluctuations are required to describe the small vertical scales. However, the minimum wave periods increase with mode number and are long compared to the duration of MODE-I. Thus, a linear wave model cannot describe the deep water fluctuations, either.

V.1.2 Site mooring observations

Statistics of the modal amplitudes for times on the order of the linear wave periods may be obtained from the site mooring velocity and temperature records. Velocity data are available at only three depths. Hence, we can estimate only the barotropic and first baroclinic modal amplitudes using a least squares fit. The resultant amplitude time series of the first mode displacement and the barotropic and baroclinic velocity components at MODE Center are shown in Figure V.3.

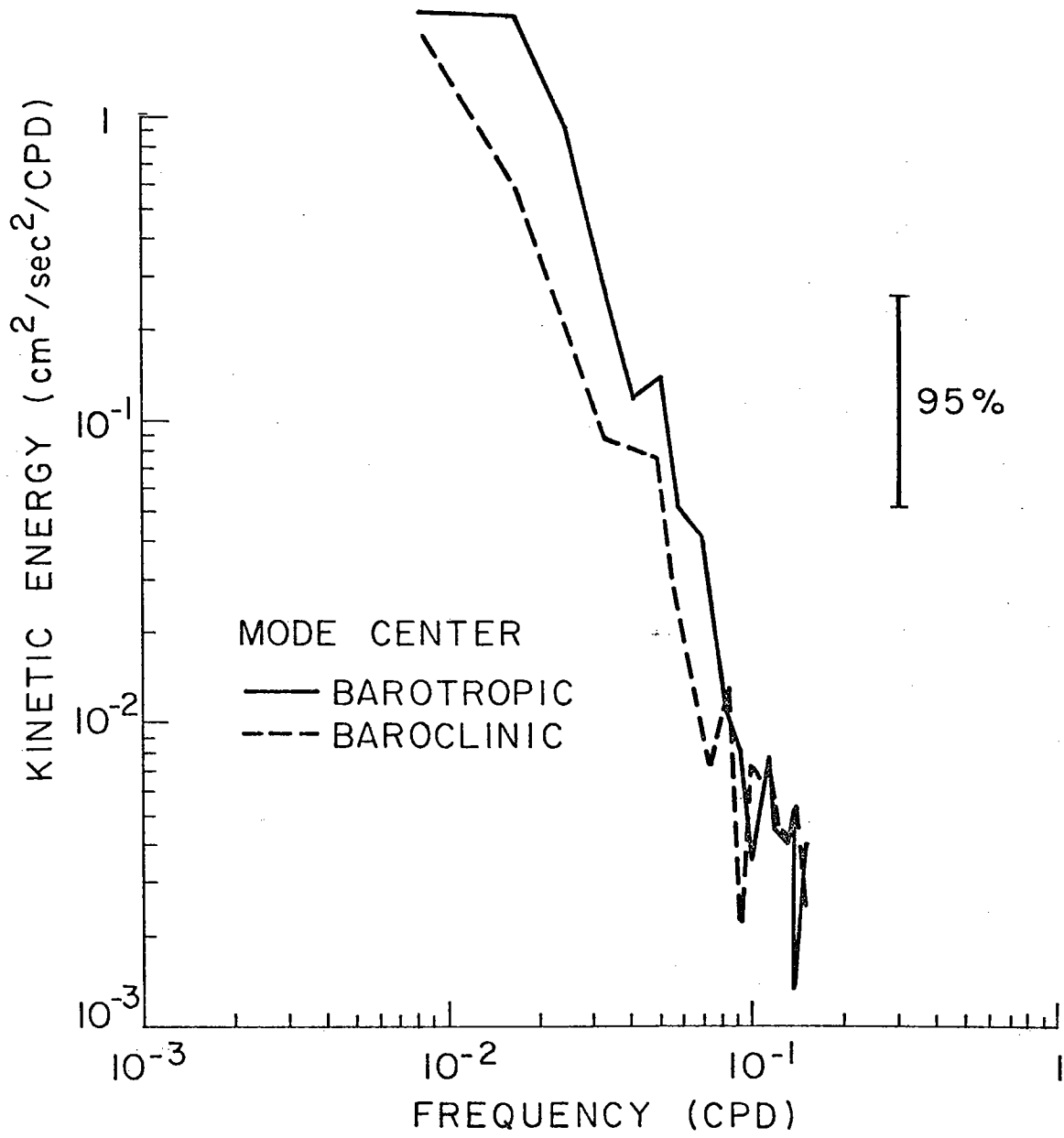


Figure V.4: Barotropic and first baroclinic kinetic energy spectra at MODE Center

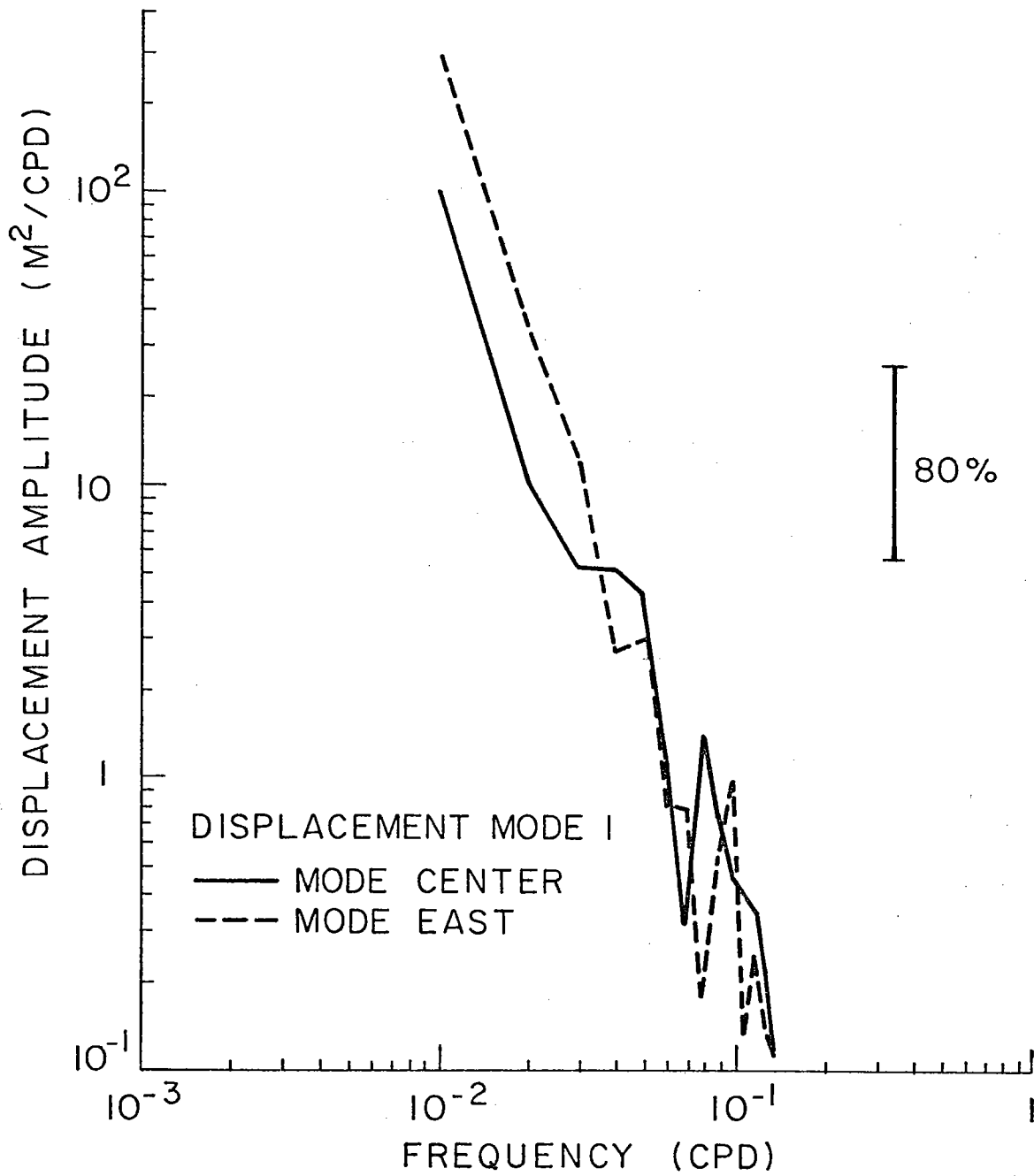


Figure V.5: First baroclinic mode displacement spectra at site moorings

Visually, the barotropic velocity has a shorter time scale and slightly larger amplitude than the baroclinic velocity. The kinetic energy spectra in Figure V.4 reflect this observation with the barotropic energy greater than the baroclinic at low frequencies (although the difference is not statistically significant at 95% confidence) and the barotropic energy peaking at 60 days while the baroclinic spectrum is red. The barotropic mode dominates at the 1500 m level where the kinetic energy is contained in a peak between 50 and 120 days, indicating shorter barotropic time scales than obtained by MF. In their wave decomposition, MF find the baroclinic motions dominating with the ratio of baroclinic to barotropic energy of approximately 1.5. The observed ratio from the site moorings is 0.85, which is not as barotropic as the process model simulations of the MODE region (Owens, 1975) where the ratio is 0.5. First mode displacement spectra at both MODE Center and MODE East are red to 100 day periods and indistinguishable at 90% confidence.

If the velocity and displacement fields are a superposition of linear, independent waves, then the coherences between the modal amplitudes at a given frequency may be computed as an energy weighted integral over wavenumbers given by

$$\text{coh}(UD) = -i \left\langle \frac{\int d\mathbf{k} \ell \mathcal{P} \mathcal{Q}_z e^{i2\mathbf{k}\cdot\mathbf{x}}}{\left[\int d\mathbf{k} \ell^2 \mathcal{P}^2 e^{i2\mathbf{k}\cdot\mathbf{x}} \right]^{1/2} \left[\int d\mathbf{k} \mathcal{Q}_z^2 e^{i2\mathbf{k}\cdot\mathbf{x}} \right]^{1/2}} \right\rangle \quad (\text{V.1.3})$$

$$\text{coh}(\bar{V}D) = i \left\langle \frac{\int d\bar{k} k \bar{\rho} \bar{\rho}_z e^{i2\bar{k}\cdot\bar{x}}}{[\int d\bar{k} k^2 \bar{\rho}^2 e^{i2\bar{k}\cdot\bar{x}}]^{1/2} [\int d\bar{k} \bar{\rho}_z^2 e^{i2\bar{k}\cdot\bar{x}}]^{1/2}} \right\rangle \quad (\text{V.1.4})$$

$$\text{coh}(UV) = \left\langle \frac{\int d\bar{k} k \lambda \bar{\rho}^2 e^{i2\bar{k}\cdot\bar{x}}}{[\int d\bar{k} k^2 \bar{\rho}^2 e^{i2\bar{k}\cdot\bar{x}}]^{1/2} [\int d\bar{k} \lambda^2 \bar{\rho}^2 e^{i2\bar{k}\cdot\bar{x}}]^{1/2}} \right\rangle \quad (\text{V.1.5})$$

where U is the zonal velocity, k the zonal wavenumber, V the meridional velocity, λ the meridional wavenumber, D the displacement and $\langle \rangle$ denotes averaging over frequency.

Since Rossby waves must propagate westward, the contributions to the integral of the meridional baroclinic velocity and the first mode displacement from each wave would be of the same sign. Thus we expect significant coherence at 90° phase between the meridional baroclinic velocity and the displacement. The phase difference arises because the displacement is proportional to $\bar{\rho}_z$ (the vertical derivative of the pressure streamfunction in phase with the pressure) and the velocity is proportional to the horizontal derivative of the streamfunction and 90° out of phase with the pressure. For the coherence between the two baroclinic velocity components and the coherence between the displacement and the zonal baroclinic velocity, the values will be determined by the meridional

		Baroclinic			Barotropic
		D	U	V	U
Baroclinic	U	(-126°) 0.42			
	V	(118°) 0.76	(-138°) 0.87		
Barotropic	U	(-153°) 0.32	(11°) 0.99	(126°) 0.80	
	V	(152°) 0.94	(-102°) 0.65	(30°) 0.93	(-86°) 0.53

a) Coherence (phase) for 150 to 300 day periods

		Baroclinic			Barotropic
		D	U	V	U
Baroclinic	U	(26°) 0.78			
	V	(88°) 0.93	(67°) 0.52		
Barotropic	U	(-126°) 0.75	(-118°) 0.36	(143°) 0.88	
	V	(-80°) 0.59	(-98°) 0.92	(165°) 0.36	(-31°) 0.34

b) Coherence (phase) for 75 to 150 day periods

Baroclinic		Barotropic	
D	U	V	U
(-99°)			
0.98			
(-91°)	(5°)		
0.75	0.78		
(-57°)	(52°)	(109°)	
0.40	0.53	0.30	
(-9°)	(86°)	(147°)	(26°)
0.58	0.60	0.19	0.68

c) Coherence (phase) for 43 to 75 day periods

Baroclinic		Barotropic	
D	U	V	U
(-74°)			
0.17			
(118°)	(-43°)		
0.72	0.49		
(-4°)	(55°)	(107°)	
0.34	0.95	0.24	
(38°)	(99°)	(156°)	(44°)
0.36	0.94	0.22	0.99

d) Coherence (phase) for 30 to 43 day periods

Table V.2: Coherences and phases between baroclinic displacement and velocity components and barotropic velocity components for 4 frequency bands

wavenumber spectrum. If the baroclinic wavenumber spectrum is dominated by a peak in one quadrant, then the contributions to the integrals will be of the same sign and the coherence significant. The expected coherences for the waves given by the MF fit are: 0.9 with displacement leading the meridional baroclinic velocity by 90° , 0.8 with the displacement leading the zonal velocity by 90° and 0.8 with the velocity components 180° out of phase. In Table V.2, the observed modal coherences are listed for 300 day times series averaged over three frequency bands. The MF fit waves would be included in the lowest frequency estimate. While the observed coherences are not consistent with the MF model, significant coherences at 90% confidence exists between the zonal and meridional velocities with phase indistinguishable from 180° . At 80% confidence, the displacement leads the meridional velocity with phase indistinguishable from 180° . At 80% confidence, the displacement leads the meridional velocity with phase indistinguishable from 90° . The lack of significant coherence between the displacement and the zonal velocity suggests that at low zonal wavenumbers the energy is evenly divided between positive and negative meridional wavenumbers, since the integral in V.1.3 is sensitive to the sign of the meridional wavenumber.

The most significant coherences in the lowest frequency band in Table V.2 represent a coupling between the baroclinic and barotropic modes; the zonal velocity components and the meridional velocity components are coherent with small phase.

A consistent coupling between barotropic and baroclinic waves over several wave periods at a single location cannot occur for linear waves. The difference in the dispersion of baroclinic and barotropic waves will cause a drift in the relative phases of the waves with time. Either the vertical structure of the mesoscale motions is intrinsically different from the linear dynamical modes or a nonlinear exchange between modes causes a coupling.

At higher frequencies the pattern of coherences is more complicated. For periods of 75 to 150 days, the meridional velocity is coherent with the displacement at 90° phase, while the zonal velocity is significantly coherent with the displacement only at 80% confidence. A cross coupling between the baroclinic zonal and barotropic meridional velocity and vice versa exists. From 43 to 75 day periods, the zonal velocity leads the displacement implying dominantly negative meridional wavenumbers while at 80% confidence the meridional velocity leads the displacement implying eastward zonal wavenumbers. At these higher frequencies, free baroclinic waves cannot exist. It is not possible to use linear waves to describe these fluctuations.

V.1.3 Summary and discussion

The mesoscale flow in the MODE region cannot be described in terms of linear waves. This result is not surprising since we do not expect the flow in the MODE region to be linear and the observed length and time scales do not fit the dispersion relation. The observed vertical structure of both the

velocity and temperature field is systematically different from the linear wave modes. Nonlinear interactions can cause a coupling of wave modes to modify the vertical structure. In the process models, nonlinear energy exchanges determine the character of the mesoscale flow. We shall compare the observed fields with the results of the process models in the next section. Linear waves cannot describe the small length and time scales in the deep water. The association of small length and time scales resembles turbulence rather than waves, indicating the probable importance of nonlinearity in the deep water.

V.2 Comparison to numerical models

In the process models, the large scale development of the flow by nonlinear cascades depends crucially on the nature of the energy and enstrophy transfers. While we cannot estimate directly the energy and enstrophy cascade rates in the MODE region, we can look for features in the flow observed in the numerical models.

In the absence of topography, if the energy dissipation is small and the enstrophy cascades to small scale where it is dissipated, an occluded field of anisotropic eddies develops. For periods greater than 200 days in the MODE region, the zonal kinetic energy exceeds the meridional kinetic energy with insignificant vertical phase variation of the velocity, consistent with the development of an equivalent barotropic state in the model. While it is not possible to resolve the

wavenumber structure of the very low frequency flow, the zonal anisotropy is suggestive of large horizontal scales, perhaps on the order of $k\beta^{-1}$ (70 to 100 km). The apparent development of anisotropic, large scale, equivalent barotropic eddies is not sufficient to indicate negligible energy dissipation, although, as we shall observe later, this assumption may be reasonable.

Topography can prevent the evolution of an existing eddy field to a barotropic state in the models. Topographic influences are evident in the deep flow over the abyssal hills. At the eastern site mooring, the mean and eddy flow are generally along geostrophic contours. In the eddy energy containing band of 80 to 120 days, the meridional kinetic energy generally dominates, not the zonal, and significant energy variations are observed over 100 km. The energetically dominant eddies in the deep water are not consistent with the barotropic large scale flow of the models.

At high frequencies, the variation of the energy in the WKB sense and even partition of energy between the zonal kinetic, meridional kinetic, and potential energy is suggestive of geostrophic turbulence. Geostrophic turbulence theory predicts a k^{-3} wavenumber spectrum for small vertical and horizontal scales. We can determine only the frequency spectra of the motions. However, in the deep water small time scales appear to be associated with small length scales. For small length scales the effect of β will be small and we might expect an advective time scale associated with these length

scales. If the small scales are passively advected by the large scale flow, a frozen field model, then the frequency spectra would vary as ω^{-3} , indistinguishable from the observed spectra. For typical main thermocline speeds, the length scale predicted from the advective time scale would be 20 to 30 km. At the high frequencies, the actual scale determination is equivocal. For an isotropic field, a lack of coherence does not indicate a short scale. In geostrophic turbulence, energy and pseudo-potential vorticity are conserved while enstrophy cascades to small scales. Thus, the high frequency spectral similarity is consistent with negligible energy dissipation.

Thus, while the numerical models are suggestive of several features of the flow in the MODE region, a consistent description of the flow cannot be obtained from a simple application of the results of the models. Within the MODE region, we should not expect the distribution of the relative effects of energy and enstrophy dissipation and topography to be constant. Hence, even if the cascade mechanism is dynamically valid, variations in the development of the flow, in both space and frequency, will occur.

V.3 Horizontal advection of heat

In the previous sections, we have suggested that the mesoscale flow is highly nonlinear, but we have not made any direct estimates of the local dynamical balances. Bryden (1975) has shown that, in the quasigeostrophic limit, two terms of the thermal balance of the ocean, the time rate of

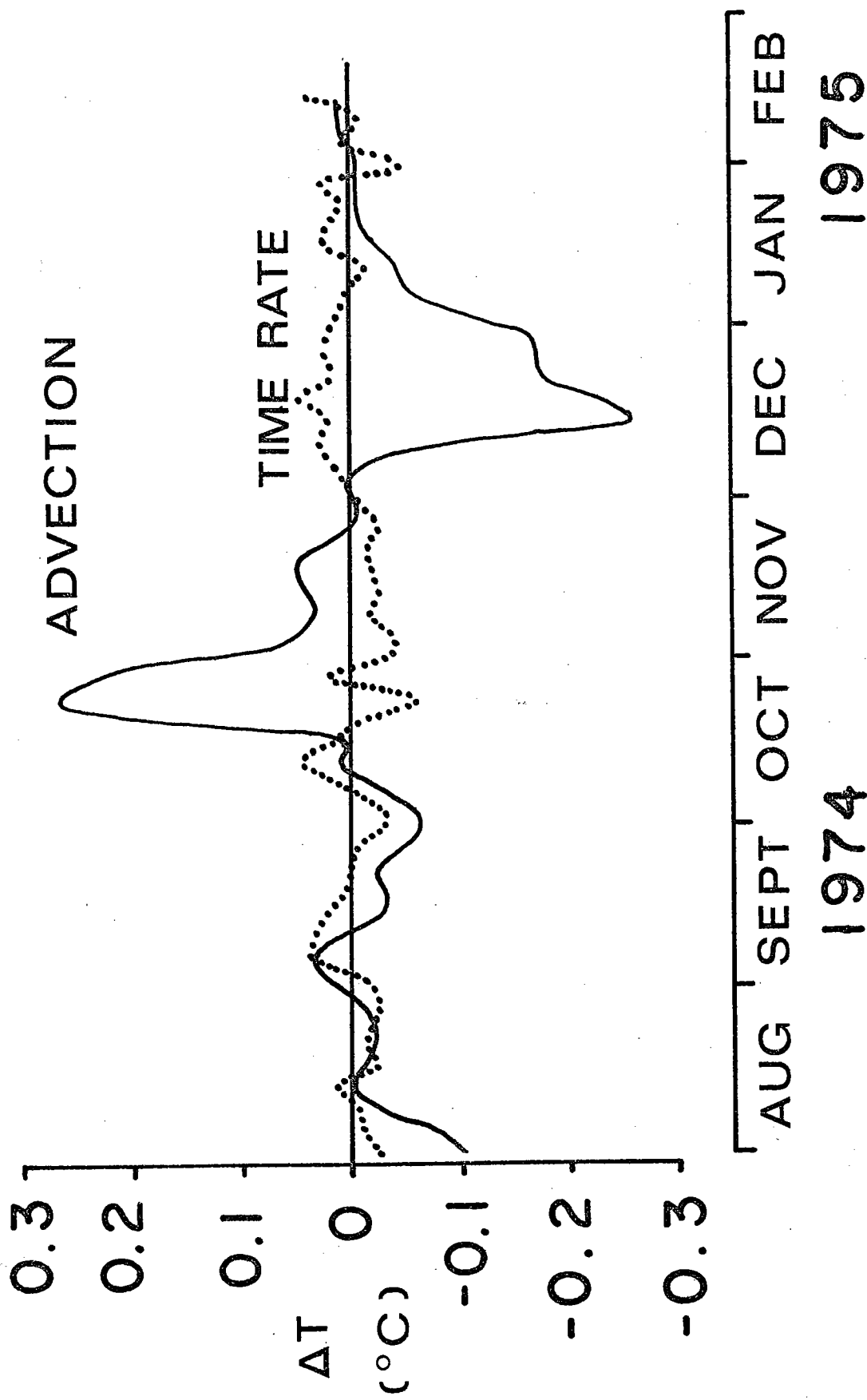


Figure V.6: Time rate of change and horizontal advection
(times minus one) of heat at MODE Center

change of heat and the horizontal advection, may be estimated from the measurements on a single mooring. Assuming thermal wind balance between the temperature (actually the density, but a tight Θ - S correlation is assumed also) and velocity, the advective terms may be estimated from the vertical derivative of the current direction ϕ and the current speed S

$$u T_x + v T_y = \frac{\rho_o f}{g \alpha} S^2 \frac{\partial \phi}{\partial z} \quad (\text{V.3.1})$$

where the estimated error is of the order of the Rossby number.

Bryden found that for 40 days in the MODE region the thermal balance is predominantly advective with the time rate of the change nearly balanced by the horizontal advection. Using velocity and temperature data from MODE Center, we shall estimate the vertically integrated thermal balance between 500 m and 4000 m for 206 days, a time longer than the dominant eddy time scale. The estimated error from the trapezoidal integration over the coarse instrument spacing is about 25% for both the advective and time rate of change terms. The thermal balance is highly nonlinear with the two terms of the balance shown in Figure V.6. An advective event of approximately 80 days duration dominates the balance. The advective event is associated with a 50 m thermocline elevation between day 290 in 1974 and day 15 in 1975 (see Figure I.2a). At the same time, the initially south-westerly flow in the thermocline changing to north-westerly is consistent with the westward drift of a cyclonic eddy past the mooring. However, the flow below the thermocline is generally at right angles to the thermocline flow

with a visually shorter time scale. Thus, the observed veering of the velocity, which is responsible for the large heat advection, occurs between the deep water and the main thermocline. During the event, the horizontal advection exceeds the time rate of change by factors as great as 5.

During the event, the deep water flow appears coherent, but there is little coherence between the thermocline and deep water. This coherence distribution is similar to temperature coherence. The temperature variation can be described by two modes. During MODE-I, two isotropic velocity modes described most of the kinetic energy. However, during the event, the deep water and thermocline flow are directed differently and an isotropic model is inappropriate.

Empirical velocity modes

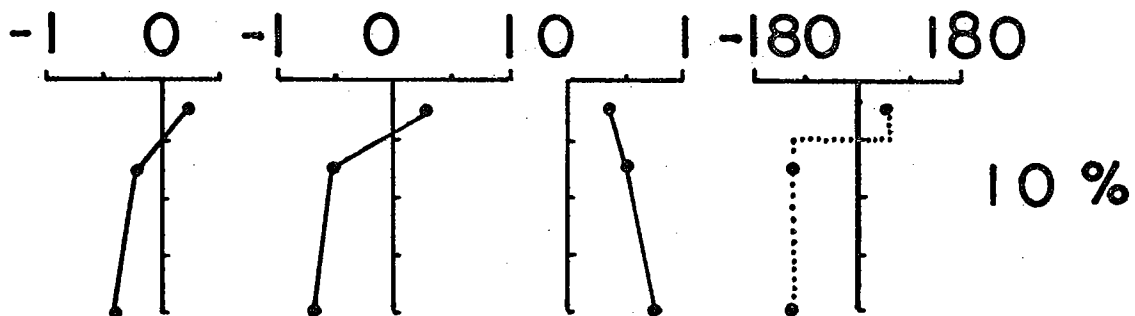
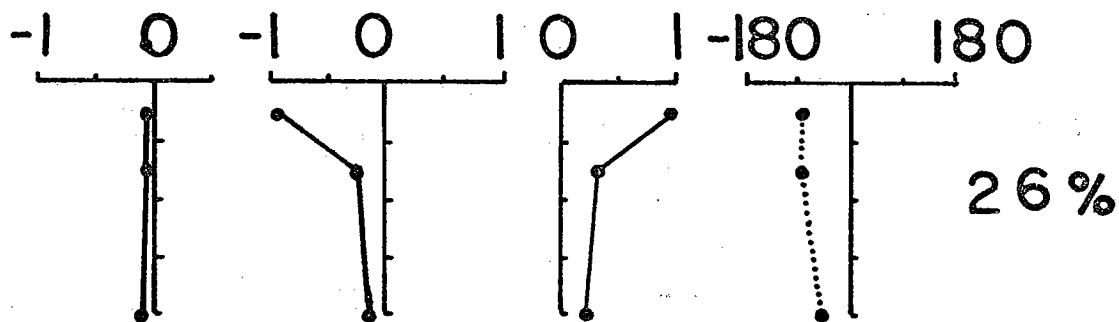
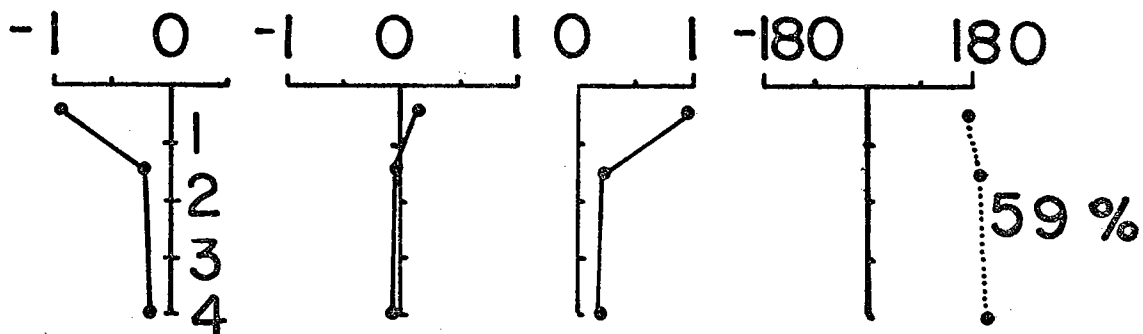
Suppose the velocity is treated as a vector stochastic process, we may use then the technique of empirical orthogonal expansions to obtain the vector velocity vertical structure. The generalization of II.4.4 to a vector process is straight forward, although the notation used is complicated. We seek to expand the velocity in a series of orthogonal modes with uncorrelated amplitudes

$$\underline{v}(z_i; t_j) = \sum_n a_n(t_j) \underline{\chi}_n(z_i) \quad (\text{V.3.2})$$

The empirical modes of a discretely sampled vector process are the solutions to the equation

$$\sum_{k=1}^2 \sum_{i=1}^N B_{ij}^{kl} \underline{\chi}_i^k = \lambda_n \underline{\chi}_j^l \quad (\text{V.3.3})$$

ZONAL MERIDIONAL SPEED DIRECTION



EMPIRICAL VELOCITY MODES

Figure V.7: Empirical vector velocity modes at MQDE Center

where B_{ij}^k is the covariance of $v_k(z_i)$ and $v_k(z_j)$ and χ_i^k is the i th empirical mode of the k th velocity component at the depth z_i . Kundu and Allen (1976) have independently derived a similar vector decomposition by expressing the velocity at a given depth as a complex scalar. The modes are real and orthogonal and the eigenvalues are real and non-negative. The eigenvalues, as in II.4.6, are the expected value of the square of the expansion coefficient and represent the amount of variation described by the mode.

Using velocity data for 300 days at MODE Center, the vector empirical modes are shown in Figure V.7. 95% of the total variance is described by three modes. The first two modes with 59% and 26% of the kinetic energy are predominantly zonal and meridional, respectively. Thus, for 85% of the kinetic energy, the velocity may be described by modes with no vertical direction change and speed profiles resembling the isotropic first empirical mode. For the third mode, the kinetic energy increases in the deep water with the main thermocline and deep water currents out of phase.

Small direction deviations exist from the simple descriptions of the modes given above. The estimated covariance is distributed as χ^2 and the determination of the distributions for the eigenvalues and eigenvectors is complicated. Using theorems from numerical analysis for the well-posedness of the eigenvalue problem, we can estimate the confidence limits (Isaacson and Keller, 1966). If we assume the uncertainty of

the covariance may be expressed as

$$R(\epsilon) = R + \epsilon C \quad (\text{V.3.4})$$

where the matrices R and C , the estimated error, have the same norm, then for any eigenvalue $\lambda(\epsilon)$ for $R(\epsilon)$ we have

$$|\lambda(\epsilon) - \lambda| = O(\epsilon) \quad (\text{V.3.5})$$

where λ is the corresponding eigenvalue of R and similarly the rms difference between the eigenvectors of $R(\epsilon)$ and R is $O(\epsilon)$. While the actual uncertainty in the direction estimate will be a function of the direction as well as ϵ , for $\epsilon \sim 0.1$ the maximum direction deviation would be approximately 20° , a reasonable bound for the expected error of the calculation.

Most of the kinetic energy is described by the first two modes with an equivalent barotropic-type structure, suggestive of the structure predicted by the process models. The third empirical mode with a deep water intensification is associated with the shorter length and time scale motions in the deep water. In the quasigeostrophic limit, if the velocity can be described by a superposition of unidirectional modes with the same vertical speed directions, then there is no horizontal advection associated with the field. For example, suppose the velocity is given by

$$\vec{v}(z, t) = \sum_n a_n(t) \hat{j}(z) \hat{e}_n \quad (\text{V.3.6})$$

then substituting into equation V.3.1 yields no horizontal advection and a linear thermal balance. Now an eddy field composed from the first two empirical modes satisfies equation V.3.6 and would be locally linear. Thus, the observed non-linearity of the thermal balance depends on the presence of modes containing a small fraction of the energy with different vertical structure. In particular, the deep water intensified mode is crucial to the observed horizontal advection of heat in the deep water. In the main thermocline, where the first two modes dominate, little vertical veering of the current occurs. Below the thermocline, the relative importance of the deep water intensified mode increases and the veering, indicative of horizontal advection of heat, occurs.

We may use the estimates of the horizontal advection and time rate of change to consider baroclinic energy transfers between the mean and eddy fields. For a baroclinically unstable field, the horizontal advection of density is of opposite sign from the time rate of change of density and the vertical advection of the mean density gradient (Bryan, 1974). A distinguishing feature of baroclinic instability is the vertical change of phase with depth (Gill, Green, and Simmons, 1974). For a growing disturbance, the phase increases with depth corresponding to the time rate of change leading the horizontal advection. Using this criterion, an energy exchange between the eddy and mean field does not occur during the 200 days record at MODE Center. The correlation of horizontal advection and time rate of change is -0.40 which is significantly

nonzero at 90% confidence, but the maximum correlation occurs at zero phase lag. During the advective event, the time rate of change and the horizontal advection have the same sign, inconsistent with baroclinic instability.

Thus, no evidence for baroclinic instability of the long term mean flow is observed below 500 m in the MODE region. This result is not surprising. The mean flow in the MODE region, except in the deep water over the abyssal hills, is too small to be reliably estimated. The mean available potential energy below 500 m is inadequate to supply the eddy kinetic energy. In the MODE region, the primary energy transfers, if any, are within the mesoscale motion itself. However, Gill, Green, and Simmons have noted that for the baroclinically most unstable disturbance the vertical phase change is confined to the upper 400 m. Thus, we expect the phase lag to be best estimated in near surface waters. At the secondary maximum in the growth curve for the baroclinic instability given by Gill, Green, and Simmons at wavelengths around 250 km the vertical phase change between 500 m and 1500 m is approximately 90° . If the MODE region was actively unstable, at least some disturbances would cause a lag between horizontal advection and time rate of change for observations in the main thermocline. However, no lag is observed indicating that local baroclinic instability of the mean is not an energy source for the eddy field in the MODE region.

V.4 Summary and discussion

A simple first attempt to model the mesoscale motions assumes linear dynamics and expands the motions in terms of quasigeostrophic waves. However, such a simple dynamical model is not adequate to describe the flow. In the main thermocline, westward motion of the eddies is observed, consistent with linear waves, but the dominant length and time scales do not fit the linear dispersion relation. For the observed length scales, the eddy time scales are less than the minimum free wave periods and greater than a purely advective time scale. Much of the kinetic and potential energy in the MODE region is associated with length and time scales where free linear Rossby waves are excluded. In addition, the vertical structure of the velocity and temperature fields differs systematically from the structure of the linear wave modes. The empirical vertical structure of the velocity is dominated by an equivalent barotropic mode which must be represented by a combination of the linear barotropic and first mode baroclinic wave modes. Similarly, the displacement is greatest in the main thermocline rather than at 1300 m as predicted by the linear first baroclinic wave mode.

For the MODE region, we expect the nonlinearity of the flow to be dynamically important. The importance of the advection of heat in the thermal balance has been shown directly. Weak nonlinear interactions between Rossby waves can lead to an apparent coupling of wave modes such as seems to be present in the linear wave models of the mesoscale motions. The devel-

opment of an existing nonlinear eddy field is governed by competition between the effects of energy and vorticity cascades and dissipation, propagation of Rossby waves and topography. Several features of the flow in the MODE region are consistent with the eddy spindown models of Rhines and others. At very low frequencies, an equivalent barotropic zonal flow dominates the motion, consistent with the spindown models when energy dissipation and bottom topography are negligible. The spectral similarity of the high frequency flow regime is possibly consistent with advected geostrophic turbulence indicating a cascade of vorticity to small length scales and negligible energy dissipation. However, the energetically dominant eddies are not consistent with the barotropic large scale flow of the models. In the 80 to 120 day period band, the meridional kinetic energy, not the zonal, generally dominates and significant energy variations occur over eddy length scales.

While the numerical models cannot describe completely the flow in the MODE region, the idea that the flow development depends on the relative effects of energy and enstrophy cascade and dissipation and of topography appears reasonable. Using the horizontal advection and time rate of change of heat in a baroclinic instability model, we observe no apparent interaction between the mean kinetic energy and the eddy energy, suggesting that the eddy energy is neither generated nor dissipated locally. If the spindown models are applicable no energy dissipation can occur. Topography can inhibit the cascade of vorticity to small scales and may be responsible for the eddy scale energy variations.

VI. Conclusions

In the Introduction, we posed four questions about the low frequency motions:

- 1) Can the eddies be characterized statistically?
- 2) What are the dynamics of the eddies?
- 3) What are the sources and sinks of energy?
- and 4) How important are the mesoscale eddies in the energetics of the ocean?

We have begun to answer these questions in this thesis for at least one small region of the western North Atlantic Ocean, the MODE region.

The temporal variability of the low frequency motions may be characterized by three regimes: very low frequencies with periods greater than 200 days, an eddy energy containing band of 80 to 120 day periods, and high frequencies with periods less than 30 days. At very low frequencies, the flow at all depths is anisotropic with the zonal kinetic energy exceeding the meridional. In the thermocline, the very low frequency zonal flow dominates the total kinetic energy. An eddy energy containing band of 80 to 120 day periods provides the greatest contribution to the kinetic and potential energy in the MODE region except for the zonal thermocline flow. The time scale of the MODE-I thermocline eddy is consistent with the existence of this band. Eddy scale kinetic energy variations are confined to this band. At high frequencies, the kinetic and potential energy scale with frequency as $\omega^{-2.5}$ and with depth in the WKB sense.

Energy at high frequencies is partitioned evenly between zonal kinetic, meridional kinetic and potential energy and is homogeneous at all depths over 100 km.

Using the technique of empirical orthogonal expansion, a relatively simple description of most of the low frequency energy may be obtained. Approximately 95% of the kinetic energy may be described by three unidirectional velocity modes. The most energetic mode is an equivalent barotropic zonal flow with vertical shear across the thermocline but in phase currents with depth, while the second mode is a meridional flow with approximately the same vertical structure. Because the time scale of the kinetic energy dominating zonal thermocline flow is long compared to the meridional time scale of 15 to 20 days, the expansion amplitudes of the two modes are uncorrelated. A small portion of the kinetic energy is described by a deep water intensified flow, which is also responsible for the directional veering of the low frequency flow in the deep water. Two modes are required to describe the displacement with the dominant mode having a maximum displacement in the thermocline and in phase displacements with depth, while the second mode has out of phase thermocline and deep water displacements.

The dynamics of the mesoscale eddies are very nonlinear. From a consistent scaling of the equations of motion, we expect the mesoscale flow to be quasigeostrophic and nonlinear. The observed integrated heat balance in the MODE

region is very nonlinear. However, even in highly nonlinear flows, some wavelike characteristics, such as westward propagation, appear. During MODE-I, the thermocline eddy moved westward at 2 to 3 km/day with approximately the internal radius of deformation length scale, but the eddy time scale was less than the minimum linear wave period and greater than a purely advective time scale. The length and time scales of the eddy motion are inconsistent with linear wave motion, indicating the importance of advection in the eddy dynamics. Also, the empirical vertical structure of the eddies is systematically different from the vertical structure of linear wave modes.

We can use the kinematic description of the eddy motion to infer further the possible dynamics of the motion. In eddy spindown experiments, the development of an existing field of eddies depends crucially on the relative effects of cascades and dissipation of energy and enstrophy, propagation of nonlinear Rossby waves and topography. At very low frequencies, the observed flow is similar to the spindown of an eddy over smooth topography with negligible energy dissipation. For the energetically dominant eddies between 80 and 120 day periods, the effects of bottom topography are apparently greater than for lower frequencies with eddy length scale energy variations and the alignment of the deep flow over the abyssal hills with geostrophic contours. The spectrally similar flow regime at high fre-

quencies is possibly consistent with advected geostrophic turbulence, indicating a cascade of vorticity to small length scales and little energy dissipation.

In the global numerical models, the eddy kinetic energy is generated by barotropic and baroclinic instability of strong mean currents and of the westward return flow. Using a baroclinic instability model for the MODE region, no apparent energy exchange between the eddy and mean flows is observed. Thus, the eddy energy is not generated locally. Also, no energy transfer from the eddy field to the mean field occurs. The eddy energy is not dissipated locally into the mean field. Comparisons with the eddy spindown experiments suggest that little local energy dissipation occurs. However, it is possible that the eddy scale energy variations are due to topographic scattering and dissipation in the deep water.

The mesoscale eddies are potentially important in the energetics of the ocean. Schmitz (1976) has suggested that the eddy Reynolds stresses in the deep water may be driving the mean circulation in the Western North Atlantic. In the MODE region, a net zonal eddy heat flux is observed, although the eddy heat transport is small compared to the estimated average annual poleward heat transport. The observed eddy heat transport is not associated with the energetically dominant motions in the MODE region, but with the less energetic small scale motions. The relevance of this observation to the eddy field elsewhere in the ocean is unknown.

The kinematics and energetics of the mesoscale eddies in the MODE region are not necessarily typical of the eddy field in the ocean, nor are the results of this thesis particularly robust statistically. In the main thermocline, the observed time scale is long and the corresponding statistical stability is low. The anisotropy of the very low frequency velocity is described by the trend of the spectra and is not statistically significant at all depths. However, this trend is consistent with a relatively simple dynamical model, the eddy spindown experiments, and thus, is a useful, if not statistically significant, description of the field. Similarly, large scale experiments in progress (POLYMODE) and historical data (Schmitz, et al., 1976) show large spatial variations in the eddy energy levels. From the MODE region, there is a general decrease in eddy kinetic energy to the east and increase to the north and south. Assuming the same eddy time scales, the higher energy regions are more nonlinear and may transport more momentum and heat in the mean. Thus, the MODE data are just a first look at the mesoscale eddies, and a more complete description awaits further observations.

Appendix A Representativeness of Moored Temperature Measurements

Are moored temperature measurements representative of dynamically important variables for the discussion of the kinematics and dynamics of mesoscale motions?

The ocean is thermally stratified in the mean. The temperature measured by a thermistor on a depth varying instrument will record an additional signal induced by the instrument motion. The ocean is also salt stratified. If the temperature and salinity are highly correlated, then the density of seawater may be computed from the temperature only, using the salinity determined from the mean potential temperature-salinity (θ -S) curve. Thus, the relation between the measured temperature and dynamical variables such as density, dynamic height and potential energy is a function of the motion of the temperature sensor and the equation of state of seawater. In this section we shall look at the problem of mooring motion and at the calculation of density from moored temperature measurements only.

A.1 Mooring motion

The design of the mooring affects the measurement of both temperature and velocity. Gould and Sambuco (1975) have reported systematic differences in the kinetic energy levels measured on surface and subsurface moorings. During MODE all the moorings were of subsurface type. Approximately half of the temperature records were obtained from temperature/pressure recorders (Wunsch and Dahlen, 1974). Using the pressure

measurements the vertical excursions of the instruments can be estimated. In this section we will consider methods for describing the motion of the mooring, its effects on the moored temperature measurements and attempts to correct the temperature for instrument depth variations.

During MODE several depth levels were instrumented for horizontal comparisons. Due to inaccurate calculation of the stretch of the dacron line used on the moorings, the mean depths of the upper instruments deviate from the design depth of a given level. The instrument level, designated as nominally 515 m in this thesis, had a design depth of 600 m. There was a 70 m depth range about 515 m between the deepest and shallowest instruments. The depths for instruments without pressure sensors were interpolated from the design depths and observed pressure depths.

Variations in the mean depth of a nominal horizontal level were not corrected for the coherence and correlation calculations where the estimates are normalized by the instrument variance. If the vertical displacement of the thermal field is small compared to the scale of the curvature of the temperature gradient, then the temperature variation is the vertical displacement times the local mean temperature gradient. When normalized by the temperature variance, the effect of the difference in the local mean temperature gradients, thus, is removed.

For the objective mapping of the temperature field, the temperature at the instrument depth z_i was corrected to the

nominal horizontal level z by integrating over the mean temperature gradient profile,

$$T(z_j) = T(z_i) + \int_{z_i}^{z_j} \left(\frac{dT}{dz} \right) dz \quad (\text{A.1.1})$$

The temperature profile is not constant with time, but varies with the vertical displacement of the isotherms. The depth correction will be in error by the difference between the instantaneous temperature gradient profile and the mean profile.

The mooring moves in response to the currents flowing past it causing depth variations in addition to the static error. The motion of an instrument on the mooring line in the presence of a temperature gradient induces a temperature fluctuation. Chhabra et al. (1975) looked in detail at the dynamic response of a single point mooring. We shall not consider the dynamic response of the mooring, but instead characterize the motion of the mooring and the magnitude of the motion induced temperature fluctuations.

The simplest mode of motion for a subsurface mooring resembles an inverted pendulum with coherent motion of all the instruments on the mooring and amplitude linearly decreasing with depth. Chhabra et al. found by tracking the buoyancy package of a subsurface mooring for six days that the mooring was always tilted and tended to swing in a horizontal plain as well as move vertically. However, with pressure sensors we can detect only vertical excursions.

Using the heavily instrumented central mooring (481) as an example, we find significant vertical coherence at the 90%

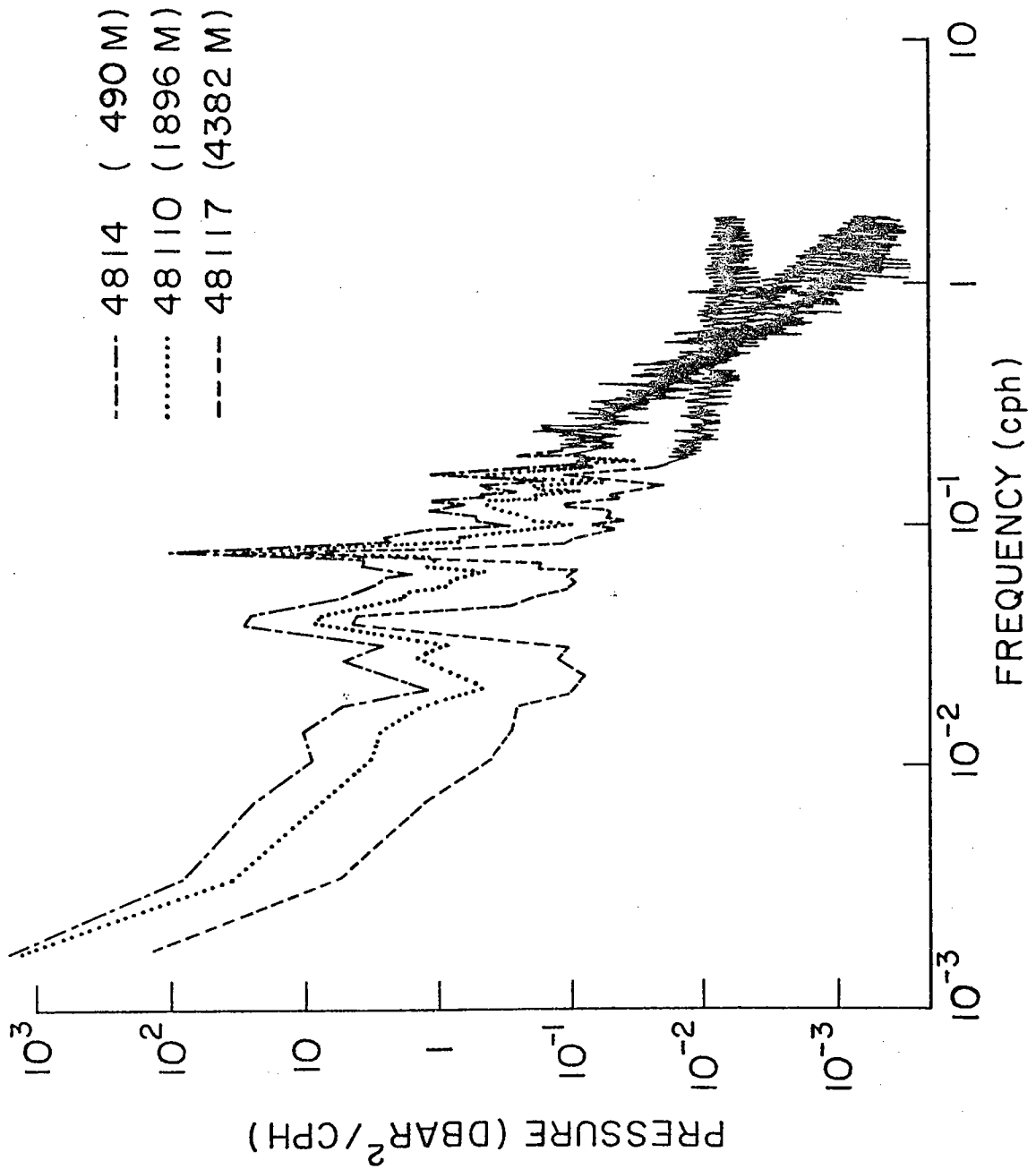


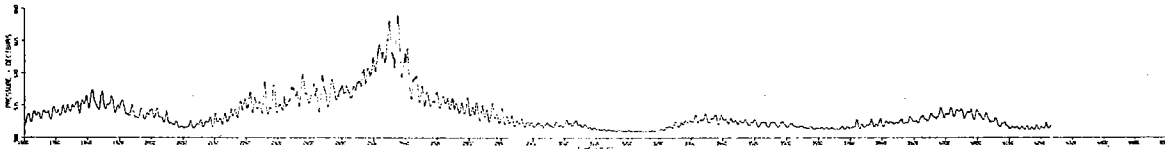
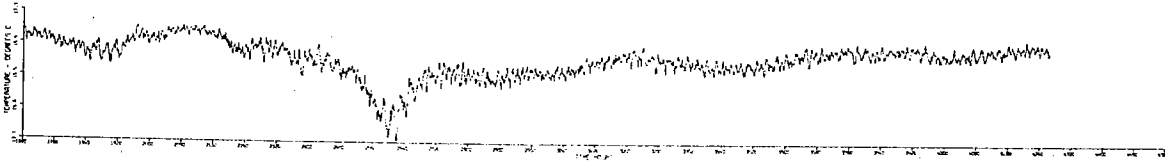
Figure A.1: Pressure spectra for three instruments on mooring 481

confidence level with nearly zero phase between all pressure sensors except the 100 m above the bottom sensor out to frequencies as high as 0.12 cph. The vertical coherence of the pressure decreases with increasing separation of the sensors. Instrument pressure spectra are dominated by the very low frequencies with strong diurnal and semidiurnal peaks. The amplitude of the instrument motion decreases with increasing depth as shown in Figure 4.1. For the deep instrument the fluctuations are below the instrument least-count noise at frequencies greater than 0.12 cph.

The observed pressure signal at an instrument is a combination of the contribution of the pressure from sea level elevation, the internal dynamic pressure fluctuations of the water motion and the motion of the instrument. In the MODE region, the surface semidiurnal tide is 33.7 cm (Hendry, 1975). For mooring 481, the pressure contribution of the surface tide is approximately half the observed tidal pressure fluctuations.

The range of instrument excursions varied considerably from a high at mooring 488 with a total excursion of 127 m and root mean square (rms) displacement of 19 m to a low at mooring 482 with a 12 m total excursion and rms displacement of 1.5 m. In general, the rms displacement increased with increasing total excursion of the instrument. The temperature and pressure plots for the nominal 500 m instruments on moorings 488 and 481 are shown in Figure A.2. The visual coherence between the temperature and pressure for mooring 488 is very high, indicating that the mooring motion has contaminated the temper-

4882



4814

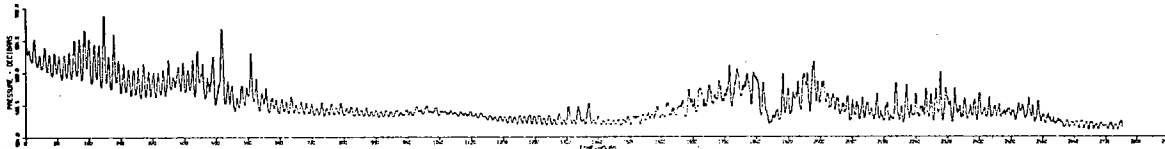
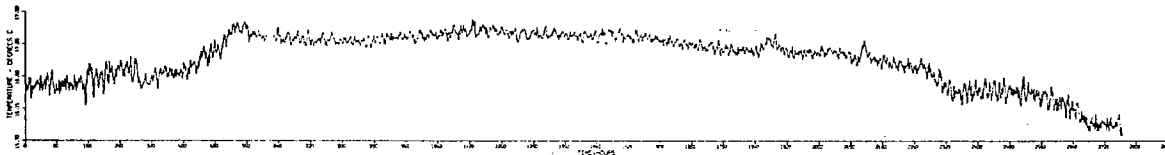


Figure A.2: Temperature and pressure records for instrument 4882 (upper plots) and 4814 (lower plots)

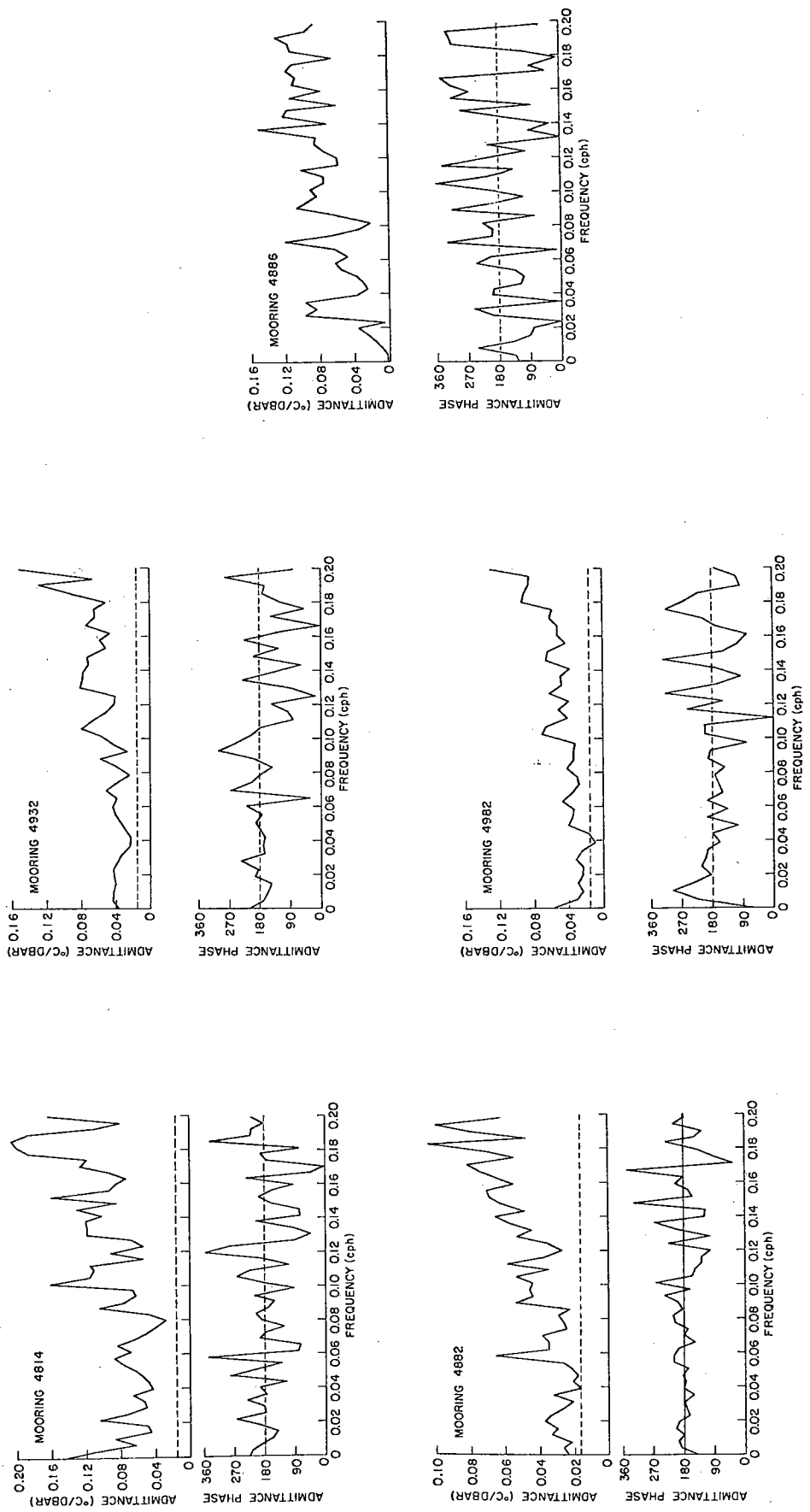


Figure A.3: Admittance amplitude and phase of the observed temperature with the instrument motion (pressure) at 4 thermocline instruments (4814, 4882, 4932, 4982) and 1 deep instrument (4886)

ature measurement. For the much quieter mooring 481, the visual coherence between temperature and pressure is low. Mooring motion does not represent a contamination problem at this mooring. To quantify the degree of motion contamination we shall calculate the admittance of the temperature and pressure for an instrument. If the temperature signal is entirely due to the motion of the instrument in a constant gradient temperature field, then the magnitude of the admittance would be equal to the temperature gradient with a phase of 180° . The admittances and phases for several instruments are shown in Figure A.3. The expected admittance for a motion induced temperature signal at 515 m is 1.5×10^{-2} °C/dbar. For instrument 4882, the admittance exceeds the pressure induced expectation by less than a factor of 2 with phase generally indistinguishable from 180° for the very low frequencies and tidal frequencies. The mooring motion has contaminated the measured temperature. In the internal gravity wave band the admittance increases with frequency. Mooring motion contamination is not as great a problem, on the average, at higher frequencies. At the relatively quiet instrument 4814, the admittance is greater than the pressure induced expectation by at least a factor of 3 except at the semidiurnal tidal frequency. Two other instruments, 4932 with a 50 m total vertical excursion and 4982 with a 30 m total vertical excursion are weakly contaminated at low frequencies. The mooring motion contamination is confined to instruments above 2000 m, since the admittance for the deeper instruments is much greater than the expected temper-

ature gradient. For example, the admittance for 4886, the 4000 m instrument with the largest vertical excursion, exceeds the pressure induced expectation by at least an order of magnitude.

The admittance estimates the average mooring motion contamination. In general, the motion induced temperature signal is greatest at very low frequencies and at tidal and inertial frequencies. However, we note in Figure A.2 that the mooring motion is not uniform. At instrument 4882, the motion is dominated by a two week burst of activity with an approximately 80 m low frequency excursion and 40 m inertial oscillations. The observed temperature during this period reflects the large instrument motion, while the visual coherence of the temperature and pressure is lower for the remainder of the record. Thus, contamination of the temperature by mooring motion is an intermittent problem.

Mooring motion can severely contaminate the moored temperature observations during times of large vertical excursions. For example, at 4882 during the 120 m excursion, the recorded temperature changed by nearly 4°C while the maximum observed variation in the temperature at 500 m from the CTD data was less than 2°C. However, during MODE, mooring motion was severe only at three moorings, 488, 493, and 498, for the main thermocline instruments and then only during a few large amplitude bursts of mooring activity.

A.2 Density and dynamic height estimation

In this thesis, we have estimated the variation of the density field from measurements of temperature only. The ocean is thermally and salt stratified. Density variations in the ocean are induced by changes in either the salinity or temperature. We only have temperature observations, but temperature and salinity are correlated in the MODE region and reasonable density estimates can be formed from the temperature and an inferred salinity.

For this appendix, we shall discuss estimation, of dynamic height, an integrated measure of the density variation, because then we may compare directly with the results of other investigators using the MODE density data. The dynamic height is the integral between two pressure surfaces of the specific volume anomaly

$$\Delta D = \int_{P_1}^{P_2} \delta \, dP \quad (\text{A.2.1})$$

where the specific volume anomaly δ is the difference between the specific volume at the in situ temperature, salinity and pressure and the specified volume at 0°C, 35% salinity and in situ pressure. Thus, there are two estimation problems for computing the dynamic height from the moored temperature alone. The mean potential temperature (Θ -S) curve for the MODE region is used to estimate the salinity from the temperature measurements to calculate the in situ specific volume. Deviations of the in situ temperature and salinity from the mean Θ -S will lead to errors in the estimated specific volume. In addition,

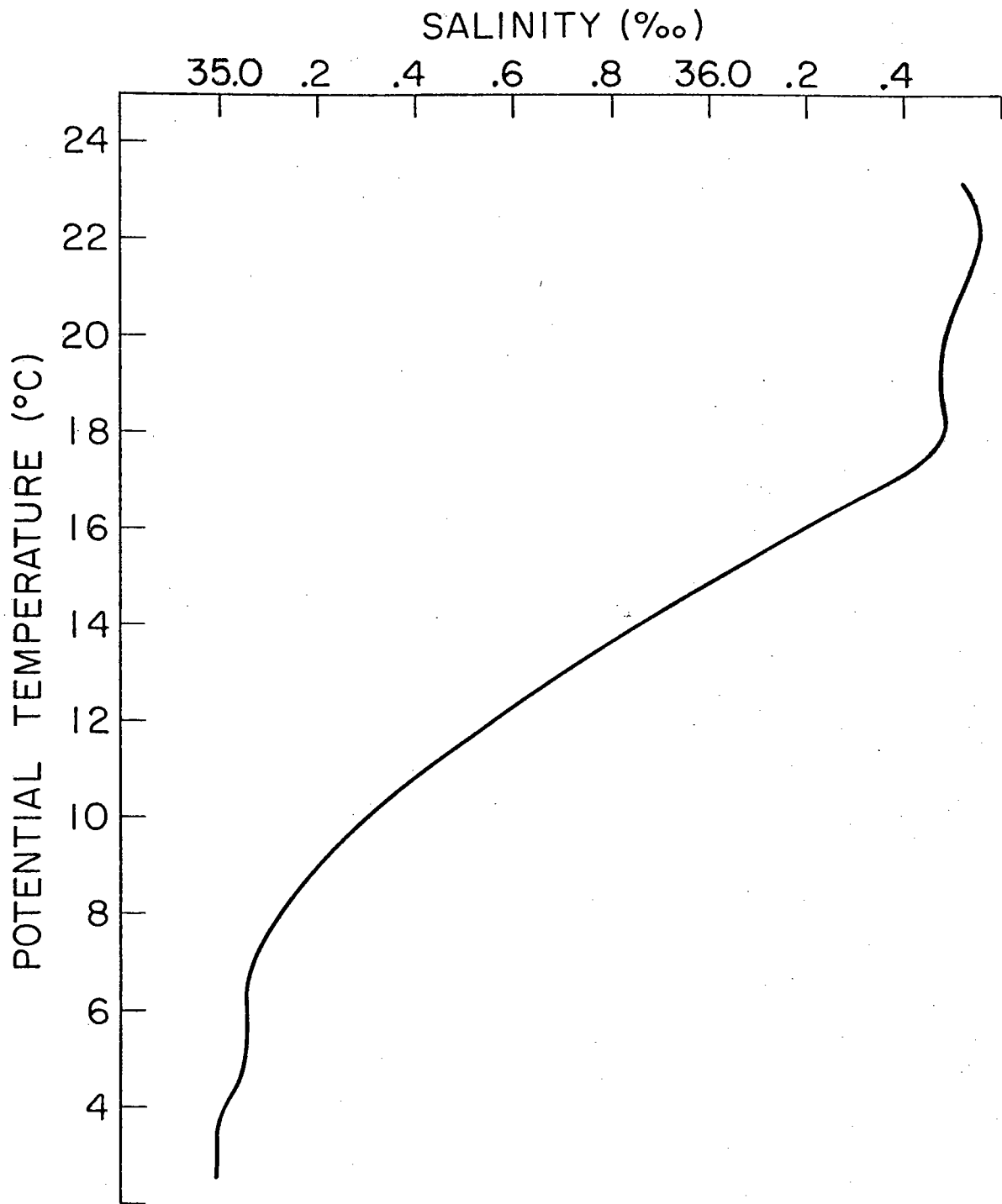


Figure A.4: Mean potential temperature-salinity (Θ -s) relation for MODE region

the integral must be estimated from a small number of measurements in a given pressure interval.

The mean Θ -S from the surface to 3000 decibars (dbars) for 141 stations taken during MODE is shown in Figure A.4 (Scarlet, private communication). The salinity fluctuations are quite large with standard deviation greater than 0.05% in the shallow water above 18°C (approximately 300 dbar surface). The shallowest instrument deployed had a mean depth of 389 m and never penetrated into the 18°C water. In the main thermocline from 17°C to 7°C (approximately 460 to 950 dbars) the standard deviation from the mean Θ -S is 0.01% which is equivalent to 0.03% error in the potential density and 0.1% error in specific volume. The salinity deviation decreases slightly at the base of the main thermocline and then increases 0.01% again in the region of Mediterranean water influence. In the deep water, the salinity deviation is 0.003%, the expected calibration error.

Thus, the expected error in the potential density due to deviations from the mean Θ -S is nearly constant and small for the main thermocline and region of Mediterranean water influence. However, since the density gradient decreases below the main thermocline, the relative error compared to the expected density fluctuation increases with depth. For a 100 m deflection of the isopycnals the error due to deviations from the Θ -S is 5% of the expected density variation at 1500 m and less than 1% at 500 m. Temperature and salinity variations in the Mediterranean water are coupled systematically and appear as lateral advection

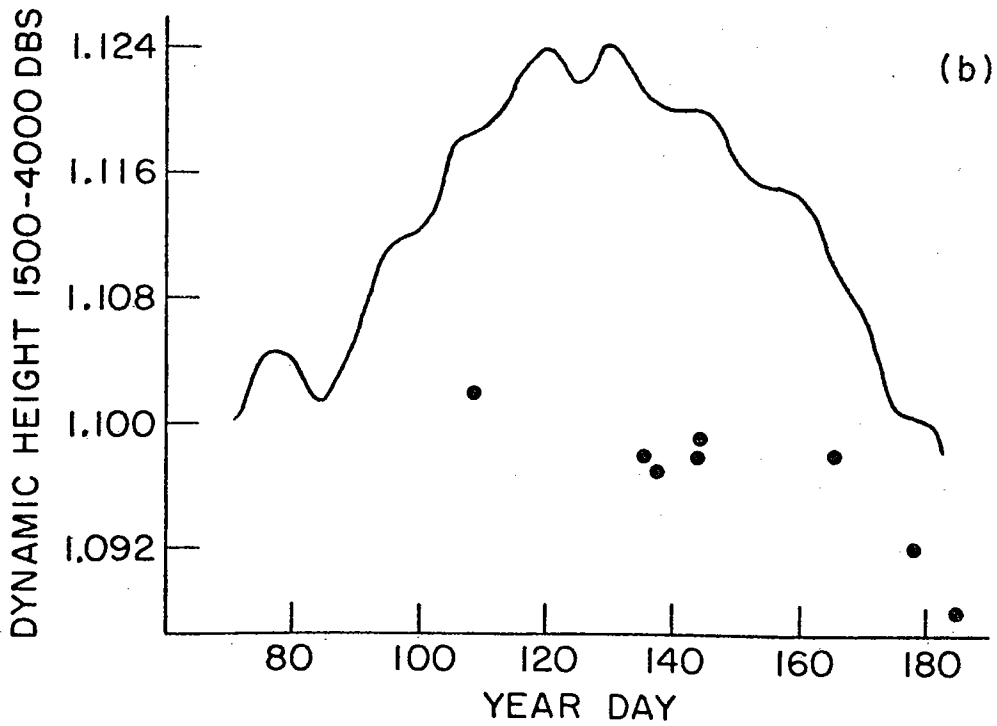
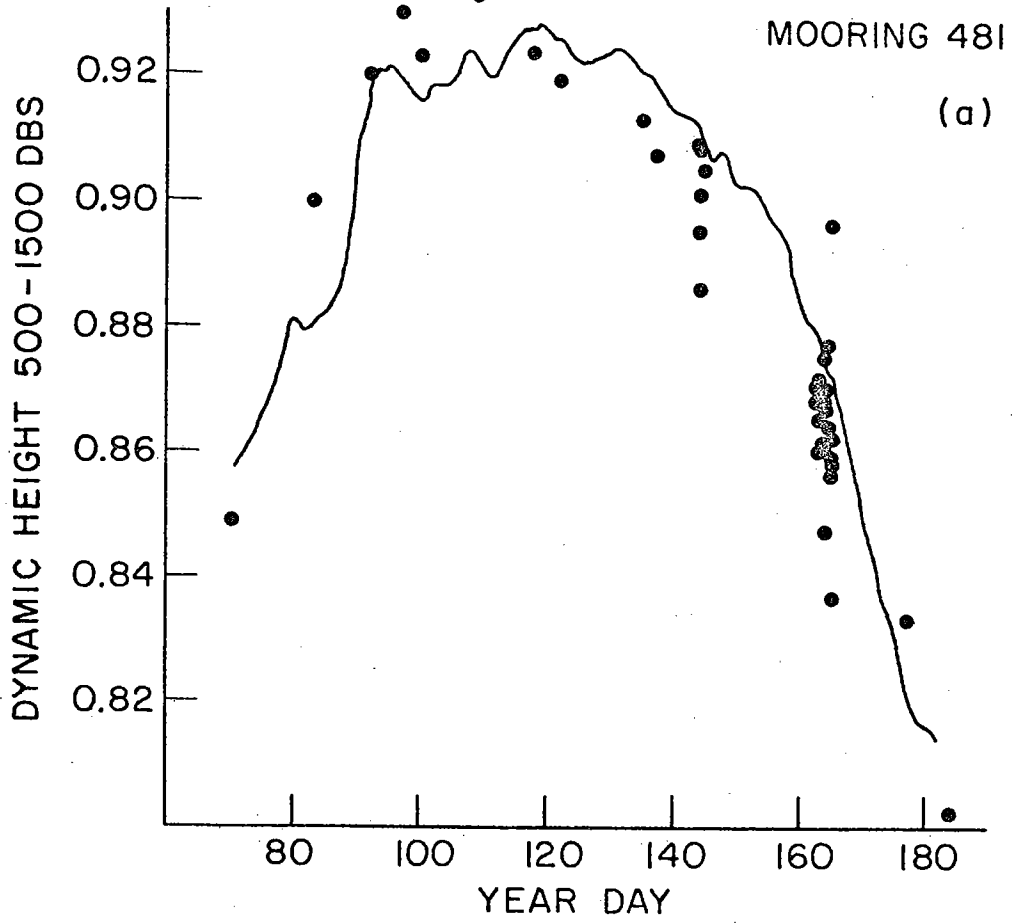


Figure A.5: Dynamic height at mooring 481 (solid line) and nearby STD stations (dots) across the thermocline (a) and across the deep water (b)

along isopycnal surfaces (Hayes, 1975). These systematic variations are the cause of the increased error in estimating density in the region of Mediterranean water influence.

Scarlet (1974a) compared the dynamic height for 28 STD stations in the MODE area calculated using the observed salinity and using the salinity from the mean θ -S curve. Between 500 and 1500 dbars, the rms difference between the two estimates is approximately 5% of the total dynamic height. Between 1500 and 3000 dbars, the difference between the two estimates increases with a tendency for the dynamic height calculated from the θ -S curve to exceed the true dynamic height. The advective intrusion of Mediterranean water in this region increases the deviation of given stations from the mean θ -S. The actual salinity of an intrusion is higher than the salinity predicted by the mean θ -S curve. Thus, the specific volume calculated using the θ -S curve is greater than the actual specific volume leading to a larger estimate of the dynamic height.

In addition the salinity estimation, the dynamic height integral, must be approximated. Assuming instruments at 500 dbar, 700 dbar, 900 dbar, and 1500 dbar, a trapezoidal integration overestimates the dynamic height by 7%. Thus, we expect the dynamic height calculated from moored temperature observations to exceed the true dynamic height.

The dynamic height calculated from the daily averaged temperature for mooring 481 is shown in Figure A.5. For instruments without pressure measurements, the pressures for nearby instruments were linearly interpolated. The calculated

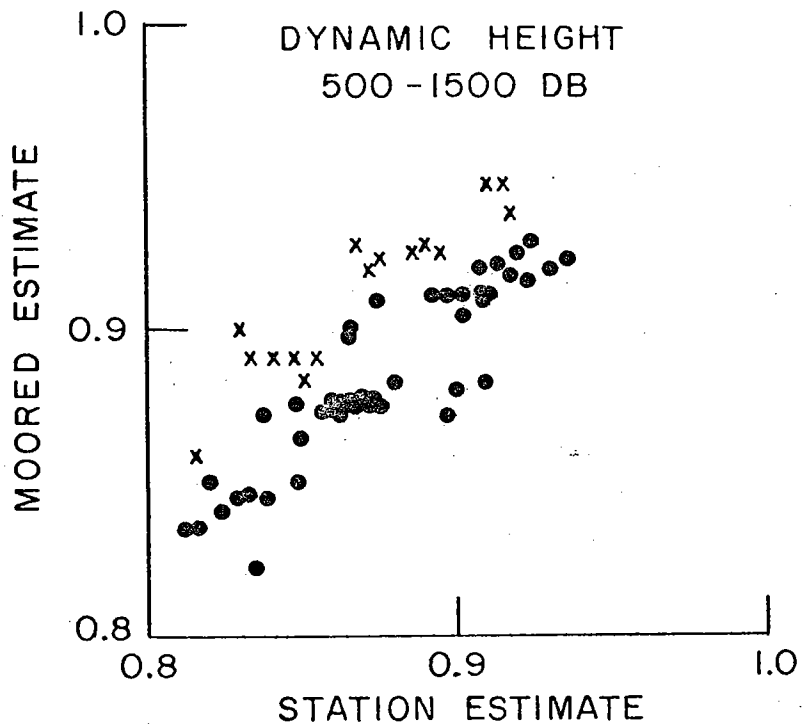


Figure A.6: Dynamic height across the thermocline estimated from moored temperature and nearby STD stations

dynamic heights were interpolated to the 500 dbar and 1500 dbar surfaces. The dynamic heights from moored temperatures are compared with the dynamic heights calculated from STD stations within 15 km of the mooring. The rms difference between the dynamic height estimates is 2% of the total dynamic height. Near the central mooring, 481, between days 163 and 165, the station dynamic heights vary by 0.059 dynamic meters, almost half the total variation near this station in 114 days.

In Figure A.6 the dynamic height calculated from the moored temperatures and the station dynamic heights for all the MODE-I moorings are compared. A linear regression of the two estimates has slope 0.83 with intercept 0.13 and the dynamic height estimates have a correlation 0.8. The slope of the regression line is not significantly different from zero at 95% confidence. The rms deviation of the two estimates is 0.04 dynamic meters.

In this appendix we have shown that the density can be estimated from the moored temperature using the mean θ - S curve of the MODE region with an error of approximately 5%, which is acceptable for the purposes of this thesis. Thus, moored temperature observations are sufficiently representative of the dynamics of the mesoscale flow.

Appendix B Maximum Entropy Spectral Estimation

In Chapter III, we introduced the maximum entropy spectral estimator as an alternate way of computing the velocity and temperature spectra. At the expense of some difficulty in interpreting the estimated amplitudes, the maximum entropy spectrum is data adaptive with increased sensitivity and resolution of periodic signals over the conventional spectrum. In this appendix, we shall show briefly how the maximum entropy spectral estimate is derived for a random process, following the work of Lacoss (1971) and Smylie, et al. (1973).

A spectrum characterizes a random process and allows the prediction of a time series of the process. The conventional spectrum is the Fourier transform of the autocorrelation

$$S(\omega) = \Delta t \sum_{k=-\infty}^{\infty} \phi(k) e^{-2\pi i \omega k \Delta t} \quad (\text{B.1})$$

and represents a periodic continuation of previous information from a sample time series. However, there are other ways to characterize a random process. For example, suppose the unknown autocorrelations are predicted from the sample autocorrelations in a manner such that no entropy or information is added. From information theory, the entropy of a N dimensional random variable $\underline{z} = (z_0, z_1, \dots, z_N)$ (an idealization of the time series z_i) with a continuum of allowed values is

$$H = - \int f(\underline{z}) \ln F(\underline{z}) d\underline{z} - (2N+2) \ln a \quad (\text{B.2})$$

where $f(\underline{z})$ is the joint probability distribution, $d\underline{V}$ is a volume element of the sample space and a is a constant with dimension of the sample space. The entropy density is related to the spectrum of the process by

$$h = \frac{1}{2} \ln \Delta t + \frac{\Delta t}{2} \int_{-\frac{1}{2\Delta t}}^{\frac{1}{2\Delta t}} \ln [S(\omega)] d\omega \quad (\text{B.3})$$

Now, making the entropy density stationary with respect to the unknown autocorrelations $\phi(k)$, $|k| > N+1$, the resultant spectrum is

$$S(\omega) = \frac{\Delta t P_{N+1}}{\left| 1 + \sum_{j=1}^{N-1} \gamma_j e^{-2\pi i \omega j \Delta t} \right|^2} \quad (\text{B.4})$$

where the prediction-error filter coefficients γ_j are given by

$$R \Gamma = P \quad (\text{B.5})$$

where R is the autocorrelation matrix with elements $\phi(k)$, Γ is the column matrix $(1, \gamma_1, \dots, \gamma_{N-1})$ and P is the column matrix $(p_{N+1}, 0, \dots, 0)$. An advantage of the maximum entropy spectrum is its sensitivity to peaks in the true spectrum and its enhanced resolution over conventional estimates. Lacoss (1971) compared the resolution of the maximum entropy and conventional spectral estimates and we refer the reader to that paper for further discussion.

Appendix C Site Mooring Data Summary

Two long duration site moorings were maintained as part of MODE. The site mooring locations are designated MODE Center (mooring 1 during MODE-I) at 28° N, $69^{\circ}40'$ W over the smooth topography of the Hatteras Abyssal Plain and MODE East (mooring 8 during MODE-I) at $28^{\circ}10'$ N, $68^{\circ}40'$ W over the rough topography of the abyssal hills. To avoid problems with disparate energy levels from surface and subsurface moorings only data from subsurface moorings are considered (thus excluding MODE-0). On each site mooring the primary levels of instrumentation are nominally 500 m, 1500 m and 4000 m. Gaps occur in the data records due to instrument failure and availability. The number of data days of temperature and velocity at each site mooring is listed in Table C.1, while the actual records used are given in Table C.2. At MODE Center, nearly two years of velocity and temperature data are available, while at MODE East there is generally less than one year of data. The daily averaged temperature data at the site moorings are shown in Figure I.2.

Mooring	Velocity			Temperature		
	Nominal Depth Level			Nominal Depth Level		
	500 m	1500 m	4000 m	500 m	1500 m	4000 m
1	666	731	660	603	416	600
8	224	480	590	325	103	325

Table C.1: Data days of low frequency velocity and temperature data from MODE Center at 28° N, 69°40' W and at MODE East at 28°10' N, 69°40' W

Instrument Designation	Depth (meters)	Start Date	Stop Date	Data Days	
				Velocity	Temperature
4742	583	XI-6-72	III-8-73	123	None
4813	489	III-12	VI-27	11	112
5031	494	VI-29	XII-11	166	None
5222	581	XII-16	IV-18-74	None	125
5381	472	IV-20	VII-25	97	97
5382	574	IV-21	VII-25	None	96
5421	495	VII-29	IV-23-75	269	269
				<u>665</u>	
4743	1595	XI-6-72	III-8-73	123	None
4819	1392	III-13	VII-2	25	112
5032	1501	VI-30	XII-8	162	None
5225	1497	XII-16	IV-11-74	117	None
5385	1468	IV-20	VII-25	97	97
5424	1499	VII-29	II-21-75	207	207
4744	4105	XI-6-72	III-8-73	123	None
48115	3968	III-13	VII-2	112	112
5229	3998	XII-16	IV-9-74	115	None
52211	4404	XII-16	IV-18-74	None	124
5389	3973	IV-20	VII-27	97	None
53810	3976	IV-21	VII-27	None	96
53811	4380	IV-21	VII-27	None	96
5427	3985	VII-29	II-27-75	213	None
5428	3987	VII-30	IV-23-75	None	268

Table C.2a: Data records at MODE Center

Instrument Designation	Depth (meters)	Start Date	Stop Date	Data Days	
				Velocity	Temperature
4732	370	XI-1-72	XII-15-72	45	None
4821	406	III-14-73	VI-24	0	103
5211	508	XII-15	IV-10-74	117	None
5212	592	XII-15	IV-17-74	None	125
5401	509	V-27	VII-27	62	None
5402	626	IV-22	VII-27	None	97
4724	1385	XI-1-72	III-9-73	129	None
4825	1411	III-14	VI-23	5	103
5022	1524	VI-29	XII-6	161	None
5215	1506	XII-15	IV-10-74	117	None
5405	1511	IV-22	VI-28	68	None
4735	3900	XI-1-72	III-9-73	129	None
4827	3957	III-14	VI-24	80	103
5023	4015	VI-28	XII-11	167	None
5219	3996	XII-15	IV-10-74	117	None
52110	3998	XII-15	IV-17-74	None	125
52111	4404	XII-15	IV-17-74	None	125
5409	4008	IV-22	VII-27	97	None
54010	4024	IV-22	VII-27	None	97
54011	4419	IV-22	VII-27	None	97

Table C.2b: Data records at MODE East

BIBLIOGRAPHY

- Amos, D. E., and L. H. Koopmans (1963) Tables of the Distribution of the Coefficient of Coherence for Stationary Bivariate Gaussian Processes, Sandia Corporation SCR-483, 328 pp
- Armi, L., and R. C. Millard, Jr. (1976) The bottom boundary layer of the deep ocean, J. Phys. Ocean., in press
- Berstein, R. L., and W. B. White (1974) Time and length scales of baroclinic eddies in the central North Pacific Ocean, J. Phys. Ocean., 4, 613-624
- Bretherton, F., R. Davis, and C. Fandry (1976) A technique for objective analysis and design of oceanographic experiments, Deep-Sea Res., in press
- Bretherton, F., and D. Haidvogel (1976) Two dimensional turbulence above topography, submitted to J. Fluid Mech.
- Bryan, K. (1974) Can baroclinically unstable eddies be detected by hydrographic stations, MODE Hot Line News, 56, unpublished document, Woods Hole Oceanographic Institution
- Bryden, H. L. (1975) Momentum, Mass, Heat and Vorticity Balances from Oceanic Measurements of Current and Temperature, Ph.D. thesis, Massachusetts Institute of Technology/Woods Hole Oceanographic Institution
- Busch, N. E., and E. L. Petersen (1971) Analysis of non-stationary ensembles in Statistical Methods and Instrumentations in Geophysics, A. S. Kjeles, ed., Proceedings of the NATO Advanced Study Institute in Norway, April, 1971, Teknologisk Forlag, Oslo
- Capon, J. (1969) High-resolution frequency-wavenumber spectrum analysis, Proc. IEEE, 57, 1408-1418
- Capon, J., and N. R. Goodman (1970) Probability distributions for estimators of the frequency wavenumber spectrum, Proc. IEEE, 58, 1785-1786
- Charney, J. G. (1955) The Gulf Stream as an inertial boundary layer, Proc. Nat. Acad. Sci., 41, 731-740
- Charney, J. G. (1971) Geostrophic turbulence, J. Atmos. Sci., 28, 1087-1095

- Chhabra, N. K., J. M. Dahlen, and M. R. Froidevaux (1974) Mooring Dynamics Experiment: Determination of a Verified Dynamic Model of the WHOI Intermediate Mooring, C. S. Draper Laboratory, Inc., R-823
- Cole, J. D. (1968) Perturbation Methods in Applied Mathematics, Blaisdell Publishing Company, Waltham, Mass., 260 pp
- Crease, J. (1962) Velocity measurements in the deep water of the western North Atlantic, J. Geophys. Res., 67, 3173-3176
- Davis, R. (1975) Statistical methods in Dynamics and the Analysis of MODE-I: Report of the MODE-I Dynamics Group, unpublished document, Massachusetts Institute of Technology
- Eckart, C. (1960) Hydrodynamics of Oceans and Atmospheres, Pergamon Press, Oxford, 290 pp
- Freeland, H. J., and W. J. Gould (1976) Objective analysis of meso-scale ocean circulation features, Deep-Sea Res., in press
- Freeland, H. J., P. B. Rhines, and T. Rossby (1975) Statistical observations of the trajectories of neutrally buoyant floats in the North Atlantic, J. Mar. Res., 33, 383-404
- Gandin, L. S. (1965) Objective Analysis of Meteorological Fields, Israel Program for Scientific Translations, Jerusalem, 242 pp
- Gill, A. E. (1974a) Mid-ocean eddies in ocean weather ship records, MODE Hot Line News, 49, unpublished document, Woods Hole Oceanographic Institution
- (1974b) The stability of planetary waves on an infinite beta plane, Geophysic. Fluid Dyn., 6, 29-47
- Gill, A. E., J. S. A. Grean, and A. J. Simmons (1974) Energy partition in the large-scale ocean circulation and the production of mid-ocean eddies, Deep-Sea Res., 21, 499-528
- Gould, W. J., W. J. Schmitz, Jr. and C. Wunsch (1974) Preliminary field results for a Mid-Ocean Dynamics Experiment (MODE-0), Deep-Sea Res., 21, 911-931

- Haidvogel, D. B. (1976) The Sensitivity and Predicatability of Mesoscale Eddies in an Idealized Model Ocean, Ph. D. thesis, Massachusetts Institute of Technology/ Woods Hole Oceanographic Institution
- Hall, R. E. (1974) Diffraction of Rossby waves by a wedge-shaped lateral boundary in Summer Study Program in Geophysical Fluid Dynamics: Fellowship Lectures, Woods Hole Oceanographic Institution, TR 74-63
- (1976) Scattering of Rossby Waves by Topography in a Stratified Ocean, Ph.D. thesis, University of California, San Diego
- Hayes, S. P. (1975) The temperature and salinity fine structure of the Mediterranean Water in the Western North Atlantic, Deep-Sea Res., 22, 1-11
- Hendry, R. M. (1975) The Generation, Energetics and Propagation of Internal Tides in the Western North Atlantic Ocean, Ph.D. thesis, Massachusetts Institute of Technology/Woods Hole Oceanographic Institution
- Hogg, N. G. (1976) On spatially growing baroclinic waves in the ocean, J. Fluid Mech., in press
- Holland, W. R., and L. B. Lin (1975) On the generation of mesoscale eddies and their contribution to the oceanic general circulation I. A preliminary numerical experiment, J. Phys. Ocean., 5, 642-657
- Hollister, C. D., and B. C. Heezen (1972) Geological effects of ocean bottom currents: western North Atlantic in Studies in Physical Oceanography, A. L. Gordon, ed., Gordon and Breach
- Isaacson, E., and H. B. Keller (1966) Analysis of Numerical Methods, John Wiley and Sons, Inc., New York, 541 pp
- Jenkins, G. M., and D. G. Watts (1968) Spectral Analysis and its Applications, Holden-Day, San Francisco, 525 pp
- Kendall, M., and A. Stuart (1976) The Advanced Theory of Statistics, vol. 3, Griffen and Co., Ltd. London, 585 pp
- Kenyon, K. (1964) Nonlinear energy transfer in a Rossby wave spectrum in Summer Study Program in Geophysical Fluid Dynamics: Student Lectures, Woods Hole Oceanographic Institution

- Killworth, P. D., and D. Anderson (1975a) Meaningless modes?, MODE Hot Line News, 72, unpublished document, Woods Hole Oceanographic Institution
- (1975b) Some thoughts on eddy generation, MODE Hot Line News, 73, unpublished document, Woods Hole Oceanographic Institution
- (1975c) Horizontal and vertical fitting of MODE-type data, MODE Hot Line News, 78, unpublished document, Woods Hole Oceanographic Institution
- Kim, K. (1975) Instability and Energetics in a Baroclinic Ocean, Ph.D. thesis, Massachusetts Institute of Technology/Woods Hole Oceanographic Institution
- Kosambi, D. D. (1943) Statistics in function space, J. Indian Math. Soc., 7, 76-88
- Koshlyakov, M. N., and Y. M. Grachev (1973) Mesoscale currents at a hydrophysical polygon in the tropical Atlantic, Deep-Sea Res., 20, 507-526
- Kundu, P. J., and J. S. Allen (1976) Some three-dimensional characteristics of low frequency current fluctuations near the Oregon coast, J. Phys. Ocean., 6, 181-199
- Lacoss, R. T. (1971) Data adaptive spectral analysis methods, Geophysics, 36, 601-675
- Longuet-Higgins, M. S. (1965) Planetary waves on a rotating sphere II, Proc. Roy. Soc. Lond. A, 289, 40-54
- (1969) On the transport of mass by time-varying ocean currents, Deep-Sea Res., 16, 431-447
- Longuet-Higgins, M. S., and A. E. Gill (1967) Resonant interactions between planetary waves, Proc. Roy. Soc. Lond. A, 299, 120-140
- Lorenz, E. N. (1969) The nature of the global circulation of the atmosphere: a present view, in The Global Circulation of the Atmosphere. G. A. Corby, ed., Royal Meteorological Society, London
- Massey, F. J. (1951) The Kolmogorov-Smirnov test for goodness of fit, J. Amer. Stat. Assoc., 46, 68-75
- McWilliams, J. C. (1974) MODE mean currents and eddy surface intensification, MODE Hot Line News, 57, unpublished document, Woods Hole Oceanographic Institution

- McWilliams, J. G., and G. Flierl (1976) Optimal, quasigeostrophic wave analyses of MODE array data, Deep-Sea Res., 23, 285-300
- McWilliams, J. C., and A. R. Robinson (1974) A wave analysis of the Polygon array in the tropical Atlantic, Deep-Sea Res., 21, 359-368
- Millard, R. C., Jr., and H. Bryden (1973) Spatially averaged MODE-I CTD stations, MODE Hot Line News, 43, unpublished document, Woods Hole Oceanographic Institution
- Miller, L. H. (1951) Table of percentage points of Kolmogorov statistics, J. Amer. Math. Assoc., 51, 111-121
- Monin, A. S., and A. M. Yaglom (1975) Statistical Fluid Mechanics: Mechanics of Turbulence, vol. 2, M.I.T. Press (English translation), Cambridge, Mass., 874 pp
- Neville, E. H. (1944) Jacobian Elliptic Functions, Oxford University Press, London
- Obukhov, A. M. (1960) The statistically orthogonal expansion of empirical functions, Izv. Geophys., 432-439
- Orlanski, I., and C. Cox (1973) Baroclinic instability in ocean currents, Geophys. Fluid Dyn., 4, 297-332
- Owens, W. B. (1975) A Numerical Study of Mid-Ocean Mesoscale Eddies, Ph.D. thesis, Johns Hopkins University and National Center for Atmospheric Research
- Pedlosky, J. (1971) Geophysical Fluid Dynamics in Mathematical Problems in the Geophysical Sciences 1. Geophysical Fluid Dynamics, Lectures in Applied Mathematics, vol. 13, W. H. Reid, ed., American Mathematical Society, Providence, 1-60
- Phillips, N. (1966) Large-scale eddy motion in the western North Atlantic, J. Geophys. Res., 71, 3883-3891
- Pochapsky, T. E. (1976) Vertical structure of currents and temperature in the western Sargasso Sea, J. Phys. Ocean., 6, 45-56
- Rhines, P. B. (1971) A comment on the Aries observations, Phil. Trans. Roy. Soc. Lond. A, 270, 461-463
- (1975) Waves and turbulence on a beta plane, J. Fluid Mech., 69, 417-433

- Rhines, P. B. (1976) The dynamics of unsteady currents to appear in The Sea, vol. 6, J. J. O'Brien, ed., John Wiley and Sons, Inc., New York
- Rhines, P. B., and F. Bretherton (1973) Topographic Rossby waves in a rough-bottomed ocean, J. Fluid Mech., 61, 583-607
- Richman, J. G., and R. C. Millard, Jr. (1976) Observations and thoughts on the homogeneous bottom layer in the Western North Atlantic, manuscript in preparation
- Robinson, A. R., and J. C. McWilliams (1974) The baroclinic instability of the open ocean, J. Phys. Ocean., 4, 281-294
- Sanford, T. B. (1975) Observations of the vertical structure of internal waves, J. Geophys. Res., 80, 3861-3871
- Scarlet, R. (1974a) Densities without salinities, MODE Hot Line News, 57, unpublished document, Woods Hole Oceanographic Institution
- (1974b) Correlation functions from MODE-I density data, MODE Hot Line News, 60, unpublished document, Woods Hole Oceanographic Institution
- Scarlet, R., A. Leetma, W. Sturges, and J. Crease (1976) The MODE-I density profile experiment: Part I: Map of the mid-ocean eddy field, unpublished manuscript
- Schmitz, W. J. Jr. (1974) Observations of low frequency current fluctuations on the Continental Slope and Rise near Site D, J. Mar. Res., 32, 233-251
- (1976) On the deep general circulation in the western North Atlantic, submitted to J. Mar. Res.
- Schmitz, W. J. Jr., J. R. Luyten, and W. Sturges (1976) On the spatial variation of the properties of low frequency fluctuations in the deep western North Atlantic, unpublished manuscript
- Smylie, D. E., G. K. C. Clarke, and T. J. Ulrych (1973) Analysis of irregularities in the earth's rotation, Methods in Computational Physics, 13, 391-430
- Stommel, H. M. (1948) The westward intensification of wind-driven ocean currents, Trans. Amer. Geophys. Union, 29, 202-206

- Sverdrup, H. U. (1947) Wind-driven currents in a baroclinic ocean, with application to the equatorial currents of the Eastern Pacific, Proc. Nat. Acad. Sci., 33, 318-326
- Swallow, J. C. (1971) The Aries current measurements in the western North Atlantic, Phil. Trans. Roy. Soc. A, 270, 451-460
- Taylor, G. I. (1921) Diffusion by continuous movements, Proc. Lon. Math Soc., 20, 196-212
- Veronis, G., and H. Stommel (1956) The action of variable wind stresses on a stratified ocean, J. Mar. Res., 15, 43-75
- Vonder Haar, T. H., and A. H. Oort (1973) New estimate of annual poleward energy transport by northern hemisphere oceans, J. Phys. Ocean., 2, 169-172
- Wunsch, C. (1972) The spectrum from two years to two minutes of temperature fluctuations in the main thermocline at Bermuda, Deep-Sea Res., 19, 577-593
- Wunsch, C., and J. Dahlen (1974) A moored temperature and pressure recorder, Deep-Sea Res., 21, 145-154
- Wunsch, C., and R. Hendry (1972) Array measurements of the bottom boundary layer and the internal wave field on the continental slope, Geophys. Fluid Dyn., 4, 101-145

BIOGRAPHICAL NOTE

The author was born on June 29, 1949, in Washington, D. C. He received a Bachelor of Science degree from Harvey Mudd College with distinction and honors in physics in 1971. He has pursued his graduate studies in the Massachusetts Institute of Technology/Woods Hole Oceanographic Institution Joint Program in Oceanography with support from a NSF Graduate Fellowship and a Fannie and John Hertz Foundation Fellowship